

“Mobile NMR for rock porosity and permeability”

Von der Fakultät für Georessourcen und Materialtechnik
der Rheinisch-Westfälischen Technischen Hochschule Aachen

zur Erlangung des akademischen Grades eines

Doktors der Naturwissenschaften

genehmigte Dissertation

vorgelegt von **Diplom-Geologin**

Juliane Arnold

aus Düsseldorf

Berichter: Univ.-Prof. Dr. Christoph Clauser
Univ.-Prof. Dr. Dr. Bernhard Blümich

Tag der mündlichen Prüfung: 20. August 2007

Diese Dissertation ist auf den Internetseiten der Hochschulbibliothek online
verfügbar

Zusammenfassung

Als nicht-invasives Verfahren bietet die kernmagnetische Resonanz (engl. Nuclear magnetic resonance, NMR) unter anderem die Möglichkeit Gesteinsformationen hinsichtlich ihrer hydraulischen Fließeigenschaften zu charakterisieren. Im Rahmen dieser Arbeit wurden drei verschiedene mobile NMR-Geräte angewendet, um die Porosität und Permeabilität an ausgewählten Bohrkernen mit Durchmessern bis zu 60 mm zu bestimmen. Neben der Anwendung im Labor, eignen sich die handlichen Sensoren auch für den Einsatz an Bohrplattformen und auf Forschungsschiffen. Dies hat zum Vorteil, dass das frisch gewonnene Kernmaterial im noch bergfeuchten Zustand untersucht werden kann.

Bei den mobilen NMR Geräten handelt es sich um experimentelle Prototypen, die sich in der Stärke und Homogenität ihres jeweiligen statischen Magnetfeldes unterscheiden. Während die unilaterale NMR-MOUSE[®] ein inhomogenes Magnetfeld in der Probe erzeugt, umschließen die beiden Halbach Kern-Scanner die Bohrkern in einem zylindrischen Volumen, woraus ein annähernd homogenes Magnetfeld in der Probe resultiert. Während mit allen drei Sensoren eindimensionale (1D) Messungen der Relaxationszeit durchgeführt werden können, eignet sich der modifizierte Halbach Kern-Scanner auch für die simultane zweidimensionale (2D) Messung von Relaxationszeiten an Kernstücken mit Durchmessern bis zu 20 mm.

1D transversale Relaxationszeiten wurden an ganzen und halbierten zylindrischen Kernen verschiedener Gesteintypen, wie Kalkstein, Sandstein, Basalt, Peridotit, Tonschiefer und an unverfestigten tonreichen Sedimenten gemessen. Das Probenmaterial unterschied sich in Porosität, Porenradienverteilung und magnetischer Suszeptibilität. Porositäten, welche anhand der NMR Signalamplitude bestimmt wurden, stimmen gut mit unabhängig gemessenen Porositätswerten überein. Weiterhin können die Messungen der transversalen Relaxationszeiten im homogenen Magnetfeld der beiden Halbach Kern-Scanner zur Vorhersage der Permeabilität genutzt werden. Bei hochporösen Sandstein- und Kalkstein-Proben eignet sich zur Berechnung der Permeabilität ein Standardverfahren für Bohrlochdaten, welches in der Ölindustrie gebräuchlich ist. Für Proben mit geringer Porosität und kleinen Porenradien, die interne Magnetfeldgradienten verursachen, ergeben sich jedoch große Abweichungen zu unabhängig bestimmten Permeabilitäten. Mittels einer neuen Modelltheorie wurde die Abhängigkeit der Oberflächenrelaxivität ρ_2 vom Porenradius beschrieben und sowohl eine analytische als auch eine empirische Formel entwickelt, die auf

niedrigporöse Gesteine der Bohrung Allermöhe angewendet wurden. Verknüpft mit der Kozeny-Carman Gleichung ließen sich unter Berücksichtigung korrigierter Werte von ρ_2 und mit dem logarithmischen Mittel aus den T_2 Verteilungskurven genaue Permeabilitäten bestimmen.

Abstract

Three different mobile Nuclear Magnetic Resonance (NMR) core-scanners were used to measure porosity and permeability of water-saturated drill cores and core plugs in a non-destructive way. In addition to their use in the laboratory, the small and light-weight devices are conveniently shipped, e.g. to drilling platforms. They allow rapid wellsite analysis of large-size cores in a fresh state without prior preparation.

The sensors are experimental prototypes and differ in their magnetic field strength and homogeneity. The magnetic field of the NMR-MOUSE[®] is applied to the sample from one side and is inhomogeneous within the object. The two Halbach core-scanners enclose the samples in a large cylindrical volume with a nearly homogeneous magnetic field. Besides one-dimensional (1D) relaxation measurements which can be performed with all sensors, the second version of the Halbach core-scanner is also suitable for two-dimensional (2D) relaxation measurements on core plugs.

1D transverse relaxation measurements were made on fully cylindrical and split, semi-cylindrical cores of limestone, sandstone, basalt, peridotite, shale and unconsolidated clay-rich sediments with varying values of porosity, pore size and magnetic susceptibility. Porosity calculated from amplitudes of transverse relaxation measurements with all instruments agrees well with porosity determined by independent methods. Transverse relaxation measurements within the homogeneous magnetic field of the Halbach core-scanners can be used for permeability prediction. In the case of sandstone and limestone samples with high porosity, a standard calculation scheme from NMR logging in the oil industry yields good results. However, standard methods cannot be applied for an accurate permeability prediction for samples with low porosity and small pore sizes associated with high internal magnetic field gradients. Therefore, a new model theory was developed, which describes the pore radius dependence of the surface relaxivity ρ_2 as both an analytical and a more practicable empirical equation. Regarding corrected ρ_2 values, permeability can be predicted accurately from the logarithmic mean of the T_2 distribution from the physically based Kozeny-Carman equation.

Contents

1	Introduction	1
1.1	NMR in formation evaluation	1
1.2	Objectives of this thesis.....	3
1.3	Content of this thesis	5
2	Fundamentals of NMR petrophysics	6
2.1	Polarization.....	6
2.2	Pulse tipping and free induction decay.....	7
2.3	Relaxation mechanisms in porous media	9
2.4	T_2 measurements.....	11
2.5	T_1 measurements.....	13
2.6	2D T_1 - T_2 correlation measurements.....	14
3	Mobile NMR instrumentation	17
3.1	NMR-MOUSE [®]	17
3.2	Halbach core-scanner	18
3.3	Improved Halbach core-scanner.....	20
4	Samples and experimental procedures	22
4.1	Sample selection.....	22
4.2	Experimental procedures.....	27
5	Calibration to porosity	30
5.1	NMR signal processing for porosity.....	31
5.2	Porosity measurements.....	32
5.2	Appraisal of the results.....	36
6	Estimation of pore size distributions and permeability	38
6.1	Influence of external magnetic field gradients	39
6.2	Limits due to magnetic susceptibility.....	41
6.3	Standard NMR models for permeability prediction	42
6.4	General permeability relationships.....	46
6.5	Mercury injection curves.....	52
6.6	Surface relaxation and ‘internal field gradient relaxation’	55
6.7	2D T_1 - T_2 correlation experiments.....	57

6.8 Permeability from 1D T_2 relaxation	65
6.9 Appraisal of the results	69
7 Conclusion & Outlook.....	71
References.....	74
Appendix.....	80

1 Introduction

Since its discovery in 1945, nuclear magnetic resonance (NMR) has become a valuable tool in physics, chemistry, biology and medicine. The unique feature of NMR is the non-destructive approach. NMR is routinely applied in analytical chemistry for elucidation of chemical structures by NMR spectroscopy and in medicine for tomographic diagnostics by magnetic resonance imaging (Blümich, 2000). In geophysics the NMR technique is well known for well logging and laboratory applications. Moreover, the surface NMR (SNMR) method is a fairly new technique for groundwater exploration and aquifer characterization (Müller and Yaramanci, 2005; Yaramanci, 2000). The usefulness of NMR is based on its direct sensitivity to water. Hydrogen nuclei in fluids of porous rocks are excited with radio frequency (rf) pulses. Hydrogen nuclei have a magnetic moment and behave like small bar magnets. When subjected to a magnetic field, such nuclei tend to align their magnetic moments parallel to the field, producing a net nuclear magnetization. In the NMR method the angle of the magnetization with respect to the magnetic field is changed by a rf pulse. Once the pulse has faded it regains its original orientation by relaxation. In a saturated porous medium this relaxation time depends not only on the fluid but also on the medium and the interaction between the medium and the magnetic moments. Thus, the study of relaxation time can provide information on structural parameters as porosity, pore size distribution or permeability of porous media.

1.1 NMR in formation evaluation

Mobile NMR has its origin in inside-out NMR, where NMR spectrometers are lowered into boreholes for analysis of fluids in the surrounding rock (Blümich et al., 1998; Hürlimann and Griffin, 2000). NMR well-logging devices are unilateral NMR sensors (Matzkanin, 1989). The term *unilateral* refers to the fact that the study object is not inserted into the magnet for measurement (the common case in NMR) but applied to the NMR sensor from one side. Suitable dimensioning of magnet and coils ensures that the polarizing magnetic field B_0 and the rf magnetic field B_1 are only moderately inhomogeneous. Information such as the total fluid content, fluid viscosity and the permeability of the formation is of fundamental importance for oil recovery efficiency.

Estimating porosity independently from mineral content is an important application of NMR logs. The traditional method for estimating porosity uses a combination of neutron and density logs. This method depends on the lithology and requires a mineralogical correction for accurate porosity values (Luthi, 2001). In contrast, NMR porosity responds directly to the hydrogen content of the formation and thus is unaffected by the lithology effects encountered in density or neutron logging (Kenyon, 1997).

Permeability is usually derived from core-based porosity-permeability cross-plots. However, such an approach is often flawed by poor porosity-permeability correlations and sparse and expensive core data, as well.

The idea to use NMR for well logging dates back to the early 1950s when companies like Chevron, Mobil, Texaco, Borg-Warner but also Schlumberger and Varian started to study fluids in porous rocks. The first generation of commercial Nuclear Magnetic Logging (NML) tools operated in the earth's magnetic field and the first log was run in 1960 (Dunn et al., 2002). It was not until the 1990s that the second generation of commercial tools operated with pulse-echo NMR technology, permanent magnets, and a system providing controllable radio frequency magnetic pulses. This allowed relaxation measurements at low static magnetic field strength (Serra and Serra, 2004). The tools of the first and second generation were operated in wireline mode following the drilling of a borehole. They obtained the NMR information while being pulled up through the hole. The third generation tools perform logging while drilling (LWD). These tools are part of the drill string and suitable for directional drilling.

Within the past ten years, mobile magnetic resonance has moved from the oil field to many new areas of application (Blümich et al., 2004a; Blümich et al., 2005). While the focus of mobile NMR in the past was on single-sided or inside-out NMR (Blümich et al., 2004a and Blümich et al., 2004b), the emphasis is shifting to include the conventional outside-in NMR to mobile NMR where the object is inside a magnet with a use of tube-shaped Halbach magnets (Halbach, 1980; Raich and Blümmler, 2004). They are particularly useful where concentrations or amounts of a substance have to be quantified over a larger volume. This is a difficult and tedious task for single-sided instruments, because the sample is typically much bigger than the sensitive volume which then has to be positioned and calibrated with extreme care (Anferova et al., in press).

In the present thesis, different mobile NMR core-scanning devices were used for fast and non-destructive determination of porosity and for estimating pore size distribution and permeability on core plugs and drill cores. Previously, commercial portable systems allowed NMR measurements only on core plugs and drill cuttings (Mirotnik et al., 2004). In this

work, initially the unilateral NMR-MOUSE[®] (Mobile Universal Surface Explorer) (Eidmann et al., 1996) with a highly inhomogeneous static magnetic field was applied and later replaced by core-scanners with Halbach magnets (Anferova et al., 2004; Arnold et al., 2006; Anferova et al., in press) enclosing the entire sample. In this case, more homogeneous magnetic fields can be employed while the sensor is still mobile. The main advantage of these core-scanning devices is their small size, low weight, and mobility allowing field use such as on logging platforms and research vessels. Moreover, for samples of arbitrarily large dimensions, such as long drill core sections, NMR measurements by the unilateral NMR-MOUSE[®] and by the Halbach core-scanners are truly non-destructive, unlike other types of NMR. Hence, the NMR-MOUSE[®] and the Halbach core-scanners can be used to calibrate NMR logging data with core analysis data. Usually this is not done and NMR wireline logging data are compared only with laboratory NMR measurements on core plugs (Lonnes et al., 2003).

1.2 Objectives of this thesis

The main objective of the present thesis is to study the feasibility of newly developed mobile low-field NMR core-scanners in order to determine porosity routinely and to estimate pore size distribution and permeability on drill cores. The present thesis results from projects financed by the German Science foundation (DFG) (CL 121/16-1/2; BL 231/26-1/2; BL 231/31-1), within the DFG priority program ODP/IODP (Ocean Drilling Program/ Integrated Ocean Drilling Program).

Information on rock porosity and permeability is crucial for understanding mass and heat transfer of the sub-sea ocean floor and of large-scale solid earth cycles which are addressed in ODP/IODP initial science plan¹. The main source of information comes from downhole measurements and from cores recovered from the drilled cores (e.g. Arnold et al., submitted; Bartetzko et al., 2005; Bartetzko et al., 2003). At present, only rock porosity is measured routinely on board of ODP/IODP research vessels. There are no facilities for permeability measurements. Recent efforts are directed towards adapting NMR methods as a non-destructive approach also to ODP and the upcoming IODP program.

The DFG projects were handled in collaboration of the Applied Geophysics (AG) and the Institute of Macromolecular and Technical Chemistry (MC) at RWTH Aachen University. MC was responsible for the development of technical solutions and the adaptation of current NMR processing techniques. AG focused on the interpretation of NMR measurements with

¹ <http://www.iodp.org/isp/>

respect to rock porosity and permeability. Different mobile NMR core-scanners were developed by MC: the unilateral NMR-MOUSE[®] (Eidmann et al., 1996; Anferova et al., 2002; Anferova et al., 2004; Blümich et al., 2004 b; Arnold et al., 2006) with a strongly inhomogeneous static magnetic field and two Halbach core-scanners (Anferova et al., 2004; Arnold et al., 2006; Anferova et al., in press) which enclose the drill cores in a large and accessible cylindrical volume with a sufficiently homogeneous static magnetic field. The NMR-MOUSE[®] and the first version of the Halbach core-scanner are suitable for one-dimensional relaxation time measurements on drill cores. In a next step the Halbach core-scanner was improved to provide two-dimensional (2D) longitudinal and transverse relaxation time measurements simultaneously on core plugs.

All devices were tested by AG for their suitability to determine porosity and permeability on magmatic and sedimentary drill cores. Rocks studied are basalt, peridotite, limestone, and clay-rich sediments recovered from the Atlantic and Pacific ocean floor during ODP Legs (Shipboard Scientific Party, 2004a; Shipboard Scientific Party, 2004b; Shipboard Scientific Party, 2003; Shipboard Scientific Party, 1997a; Shipboard Scientific Party, 1997b; Shipboard Scientific Party, 1996; Shipboard Scientific Party, 1994) and a Meteor Cruise (Meteor-Bericht, 2003). Particularly, magmatic and mud formations are commonly not studied by NMR logging in the oil industry as they present no classical reservoir rocks compared to sandstone and carbonate formations. On the other hand no consolidated sandstones had yet been drilled in ODP/IODP. Hence, sandstone samples from the continental Allermoehe borehole (Northwest Germany) and from different outcrops in Germany were studied in addition with mobile NMR instrumentation. From the Allermoehe borehole, even NMR data is available allowing comparison between NMR core-scanner and logging data.

The NMR results were calibrated against a large collection of independent petrophysical data. Moreover, the precision and limits of the method were evaluated for different ranges of rock porosity, pore sizes, and content of ferromagnetic material with increased magnetic susceptibility.

Within the above mentioned projects, five scientific papers have been published or prepared on the design of mobile NMR instrumentation and its application on drill cores for the determination of porosity and permeability. The papers Arnold et al. (2006) and Pape et al. (manuscript in preparation) focus on porosity and permeability analysis by mobile NMR. The publications Blümich et al. (2004b), Anferova et al. (2004) and Anferova et al. (in press) are devoted to the technical construction of the different sensors.

1.3 Content of this thesis

The theoretical background of NMR with respect to petrophysical applications is introduced in Chapter 2. Chapter 3 deals with the mobile NMR equipment which was developed and tested during this study. Besides the size, weight and geometry of the different sensors, more details are discussed regarding the sensitive volume, operating frequency, and magnetic field strength and field gradients. Chapter 4 describes the core material studied and the applied measurement procedures including the NMR method and independent petrophysical studies. Chapter 5 is related to the determination of core porosity. Limits and accuracy of the different mobile NMR sensors are analyzed with respect to porosity ranges and various magnetic susceptibilities of the drill cores. Chapter 6 deals with the interpretation of relaxation measurements with respect to pore size distributions, studying the influence of external and internal magnetic field gradients. Standard permeability calculation schemes are applied for the interpretation of NMR measurements on drill cores representing classical reservoir rocks. In these cases, diffusion effects due to local field gradients are low and hence can be neglected. In addition, a newly developed model theory is used to obtain hydraulic effective pore radii from transverse relaxation time distributions. From these, permeability can be predicted accurately for sandstones with small pore sizes in spite of the influence of internal magnetic field gradients which is strongly enhanced here. Finally Chapter 7 summarizes the results obtained and provides conclusions and recommendations for future work.

2 Fundamentals of NMR petrophysics

Pulsed NMR measures the magnetization (M) and relaxation of hydrogen nuclei contained in the pore fluids. The magnetization is proportional to the number of hydrogen nuclei in the sensitive region of the sensor and can be scaled to provide a NMR porosity (Timur, 1969; Kenyon, 1992). In principle, the NMR porosity responds directly to the hydrogen content of the formation and thus is unaffected by the lithology effects in density and neutron logging (Kenyon, 1997).

The size distribution of fluid-filled pores is another essential information on rock samples which can be obtained from low-field NMR (Chen et al., 2002). In the following it is shown how this distribution and the NMR signal are related to each other.

2.1 Polarization

In a static magnetic field (B_0) protons tend to align themselves with the field and the nuclei spins will start to precess about the direction of the magnetic field. The Larmor equation (1) expresses the relationship between the strength of the magnetic field (B_0), and the precessional frequency (f), of an individual spin:

$$f = \frac{\gamma B_0}{2\pi}, \quad (1)$$

where γ is the gyromagnetic ratio, which is a measure of the strength of the nuclear magnetism. When a large number of spins are precessing about B_0 , most spins adopt the parallel rather than the antiparallel state. Hence, the net magnetization M_0 is in the direction of the B_0 field. The alignment of the spins which is called polarization gradually increase with a time constant which is the longitudinal relaxation time T_1 (Dunn et al, 2002):

$$M_z(t) = \frac{M_0(e^{\frac{t}{T_1}} - 1)}{e^{\frac{t}{T_1}}}, \quad (2)$$

where t is the time that the spins are exposed to the B_0 field, $M_z(t)$ is the magnitude of magnetization at time t , when the direction of B_0 is taken along the z -axis, and M_0 equals the

asymptotic and maximum magnetization in a given magnetic field. T_1 is also known as the spin-lattice relaxation time, and characterizes the alignment of spins with the external static magnetic field (Figure 1).

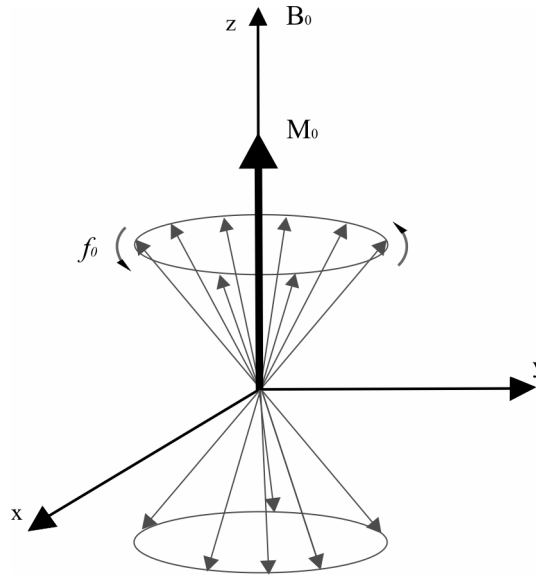


Figure 1: Net magnetization (M_0) resulting from the precession of proton spins about an external magnetic field (Coates et al., 1999).

2.2 Pulse tipping and free induction decay

After the spins are polarized, the next step is to tip the aligned proton spins from the longitudinal direction to a transverse plane by transmitting an oscillating radio frequency magnetic field (B_1), perpendicular to the direction of the static magnetic field (B_0). The frequency of B_1 needs to be equal the precessing frequency of the spins in order to ensure to effective tipping. This frequency is called Larmor frequency which is the resonance frequency of the magnetic nuclei. Application of the oscillating magnetic field (B_1) moves the spins to a higher energy level and makes them precess in phase with each other. This process is called Nuclear Magnetic Resonance.

The angle through which the magnetization has rotated away from the z-axis (compare Figure 2) is known as ‘flip angle’ or ‘tip angle’ and is given by:

$$\theta = \gamma B_1 \tau, \quad (3)$$

where θ is the tip angle (degrees), B_1 is the amplitude of an oscillating field and τ is the time over which the oscillating field is applied (pulse length of the NMR experiment). The strength and duration of B_1 determine the amount of energy available to achieve spin transitions between parallel and anti-parallel states. Thus, the flip angle is proportional to the strength and duration of B_1 (Coates et al., 1999).

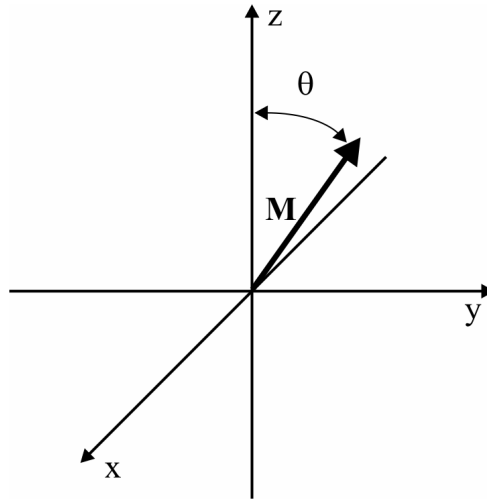


Figure 2: Nuclear magnetization M can be rotated away from the direction of B_0 . The angle θ between the z -axis and the magnetization is called ‘flip angle’.

In NMR tools, the net magnetization is normally tipped at angles of $\theta = 90^\circ$ and $\theta = 180^\circ$. When a 90° pulse is applied, the polarized proton spins start to precess in phase in a transverse plane. But after the B_1 field has been turned off, the spins dephase over a time T_2 which characterizes the loss of phase coherence due to interactions between the spins. Hence, T_2 is also known as spin-spin relaxation time. The amplitude of the spin-echo train at time t , which is the amplitude of the transverse magnetization $M_{xy}(t)$, is given by:

$$M_{xy}(t) = M_{0xy} e^{\frac{-t}{T_2}}, \quad (4)$$

where M_{0xy} is the magnitude of the transverse magnetization at $t = 0$ (the time at which the 90° pulse ceases). During dephasing, the net magnetization decreases. Such a reduction in magnetization (decay) is usually exponential and is called Free Induction Decay (FID) (Figure 3).

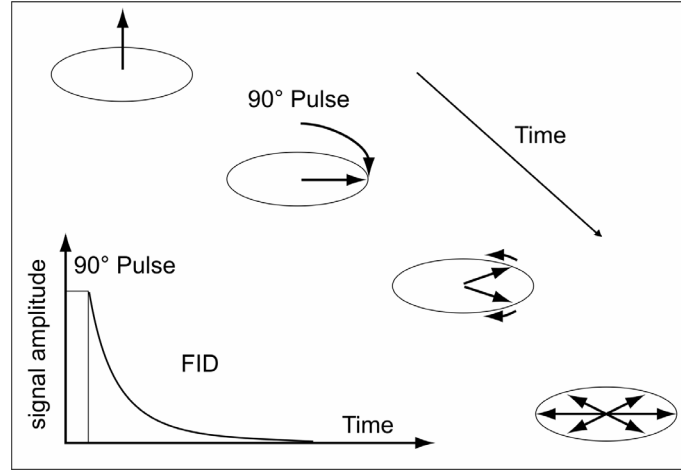


Figure 3: After application of a 90° rf pulse, the proton spins dephase, and a free induction decay (FID) signal can be detected (after Coates et al., 1999).

2.3 Relaxation mechanisms in porous media

For fluids in rock pores, three different mechanisms acting in parallel are involved in relaxation (Coates et al., 1999):

$$\frac{1}{T_{1A}} = \frac{1}{T_{1F}} + \frac{1}{T_{1S}} \quad (5)$$

$$\frac{1}{T_{2A}} = \frac{1}{T_{2F}} + \frac{1}{T_{2S}} + \frac{1}{T_{2D}} \quad (6)$$

where the subscripts A, F, S, and D denote apparent, free fluid, surface-induced, and diffusion-induced mechanisms, respectively. The free fluid relaxation time (about 3 seconds) is a property of the fluid only and affects both T_1 and T_2 relaxation. In contrast, water in the pore space of a rock has apparent T_1 and T_2 relaxation times typically varying from one to several hundred milliseconds (Dunn et al., 2002). Therefore, the contribution from the free fluid in equations (5) and (6) can be neglected. The surface-induced relaxation which affects both T_1 and T_2 relaxation is due to interaction between the fluid and the solid surface. In contrast, the diffusion-related relaxation which affects only the T_2 relaxation arises from internal magnetic field gradients due to magnetic susceptibility contrast between grains and pore fluid or from inhomogeneities in the applied B_0 field. The surface and diffusion-induced relaxation rates are given by (Cohen and Mendelsohn, 1982):

$$\frac{1}{T_{1S}} = \rho_1 \frac{S}{V} \quad (7)$$

$$\frac{1}{T_{2S}} = \rho_2 \frac{S}{V} \quad (8)$$

$$\frac{1}{T_{2D}} = \frac{[(\gamma G t_E)^2 D_0]}{12} \quad (9)$$

where ρ_1 and ρ_2 are the surface relaxivity values corresponding to T_1 and T_2 , respectively. Surface relaxivity is a measure of how quickly proton spins lose orientation or phase coherence due to magnetic interactions at the fluid-solid interface. It is dominated by paramagnetic ions in the grain surfaces (Kleinberg et al., 1994). Surface relaxation ρ falls in the range of approximately 3 $\mu\text{m/s}$ to 30 $\mu\text{m/s}$ for clastics and is smaller for carbonates (Coates et al., 1999). S/V is the surface-to-volume ratio. For spherical pores $S/V = 6/d$, where d is the pore diameter. G is the gradient of the magnetic field (T/m), γ the gyromagnetic ratio, t_E the inter-echo spacing used in the pulse sequence, and D_0 the self-diffusion coefficient of the liquid (m^2/s).

Typical reservoir rocks belong to the ‘fast-diffusion’ relaxation regime (Brownstein and Tarr, 1979) in which the relaxation at the surface is slower than the transport of the hydrogen nuclei to the surface. Thus, the spins experience a rapid exchange of environments so that the local fields in each region of a pore are averaged to their mean value. As a consequence, a single exponential decay is observed for a given pore, and the rate of magnetization decay depends on surface to volume ratio only (Kleinberg et al., 1994). In the ‘slow diffusion’ limit, in contrast, the magnetization decay is multi-exponential and depends on the pore geometry. For low magnetic field strength (and thus small G) and at short t_E (Kleinberg and Horsfield, 1990), the contribution to T_2 decay times provided by the diffusion in the inhomogeneous local magnetic fields is negligible to that by surface relaxation. Therefore, the measured T_1 and T_2 values can be approximated:

$$\frac{1}{T_{1A}} = \rho_1 \frac{S}{V} \quad (10)$$

$$\frac{1}{T_{2A}} = \rho_2 \frac{S}{V} \quad (11)$$

Equations (10) and (11) form the basis of NMR core analysis and log interpretation: T_1 and T_2 are proportional to V/S , which in turn is proportional to pore size. This means that relaxation is faster in small pores than in large pores.

2.4 T_2 measurements

Both T_1 and T_2 are important in logging. In continuous logging, it is more practical to measure T_2 relaxation because it can be obtained quicker than T_1 . Thus it provides smaller bed boundary effects and a better vertical resolution. Besides, higher measurements repetition rates increase the signal-to-noise ratio (Kenyon, 1997).

The increase in the measured transverse magnetization signal induced by repeated rf-pulses is observed as a phenomenon which is called spin echo. It was first discovered by Hahn in 1950 (Hahn, 1950). The Hahn echo decay is the basic spin echo sequence to measure T_2 (Figure 4). It consists of a 90° pulse followed by a 180° pulse after the delay time τ . When hydrogen spins are tipped 90° from the direction of the magnetic field, they precess and dephase due to the inhomogeneity of the magnetic field. The spins can be refocused by transmission of a 180° pulse. As the spins rephase, they generate a signal in a receiver coil - a spin echo. T_2 can be measured by performing successive measurements for different values of τ .

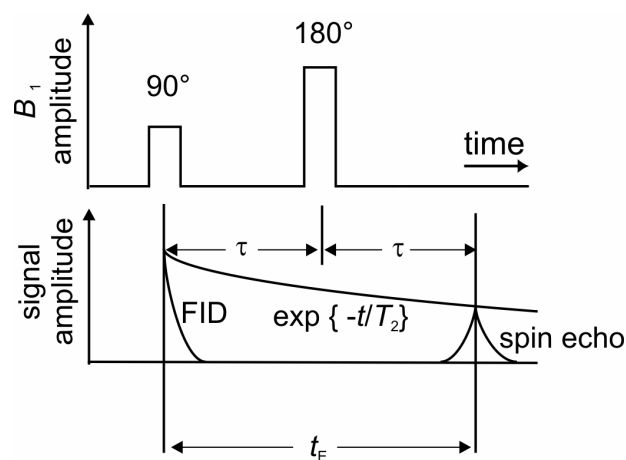


Figure 4: Hahn echo decay pulse sequence to measure T_2 ; FID is the free induction decay, τ delay time between the two pulses and t_E is the inter-echo spacing used in the pulse-sequence.

Another pulse sequence to measure transverse magnetization is the CPMG sequence (Carr and Purcell, 1954; Meiboom and Gill, 1958) which was used in this study (Figure 5). It consists of one 90° pulse followed by a series of 180° pulses after the delay time τ . The time interval between two 180° pulses is the echo time t_E which is equal to 2τ . The time between two sequences is the recovery time t_R ; it must be sufficiently long so that magnetization has decayed completely to equilibrium. The advantage of the CPMG pulse sequence is the much shorter time required to measure at multiple echo times as the 180° pulses can be applied repeatedly to produce a series of echo trains. With the Hahn sequence, in contrast, only one echo can be measured. Therefore much more sequences are needed to get the same amount of echoes (Flikweert, 2003).

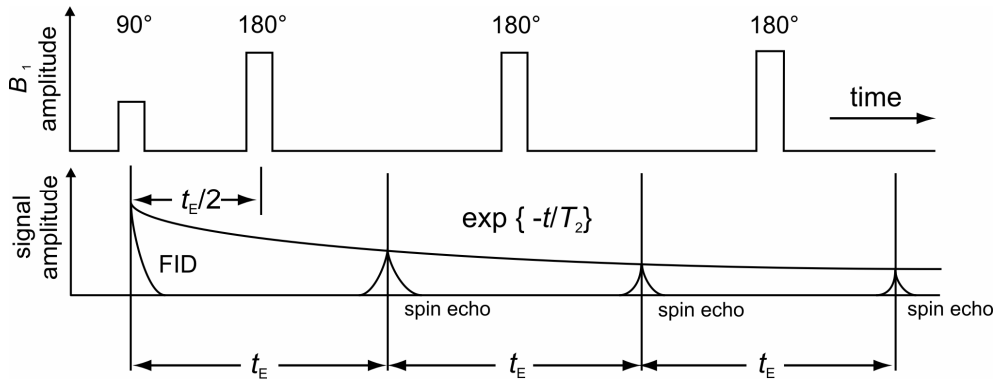


Figure 5: CPMG sequence for detection of the signal decay by the NMR core-scanners; FID is the free induction decay, t_E echo time and T_2 transverse relaxation time. Due to its strong magnetic field gradient, the NMR-MOUSE[®] measures $T_{2,\text{eff}}$ instead of T_2 (cf. Chapter 3.1).

In the fast diffusion limit and for a sample with a distribution of N different pore sizes, the transient variations of the transverse magnetization $M_{xy}(t)$ can be expressed as a sum of exponentials:

$$M_{xy}(t) = \sum_{i=1}^N M_{xy,i} e^{-\frac{t}{T_{2,i}}}, \quad (12)$$

which shows that the overall decay is the sum of the individual decays. For a vanishing magnetic field gradient, i.e. $G = 0$, the spectrum or distribution $P(T_{2i})$ of relaxation times T_{2i} is a direct map of the pore size distribution $P(d)$ with $T_2 \sim V/S \sim d$, where the distribution functions P represent probability densities. Proper fitting routines are used to fit a sum of decay exponents (each with a different decay constant) to the envelope of the echo

trains from core samples. All of the decay constants make up the decay time spectrum or the relaxation time distribution (Blümich et al., 2004b) (Figure 6). Two different fit analysis were used in this study to obtain the distribution of transverse relaxation times T_2 : a Matlab code based on the approach of lognormal distributed pore radii and thus relaxation times (written by Hartmann; personal communication, 2005) and a regularized inverse Laplace transformation based on the UPEN program, (Borgia, 1998). The obtained distributions are in good agreement. The Matlab fitting routine restricts the relaxation time distribution to a multimodal lognormal distribution. A nonlinear least square routine is used to fit the simulated decay time spectrum to the original data points. Thus, the model parameters (standard deviation and expected values of the lognormal distributions) are obtained that yield the curve closest to the data points. This method has the advantage that reliable results can even be obtained when measurements are performed with a low signal to noise ratio.

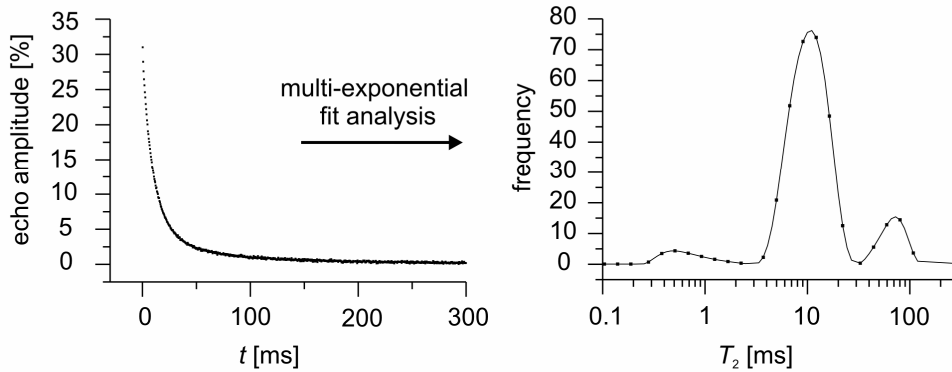


Figure 6: CPMG echo envelope measured on a water-saturated sediment sample (left) and corresponding frequency distribution of T_2 obtained by regularized inverse Laplace transformation with the UPEN program (Borgia, 1998).

2.5 T_1 measurements

The longitudinal relaxation time T_1 is the recovery time of the longitudinal component of the magnetization M_z to its equilibrium value M_0 . Two common pulse sequences are used to measure T_1 : the *saturation recovery* and the *inversion recovery* (Dunn et al., 2002).

In the saturation recovery (cf. Figure 7) M_z is initially destroyed by a series of aperiodic 90° pulses, whereas the inversion recovery sequence starts with a 180° pulse which rotates M_z from the positive to the negative z-axis. Immediately after the stimulus, the spins start to flip back at the rate of T_1 . Then a Hahn echo sequence with a short echo time t_E is applied after the recovery time τ_1 . By recording the echo signal intensity as a function of

continuously increasing recovery time τ_1 , it is possible to follow the longitudinal magnetization. The magnetization recovery curves are described by the following equations (Dunn et al., 2002):

$$\text{Saturation recovery: } M_z(t) = M_0(1 - e^{-\frac{t}{T_1}}). \quad (13)$$

$$\text{Inversion recovery: } M_z(t) = \frac{M_0(e^{\frac{t}{T_1}} - 2)}{e^{\frac{t}{T_1}}}, \quad (14)$$

For a correct determination of T_1 , the maximum value of τ_1 has to be at least 5 times T_1 .

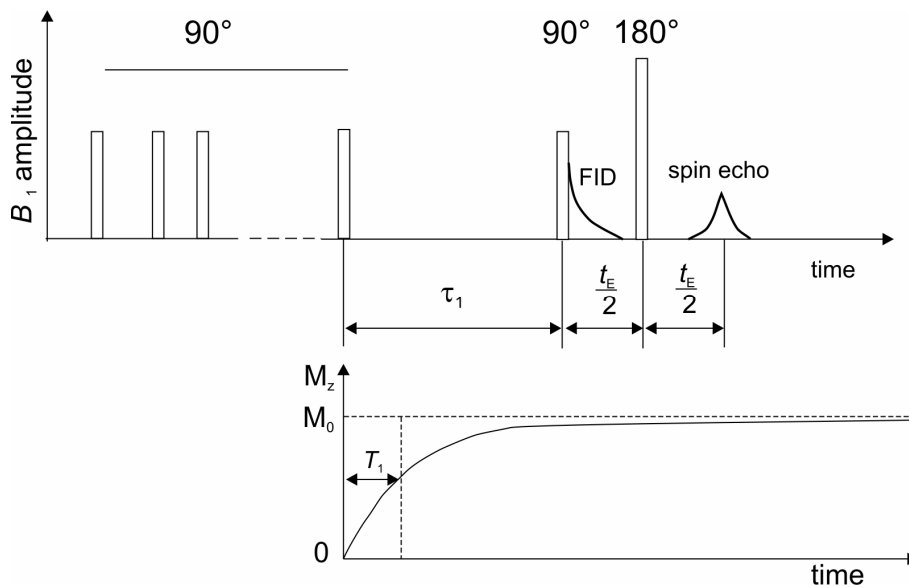


Figure 7: Saturation recovery pulse sequence to measure the longitudinal relaxation time T_1 which is the recovery time of the longitudinal component of the magnetization M_z to the equilibrium value M_0 (1-1/e); τ_1 is recovery time and t_E echo time.

2.6 2D T_1 - T_2 correlation measurements

Homogeneous static magnetic fields, the CPMG pulse sequence, short echo times, and low Larmor frequencies can be used to minimize diffusion effects on T_2 distributions. However, internal magnetic field gradients which are difficult to characterize occur at the pore scale and cannot be eliminated completely (Dunn et al., 2002).

2D T_1 - T_2 relaxation correlation experiments can be performed to test the influence of diffusion on the shape of the T_2 distribution function, (Anferova et al., 2007). The T_1/T_2 ratio

indicates the attenuation of the transverse magnetization by diffusion in the internal gradients which are proportional to the applied magnetic field.

Examples of simple pulse sequences are the inversion or saturation recovery filters followed by a CPMG detection for correlating T_1 and T_2 (Figure 8). Since 2002, both types of 2D sequences are being used on Logging While Drilling (LWD) tools (Darling, 2005). When applying the pulse sequence shown in Figure 8 (Hürlimann and Venkataramanan, 2002; Song et al., 2002), the measured magnetization $M(\tau_1, n_j, t_E)$ of the water protons in the saturated rock matrix depends on the longitudinal relaxation time T_1 and the transverse relaxation time T_2 ,

$$M(\tau_1, n_j, t_E) = \iint dT_1 dT_2 f(T_1, T_2) k_1(T_1, \tau_1) k_2(T_2, n_j, t_E), \quad (15)$$

where τ_1 is the saturation recovery time, n_j is the number of echoes and t_E is the echo time. The 2D distribution function $f(T_1, T_2)$ follows from equation (15) by 2D inverse Laplace transformation, using the two-dimensional inversion routine (Godefroy and Callaghan, 2003):

$$M(\tau_1, n_j, t_E) \xrightarrow[\text{LP}]{\text{2D}} f(T_1, T_2) k_1(T_1, \tau_1) k_2(T_2, n_j, t_E) \quad (16),$$

where the kernels k_1 and k_2 for the pulse sequence are given by:

$$k_1(T_1, \tau_1) = 1 - \exp\left\{-\frac{\tau_1}{T_1}\right\} \quad (17)$$

and

$$k_2(T_2, n_j, t_E) = \exp\left\{-\frac{n_j t_E}{T_2}\right\}. \quad (18)$$

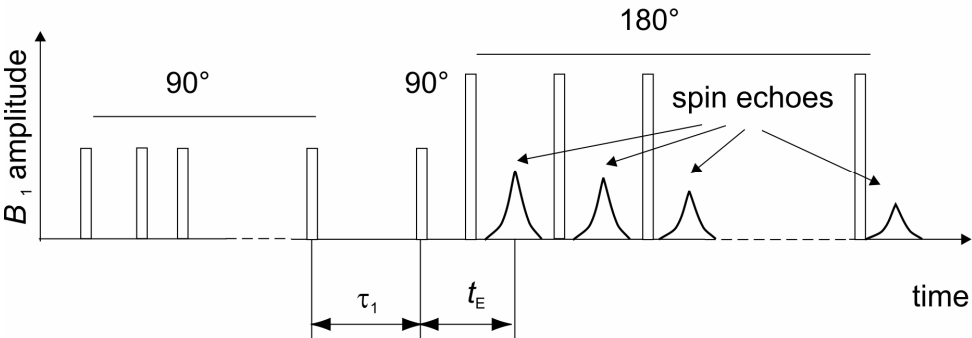


Figure 8: Pulse sequence for measuring T_1 - T_2 relaxation correlation; τ_1 is saturation recovery time and t_E echo time.

3 Mobile NMR instrumentation

In the following, mobile NMR devices which were applied in this work are briefly described. All sensors are combined with a mobile NMR spectrometer and a laptop computer.

3.1 NMR-MOUSE[®]

The unilateral NMR-MOUSE[®] (Eidmann et al., 1996; Anferova et al., 2002; Anferova et al., 2004; Blümich et al., 2004 b; Arnold et al., 2006) has a flat surface that can be placed on the object for measurements (Figure 9). It is a portable, palm-sized device weighting 2.5 kg, constructed from a figure 8 rf-coil and a U-shaped magnet (Figure 10). It produces a static magnetic field B_0 of 0.5 T. A rf field B_1 with frequency of 21.1 MHz provides a signal penetration of 3 mm into the core sample. The magnetic field of the NMR-MOUSE[®] is highly inhomogeneous with a gradient of about 12 T/m within the sensitive volume of about 0.1 cm³. Because of its small sensitive region, the device can be used to determine local heterogeneities in the samples. As the sensitive volume probed by the NMR-MOUSE[®] is well defined for a given profile of B_0 and B_1 fields and given pulse sequence parameters, NMR porosity data normalized to a unique pure water measurement can be compared quantitatively, irrespective of the sample size. Due to the inhomogeneous magnetic field of the NMR-MOUSE[®], the decay of the echo envelope is affected additionally by diffusion in the probe's extremely high magnetic field gradient. It is also distorted by a superposition of T_2 and T_1 effects because the magnetic B_1 field gradient results in a distribution of flip angles rather than a single flip angle. The resultant decay time constant is denoted by $T_{2,\text{eff}}$ instead of T_2 (Hürlimann and Griffin, 2000).

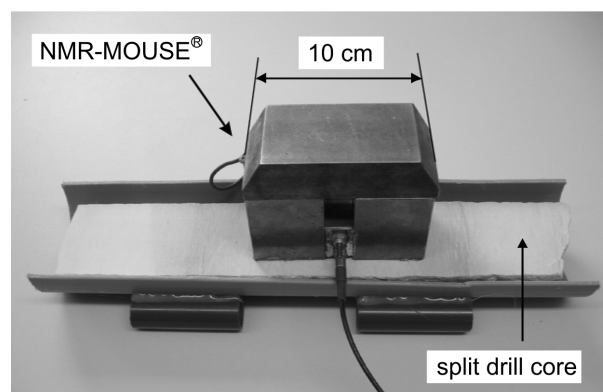


Figure 9: NMR-MOUSE[®] in place for measurement on a drill core section.

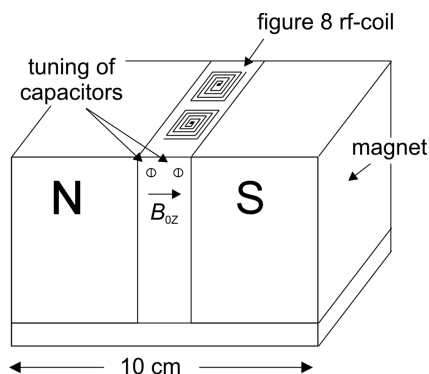


Figure 10: Schematic drawing of the NMR-MOUSE[®]. This core-scanner is constructed from two permanent magnets mounted on an iron yoke with anti-parallel polarization. The rf field B_1 is generated by a figure-8 rf-coil placed in the gap. Two capacitors can be tuned to adjust the resonance frequency and to match the output impedance of the probe with the 50Ω impedance of the spectrometer.

3.2 Halbach core-scanner

In a next step, a mobile NMR core-scanner with a Halbach magnet was applied for measurements of porosity and pore-size distributions on water-saturated cylindrical drill cores with diameters up to 60 mm. It is light (~ 8 kg) and has a sufficiently homogeneous magnetic field in a large, accessible cylindrical volume.

The Halbach core-scanner (Anferova et al., 2004; Arnold et al., 2006) encloses the drill core in six magnet rings. Each magnet ring consists of 16 bar magnets ($18 \times 18 \times 27 \text{ mm}^3$) and has an inner diameter of 70 mm and an outer diameter of 155 mm. The entire magnet system is 165 mm long. It produces a static magnetic field B_0 of 0.3 T corresponding to a resonance frequency of 12.74 MHz for spins of hydrogen nuclei. The estimated gradient of the magnetic field within the sensitive volume of 60 mm diameter and 60 mm height is less than 0.3 T/m. The device can be used for certain sample geometries in combination with exchangeable rf-coils (Anferova et al., 2004). On the one hand a surface rf-coil is used, which is suitable for standard ODP/IODP cores. They have a diameter of 60 mm and are split right after recovery into semi-cylinders. On the other hand measurements use a solenoidal rf-coil for full-cylindrical cores with diameters of up to 60 mm. A schematic drawing and a photo of the Halbach core-scanner are shown in Figure 11 and Figure 12.

As the magnetic field of the Halbach magnet is normal to the cylinder axis, simple solenoidal rf coils, centered around the cylinder axis, can be employed and the magnet can be used on long cylindrical objects. Besides, the ideal Halbach magnet can be constructed from small magnet blocks (Raich and Blümler, 2004) of light weight and low cost with a magnetic

field sufficiently homogeneous and strong for various NMR applications. A further advantage is the very weak stray field of such a magnet which does not affect motors and other ferromagnetic parts in its vicinity.

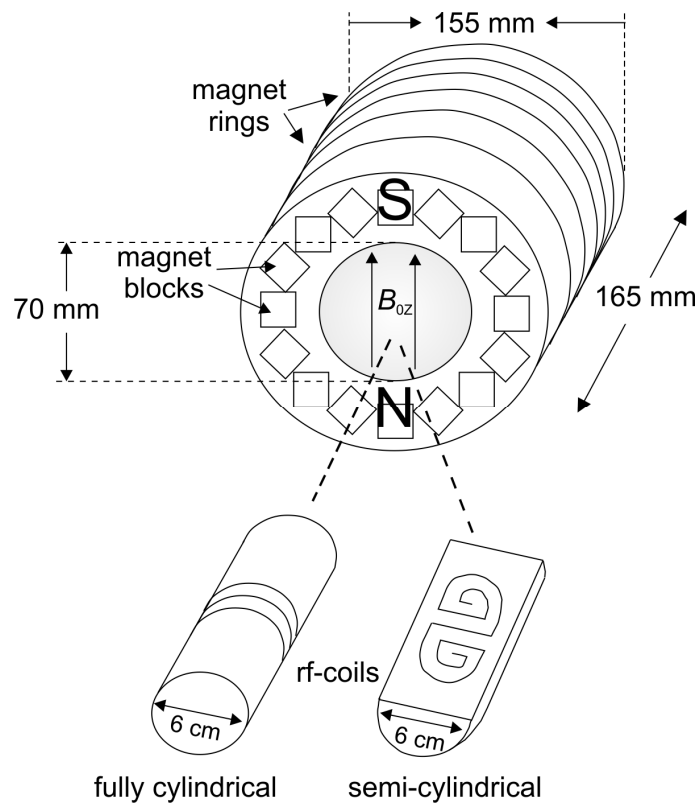


Figure 11: Schematic drawing of the Halbach core-scanner with two different coils for fully cylindrical or split, semi-cylindrical cores with diameters of up to 60 mm.

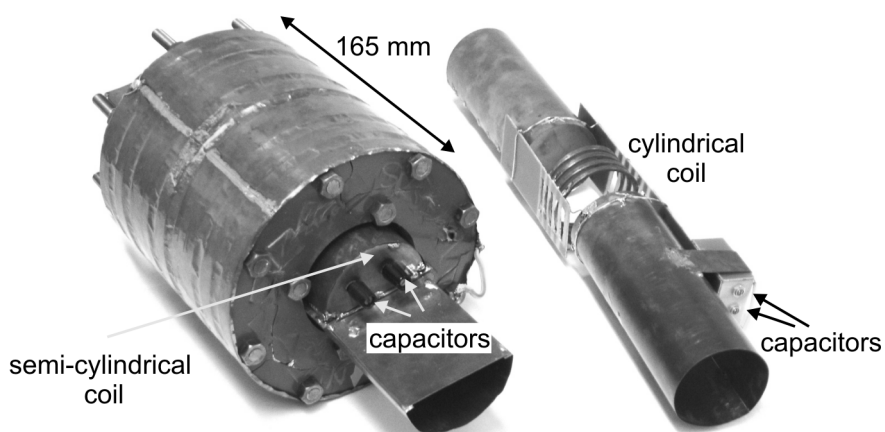


Figure 12: Photo of the Halbach core-scanner with the semi-cylindrical coil in its center. This can be changed for the fully cylindrical coil on the right. Two capacitors are shown at each coil: one to tune the resonance frequency and the other one to match the output impedance of the probe with the $50\ \Omega$ impedance of the spectrometer.

Measurements with the NMR-MOUSE[®] are performed at higher frequencies increasing the signal-to-noise ratio. However, the signal received from a sample measured with the Halbach core-scanner is much stronger. This is due to the sensitive volume of the Halbach core-scanner which is more than 100 times larger than that of the NMR-MOUSE[®]. The signal-to-noise ratio which is valid for inside-out NMR experiments was initially formulated by Abragam (1961) and the analyses extended by Hoult and Richards (1976). Perlo (2006) modified the analytical expression for single-sided NMR measurements associated with highly inhomogeneous fields. To achieve the same signal-to-noise ratio with the NMR-MOUSE[®], the number of scans has to be increased by a factor of 100 as the signal-to-noise ratio (S/N) is proportional to the sensitive volume V of the core scanning device and the square root of the number of scans n ($S/N \sim V n^{1/2}$) (Hoult and Richards, 1976). Hence, measurements with the NMR-MOUSE[®] require accordingly more time than those with the Halbach core-scanner.

A further advantage of the Halbach core-scanner compared to the NMR-MOUSE[®] is the use of a weaker magnetic field B_0 : The background local magnetic field gradients which result from the magnetic susceptibility differences between grain materials and pore fluid are proportional to the overall field strength of the magnet.

3.3 Improved Halbach core-scanner

A second version of the Halbach core-scanner (Anferova et al., in press) was constructed later on with an even more homogeneous magnetic field and an increased sensitive volume (Figure 13). The magnet system consists of two Halbach arrays separated by an axial gap of 10 mm. Each Halbach array contains three stacked magnet rings, which consist of 16 magnet blocks with dimensions of 30 mm³. The magnet blocks are arranged in a circle with an inner diameter of 140 mm and an outer diameter of 260 mm. The magnet system produces a magnetic field of $B_0 = 0.22$ T, corresponding to a proton (¹H) resonance frequency of 9.6 MHz. The estimated average gradient of the magnetic field within the central sensitive cylindrical volume of 20 mm diameter and 20 mm length is about 0.05 T/m. A cylindrical rf coil with 24 mm diameter and 12 mm length which matches a region of the most homogenous magnetic field is used for the more demanding measurements in 2D T_1 - T_2 correlation experiments and PFG experiments. The average field gradient of the magnetic field along the cylinder axis in the sensitive cylindrical volume of 40 mm diameter and 80 mm length is lower than 0.15 T/m and sufficiently small for T_2 measurements. Exchangeable cylindrical rf coils with diameters of 64 mm and 82 mm and a surface figure-8

rf coil with a diameter of 60 mm are available for T_2 measurements. Cylindrical and figure-8 rf coils are suitable for analysis of full and split cores, respectively.

The Halbach core-scanner was furnished with a sliding table for automatic scans of porosity along long drill core sections (Figure 14). The drill cores can be placed inside a fixed plastic tube with an inner diameter of 64 mm and a length of 2.2 m. The Halbach core-scanner is then moved along the fixed core by a computer-controlled stepping motor.

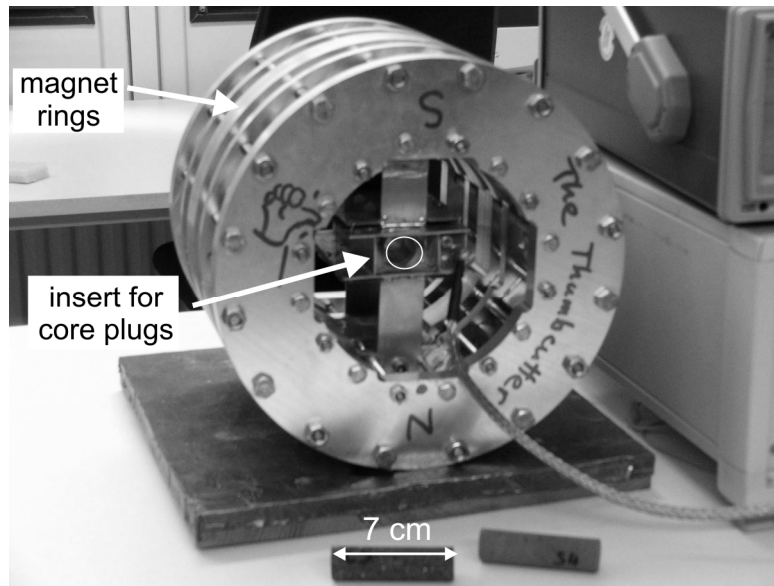


Figure 13: Photo of the improved Halbach core-scanner with an inner diameter of 140 mm and combined with a special insert for core plugs with a diameter of 20 mm.

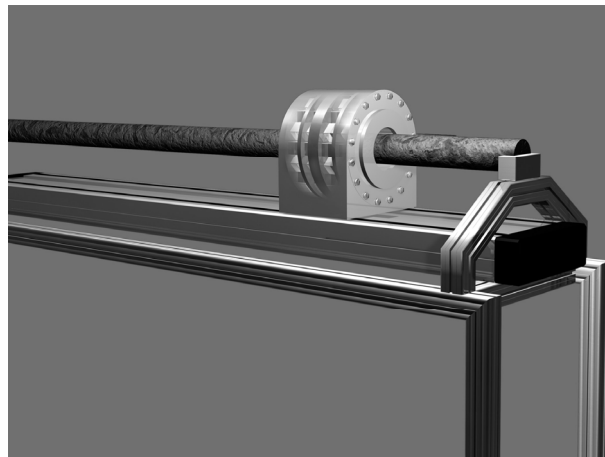


Figure 14: Core-scanner with a sliding Halbach magnet for automatic NMR scanning of cylindrical drill cores.

4 Samples and experimental procedures

4.1 Sample selection

A total of 34 fully cylindrical and split semi-cylindrical drill cores of diameters between 50 mm and 60 mm and 30 core plugs of 20 mm in diameter were used in this study. They represent different rock types: Sandstone and shale from continental outcrops and boreholes located in Germany, and limestone, clay-rich sediment and basalt from boreholes drilled into the Atlantic and Pacific oceanic crust. Origin and type of the studied rock samples are shown in Table 1. Table 2 displays images of cores and plugs which are representative for each geological environment. The samples differ in porosity (2 % - 33 %), permeability ($< 0.0001 \text{ mD} - 2205 \text{ mD}^2$) and magnetic susceptibility ($-13 \times 10^{-6} \text{ SI} - 13 \times 10^{-3} \text{ SI}$). Magnetic susceptibility of the samples is given in Table 1.

Core samples were available from the Allermoehe borehole. It is located in the northern German sedimentary basin near Hamburg and drilled into the Rhaetian hydrothermal aquifer that is considered a geothermal resource. Rhaetian sandstones were cored in the depth interval between 3220 m und 3250 m. From the same depth interval, additional NMR logging data are available which was recorded by Schlumberger's CMR (Combinable Magnetic Resonance) tool. Aside a few split cores with diameters of 50 mm measured with the NMR-MOUSE[®] and the first version of the Halbach core-scanner, 20 core plugs with diameters of 20 mm were studied with the improved Halbach core-scanner for comparative studies between NMR core-scanner and NMR logging data. The chosen core material is classified as fine-grained sandstone with a high quartz content. Compared to other parts of the formation, the available core plugs contain no anhydrite cementation.

Eleven sandstone samples collected from outcrops located in different parts of Germany (Bad Bentheim, Barkhausen, Cotta, Ibbenbüren, Obernkirchen, Bad Karlshafen, Sand, Schleerieth, Velpe, Züschen, and Ettlingen) were studied with the improved Halbach core-scanner. For NMR measurements core plugs with a diameter of 20 mm were used. The sandstone samples were chosen to cover a wide range of permeability.

The geothermal drilling project of the SuperC student centre at RWTH Aachen University provided the opportunity to measure fully saturated cores right after drilling.

² 1 mD $\sim 10^{-15} \text{ m}^2$

Light-weight NMR equipment including the first version of the Halbach core-scanner, a portable NMR spectrometer and a laptop computer operated next to the drilling platform of the RWTH-1 borehole³. The cylindrical drill cores had a diameter of 50 mm and were recovered from a depth of around 1460 m. Drill cores consisted of shale with very low porosity and permeability (Kukla and Trautwein-Bruns, 2006).

To test the applicability of the mobile NMR instrumentation for drill cores recovered within ODP/IODP, cores from several ODP Holes were studied with the first version of the Halbach core-scanner:

ODP Holes 917A and 989B drilled during ODP Legs 152 and 163 are located on the Eastern and Southeastern Greenland Shelf, respectively, approximately 50 km from the coast. The studied drill cores were recovered from depth intervals between 80 mbsf and 800 mbsf (Hole 917A) and between 5 mbsf and 50 mbsf (Hole 989B). They represent vesicular and aphyric basalt emplaced as lava flows and probably weathered in a subaerial environment (Shipboard Scientific Party, 1994; Shipboard Scientific Party, 1996).

ODP Hole 999B drilled during ODP Leg 165 is located in the Colombian Basin (Caribbean Sea). Studied drill cores were recovered from a depth interval between 870 mbsf and 930 mbsf and are classified as light gray, calcareous limestone with some interbedded dark gray volcanic ash layers (Shipboard Scientific Party, 1997a).

ODP Hole 1005C was drilled during ODP Leg 166 and is positioned in the Great Bahama Bank. The studied cores were drilled between a depth of 515 mbsf and 700 mbsf. They are described as fine-grained, brownish gray foraminiferous wackestones. Some bioclasts are preserved as molds. The cores are characterized by alternating intervals of light, well cemented, non-compacted sediments and dark, less-cemented, compacted zones. Contacts between these zones are gradational (Shipboard Scientific Party, 1997b).

ODP Holes 1244C and 1244E were cored during ODP Leg 204. They are positioned in the Cascadia accretionary complex (Hydrate Ridge) on the Oregon continental margin, offshore Oregon (Shipboard Scientific Party, 2003). Studied cores were recovered from a depth interval between 10 mbsf and 216 mbsf. The lithology at both holes is similar, characterized by brownish gray hemipelagic clay interlayered with silts and volcanic ash layers.

ODP Holes 1274A and 1275B drilled during ODP Leg 209 are positioned along the Mid-Atlantic Ridge from 14° N to 16° N. Drilling recovered substantial proportions of

³ <http://www.superc.rwth-aachen.de>

4 Samples and experimental procedures

gabbroic rocks intruded into mantle peridotite (Shipboard Scientific Party, 2004a). The studied cores were recovered at ~ 31 mbsf in Hole 1274A and at ~ 93 mbsf in Hole 1275B.

ODP Hole 1277A cored during ODP Leg 210 is located in the Newfoundland rift (Shipboard Scientific Party, 2004b). The studied core is recovered from a depth at around 151 mbsf. It is classified as a serpentinized peridotite with veins of gabbro.

In addition cores from Hole GeoB 8627-1 cored during Meteor Cruise M58/2 were studied with the NMR-MOUSE[®] at Bremen University. The cores have a diameter of 50 mm and are split into semi cylinders. Hole GeoB 8627-1 is located at the continental slope near Dakhla off northwestern Africa. The cores were recovered within a depth range of 0 mbsf and 12 mbsf and are classified as olive gray foraminifera bearing mud (Meteor-Bericht, 2003).

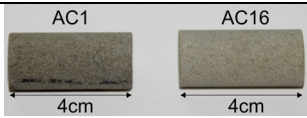
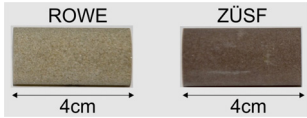
Table 1: Borehole and outcrop table, location, rock type, and range of magnetic susceptibility of samples used in this study (SI units are used).

Borehole/Outcrop/ Leg	Location	Rock type	Magnetic susceptibility $\times 10^{-6}$ [SI]
Allermoehe borehole	Northern German Sedimentary Basin	sandstone	0 - 25
RWTH-1 Borehole	RWTH Aachen University (Germany)	shale	60 - 130
ODP Leg 152, Hole 917A	Eastern Greenland shelf	basalt	2900 - 13000
ODP Leg 163, Hole 989B	Southeastern Greenland margin	basalt	5000 - 7300
ODP Leg 165, Hole 999B	Caribbean Sea, Colombian Basin	limestone, with volcanic ash layers	0 -190 up to 2000 (ash layers)
ODP Leg 166, Hole 1005C	Great Bahama Bank	limestone	0 - 40
ODP Leg 204, Holes 1244C & 1244 E	Hydrate Ridge, Cascadia Continental Margin	clay-rich sediment	250 - 380
ODP Leg 209, Hole 1274A Hole 1275B	Mid-Atlantic Ridge from 14° to 16° N	peridotite gabbro	5000-10000 30000 - 70000
ODP Leg 210, Hole 1277A	Newfoundland rift	peridotite	15000 - 27000
Meteor Leg 58/27, GeoB 8627-2	Shelf near Dakhla, Northwestern Africa	clay-rich sediment	0 - 130


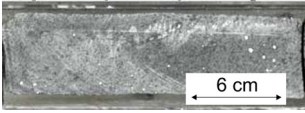
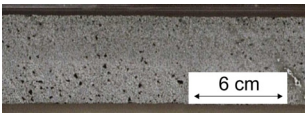
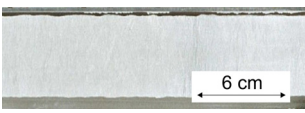


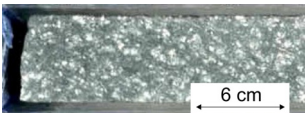
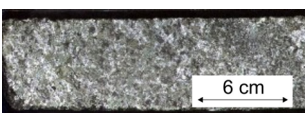
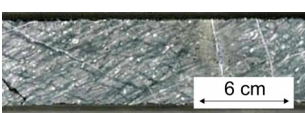
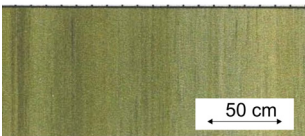
4 Samples and experimental procedures

Borehole/Outcrop/ Leg	Location	Rock type	Magnetic susceptibility $\times 10^{-6}$ [SI]
Outcrop Bad Bentheim	Bad Bentheim, Germany 52°18'37 N, 7°15'02 E	sandstone	-10
Outcrop Barkhausen	Barkhausen, Germany 52°17'03 N, 8°24'36 E	sandstone	150
Outcrop Cotta	Cotta, Germany 50°56'55 N, 14°0'39 E	sandstone	13
Outcrop Ibbenbüren	Ibbenbüren, Germany 52°16'50 N, 7°43'59 E	sandstone	5
Outcrop Obernkirchen	Obernkirchen, Germany 52°15'47 N, 9°12'31 E	sandstone	-13
Outcrop Bad Karlshafen	Bad Karlshafen, Germany 51°39'06 N, 9°26'30 E	sandstone	100
Outcrop Sand	Sand, Germany 49°58'39 N, 10°35'25 E	sandstone	105
Outcrop Schleerieth	Schleerieth, Germany 50°01'12 N, 10°05'26 E	sandstone	245
Outcrop Velpe	Velpe, Germany 52°25'10 N, 10°56'30 E	sandstone	-8
Outcrop Züschen	Züschen, Germany 51°10'47 N, 9°14'01 E	sandstone	13
Outcrop Ettlingen	Ettlingen, Germany 54°23'94 N, 34°58'58 E	sandstone	2

Table 2: Images from representative cores (one core per borehole) and plugs used in study; laboratory labels, rock classifications and core or plug diameters are given.

Laboratory label	Images of typical core or plug	Rock classification	Core or plug diameter in mm
Allermoehe, AC1, AC16		sandstone	20
Outcrops, ROWE, ZÜSF		sandstone	20

4 Samples and experimental procedures

Laboratory label	Images of typical core or plug	Rock classification	Core or plug diameter in mm
RWTH-1, C28-2		shale	50
ODP Leg 152, Hole 917A, 101 R, 4W, 22 cm - 42 cm		Vesicular basalt	~ 60
ODP Leg 163, Hole 989B, 6R, 8W, 60 cm - 80 cm		Vesicular basalt	~ 60
ODP Leg 165, Hole 999B, 40R, 3W, 20 cm - 40 cm		Calcareous limestone with ash layers	~ 60
60ODP Leg 166, Hole 1005C, 34R, 2W, 115 cm - 135 cm		foraminiferous limestone	~ 60
ODP Leg 204, Hole 1244E, 2H, 2W, 8 cm - 28 cm		clay-rich sediment	~ 60
ODP Leg 209, Hole 1274A, 6R, 2W, 0 cm - 20 cm		peridotite	~ 60
ODP Leg 209, Hole 1275B, 19R, 4W, 0 cm - 20 cm		oxidized gabbro	~ 60
ODP Leg 210, Hole 1277A, 9R, 1W, 115 cm - 135 cm		serpentinized peridotite	~ 60
Meteor Leg 58/27, GeoB 8627-2, 3 m - 5 m		Clay-rich sediment	~ 60

4.2 Experimental procedures

Most of the drill cores had dried during storage. For NMR laboratory testing they were resaturated with distilled water. Samples had been dried to constant weight in an oven at a temperature of 60° C to remove all water from interconnected pores. Then they were saturated with distilled water in a vacuum exsiccator to constant weight.

Experimental parameters and measurement times of the NMR-MOUSE[®] and the Halbach core-scanners used for 1D T_2 measurements and for 2D T_1 - T_2 correlation experiments are shown in Table 3.

Table 3: Experimental parameters and measurement times of the different core-scanners.

Parameter	NMR-MOUSE [®]	Halbach core-scanner	Modified Halbach core-scanner
Frequency	21.1 MHz	12.7 MHz	9.6 MHz
Number of scans	600-1000	32-64	32-80
Pulse length	2.1 μ s - 2.6 μ s	9 μ s – 13 μ s	9.7 μ s
Inter-echo time	0.1 ms – 0.2 ms	0.06 ms – 0.2 ms	0.06 ms - 0.15 ms
Number of echoes	1300 - 2900	200 - 2900	1500-6400
Saturation delay time	-	-	1 s
Saturation recovery time	-	-	1 ms – 3.5 s
Measurement time	15 min - 30 min	Seconds – 5 minutes	1D measurements: 30 s - 5 min 2D measurements: 30 min

To estimate the limits of the NMR method with respect to the amount of paramagnetic impurities of the rocks magnetic susceptibility was measured on all drill cores with a Multi-Sensor Core Logger (MSCL) (Geotek, 2000). The MSCL uses a stepper motor to move core segments along a track and past a series of sensors. Positions and lengths are automatically detected. The logging measurements are controlled and rapidly collated by the system's computerized control.

All NMR porosities measured on hard rock were correlated to porosity values measured on corresponding core plugs with a helium gas pycnometer.

To extend the interpretation of NMR core data with respect to permeability, the following measurements were performed on corresponding core plugs: permeability, mercury

porosimetry and specific surface area. Additionally, electrical resistivity was measured to obtain the formation factor and thus tortuosity.

Permeability was determined from gas flow measurements. For low permeability rocks, the effective permeability to gas depends on pressure and may therefore deviate from that for water. Hence, the Klinkenberg correction method (Rieckmann, 1970) was used to account for this effect.

To estimate pore size distributions from NMR relaxation measurements, additional information was obtained by mercury porosimetry on selected core plugs. Mercury injection is a well established and widely used method for obtaining pore size information (Dullien, 1979). It yields the pore throat sizes weighted by the pore volumes to which the pore throats provide access (Coates et al., 1999). Mercury is injected into a core plug with stepwise increasing pressure until a maximum limit of 60,000 psi⁴ is attained. During each step, both the pressure and volume of mercury are measured after the pressure reaches equilibrium. Applying the Washburn equation (Webb, 2001), each pressure step can be associated with a particular pore throat size which decreases with pressure.

Precise measurements of the specific inner surface were performed by N₂-sorption according to the Brunauer-Emmet-Teller (BET) method (Brunauer et al., 1938). The specific surface is defined as the ratio between the absolute surface area of a solid and its mass (sample weight). The surface area includes all parts of accessible inner surfaces (mainly pore wall surfaces). The BET method involves the determination of the amount of the adsorptive gas required to cover the accessible internal pore surfaces of a solid with a complete monolayer of adsorbate. The volume of this monolayer adsorbate can be calculated from the adsorption isotherm by means of the BET equation (Bundesanstalt für Materialforschung und Prüfung, 2005).

The formation factor F was obtained from electrical resistivity measurements. The reciprocal of the formation factor describes the effective porosity with respect to transport processes such as fluid flow, electrical conductance, and diffusion (Pape et al., 2000). This quantity is defined by Archie's first law (Archie, 1942):

$$F = \frac{T}{\phi}, \quad (19)$$

⁴ 1 psi (pound per square inch) = 6980 Pa

where T is the tortuosity. Archie's law can also be written as a ratio of the bulk resistivity R_0 and the resistivity of the pore fluid R_w (Serra and Serra, 2004):

$$F = \frac{R_0}{R_w}. \quad (20)$$

5 Calibration to porosity

NMR transverse relaxation time measurements can be calibrated directly to porosity, which is a very important parameter in formation evaluation. Porosity determined on cores by mobile NMR instrumentation was compared with independent measurements of porosity. Moreover, accuracy, resolution, and limits of the method with regard to the magnetic susceptibility of the studied samples were analyzed.

Porosity is defined as the ratio of the void volume (the space between the grains) in a rock to its bulk volume (the overall volume of the voids plus the grains) (Schön, 1996; Hook, 2003):

$$\Phi = \frac{V_p}{V_b} = \frac{V_p}{V_p + V_g}, \quad (21)$$

where Φ is porosity, V_p is void space or pore volume, V_b is bulk volume, and V_g is grain volume.

Traditionally, the total NMR porosity seen in sandstone reservoirs is subdivided into three major components: free-fluid porosity with long T_2 components (T_2 values > 33 ms), capillary-bound water with T_2 times between 3 ms and 33 ms, and finally the fast decaying clay-bound water below 3 ms (Allen et al., 2000). However, the T_2 cutoffs for the different fluid components are variable and depend on the rock type and on the influence of magnetic field gradients. Figure 15 shows a T_2 distribution of a water-saturated sandstone sample measured with the Halbach core-scanner. The bimodal distribution of T_2 can be partitioned into capillary- and clay-bound water in small pores on the one hand and free, producible water in large pores on the other hand with fast and slow relaxation times, respectively.

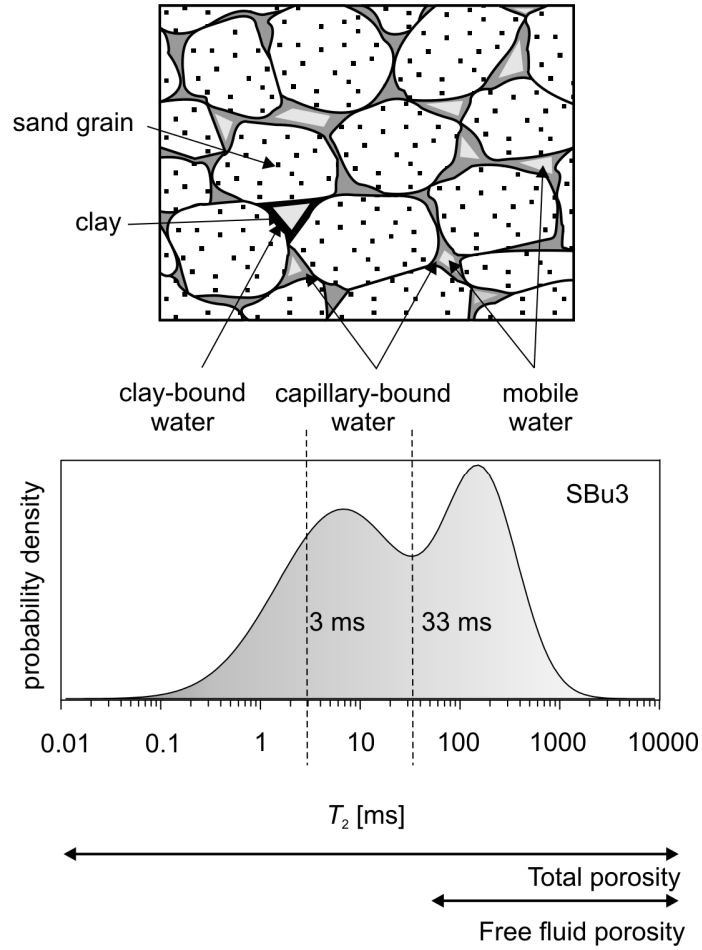


Figure 15: T_2 distribution measured with the modified version of the Halbach core-scanner on a water-saturated sandstone core plug (Ettlingen-SBu3) to identify fluid components. Mobile water (light gray) contributes to the longer T_2 time components, whereas capillary- and clay-bound water (dark gray) is reflected by shorter T_2 values. The cutoff time of 33 ms, commonly used in sandstone formations separates the T_2 distribution into the free fluid porosity and into the total porosity. The cutoff time of 3 ms separates clay- and capillary-bound water (after Allen et al., 2000).

5.1 NMR signal processing for porosity

In water-saturated cores the number of spins in the fluid within the sensitive volume of the sensor is proportional to sample porosity. The initial amplitude of the NMR signal S_p is the integral of the T_2 distribution, $P(T_2)$, where the distribution function P represents probability densities:

$$S_p = \int P d \log \left(\frac{T_2}{1 \text{ ms}} \right). \quad (22)$$

It is directly related to the number of the spins in the sensitive volume probed by NMR. Hence, porosity can be determined in two ways: (1) the initial CPMG signal amplitude measured on water-saturated cores is normalized to the amplitude measured on pure water which is equivalent to a porosity of 100 %. For improved accuracy, the full CPMG decay curve is reconstructed from the T_2 distribution and extrapolated to zero echo time; (2) the integrals of the distribution curves are normalized by the integral of the pure water signal. However, the porosity measured is a function of the shortest T_2 , the decay constant due to spin-spin relaxation that can be detected by the tool and this, in turn, depends on the echo spacing. Modern tools that can detect a T_2 as short as approximately 0.3 ms are thought to include most of the clay-bound water in their measurement yielding a porosity that compares reasonably well to values from helium core porosimetry (Allen et al, 2000). Older tools which can only detect T_2 times above approximately 3 ms are thought to measure an effective porosity (Hook, 2003). T_2 measurements on drill cores and plugs by mobile NMR instrumentation used in this study are performed at echo times of 0.2 ms and less. Hence, they yield total porosity including clay bound water which is comparable to values from helium core porosimetry.

In contrast, inside-out measurements with the NMR-MOUSE[®], which has a defined sensitive volume outside-in measurements with the Halbach core-scanners require a volume calibration for porosity determination. Special glass tubes (one semi cylindrical tube with a diameter of 60 mm and three fully cylindrical tubes with diameters of 20 mm, 50 mm and 60 mm imitating the geometry of the studied drill cores and plugs were produced. Thus NMR core measurements could be normalized with measurements on distilled water in the glass tubes, which correspond to 100 % porosity.

5.2 Porosity measurements

Several transverse relaxation measurements with the NMR-MOUSE[®] were performed on different drill cores of sandstone, limestone and basalt to obtain porosity. Figure 16 shows $T_{2,\text{eff}}$ distributions measured on sandstone cores recovered from the Allermoehe borehole. The shapes of the distributions curves for the different cores are similar, but the probability density clearly scales with the porosity of the samples.

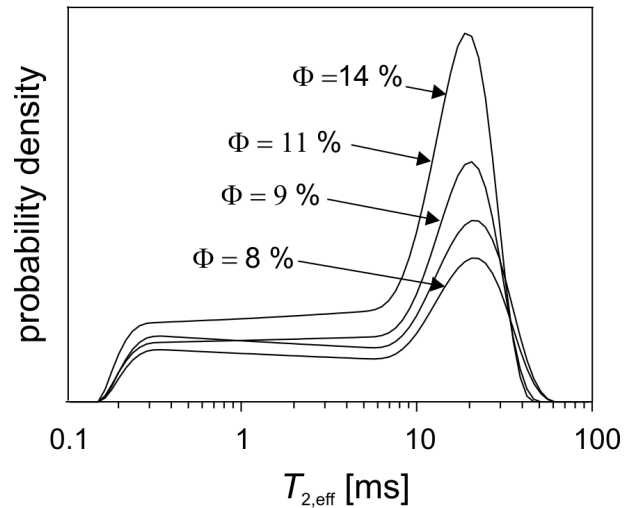


Figure 16: $T_{2,\text{eff}}$ distributions measured on sandstone cores of different porosity Φ recovered from the Allermöhe borehole in the Northern German sedimentary basin.

In Figure 17 porosity determined from measurements with the NMR-MOUSE[®] on various positions along drill cores is compared with conventional core porosity measured with a helium gas pycnometer on the corresponding core plugs. A linear regression yields a correlation coefficient $R^2 = 0.68$ and a standard deviation SD of 3.42 %. For samples with porosities below 5 % the signal-to-noise ratio of the measurement was insufficient for an inverse Laplace transformation, in contrast to samples with higher porosities.

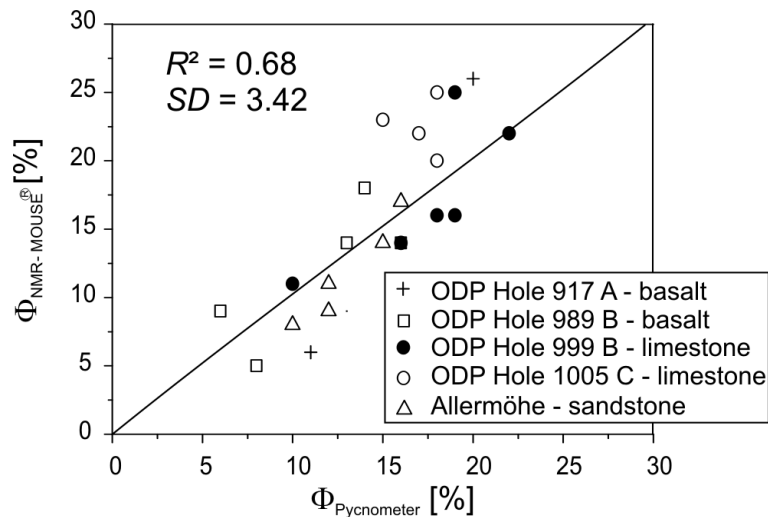


Figure 17: Correlation of porosities Φ determined on 22 rock samples with the NMR-MOUSE[®] ($\Phi_{\text{NMR-MOUSE}^{\text{®}}}$) and a gas pycnometer ($\Phi_{\text{pycnometer}}$); R^2 is the correlation coefficient and SD the standard deviation of the linear regression containing the point (0, 0).

Further measurements on drill cores of sandstone, limestone, shale and basalt were performed with the first version of the Halbach core-scanner (Figure 18).

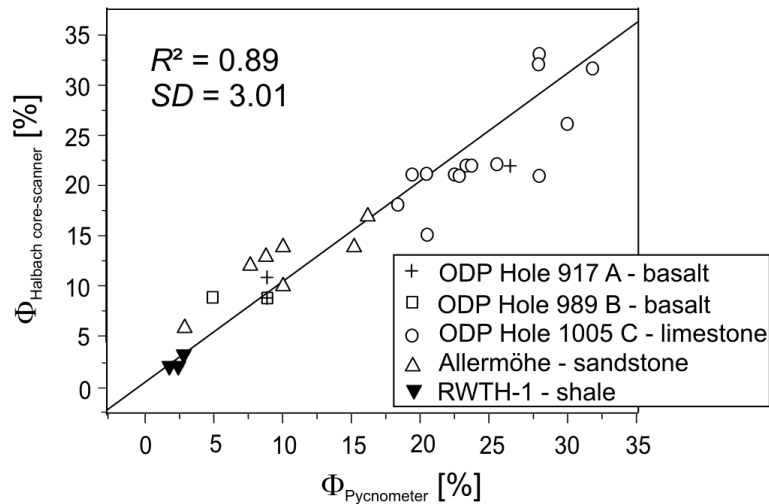


Figure 18: Correlation of porosities Φ determined on 29 rock samples with the Halbach core-scanner ($\Phi_{\text{Halbach core-scanner}}$) and a gas pycnometer ($\Phi_{\text{pycnometer}}$); R^2 is the correlation coefficient and SD the standard deviation of the linear regression containing point (0, 0).

Correlation with pycnometer porosity determined on the corresponding core plugs yields an improved linear regression with $R^2 = 0.89$ and a standard deviation SD of 3.01 %. Measurements on the shale cores recovered from the RWTH-1 borehole were performed right after recovery at the drilling platform. The Halbach core-scanner was used in combination with the cylindrical solenoidal coil (50 mm diameter). Relaxation time distributions of these cores are in the range of low T_2 values varying between 0.04 ms and 4 ms corresponding to the small pore sizes common in shale. Porosity values are in the range of 2 % and 6 %. For three shale cores porosity values determined with the Halbach core-scanner were compared to independently measured porosities with a helium gas pycnometer. The results are in excellent agreement as the measurements were performed on the cores in their original wet state (cf. Figure 18). Studies on the RWTH-1 shale cores with the Halbach core-scanner confirm that porosities of less than 3 % can be determined with accuracy.

NMR measurements using the NMR-MOUSE[®] and the Halbach core-scanner on basalt cores recovered during ODP Legs 152 and 163 showed a low signal-to-noise ratio due to high magnetic susceptibility values ($> 5 \times 10^{-3}$ SI) of the cores. The study of gabbro samples recovered during Leg 210 with magnetic susceptibility in excess of 30×10^{-3} SI illustrated the limit of the available mobile NMR instrumentation as no signals could be detected.

While NMR measurements with the NMR-MOUSE[®] and the first version of the Halbach core-scanner were performed on full cores, the reference porosities determined with a helium gas pycnometer were obtained from separate plugs taken from the same cores. Hence, these comparisons are influenced by the different volume affected by the measurements. In particular with regard to the limestone samples, the scatter of porosity in Figure 17 and Figure 18 to a large degree is due to heterogeneity in texture which is typically caused in carbonates by their intergranular pores and vugs (Toumelin et al., 2003).

Another source of scatter in measurements on ODP cores may be due to the slightly varying diameters of the cores. Deviations of up to 3 mm are common, but signal amplitudes were always normalized to the same volume of water.

The improved Halbach core-scanner was used to measure 30 sandstone core plugs recovered from the Allermöhe borehole and from several outcrops in Germany. The porosity results are compared with conventional porosity results determined with a helium gas pycnometer on the same core plugs. Hence, both porosity measurements are related to the same integration volume. This results in a high correlation coefficient $R^2 = 0.91$ between NMR core-scanner and pycnometer measurements and a low standard deviation SD of 2 % (Figure 19).

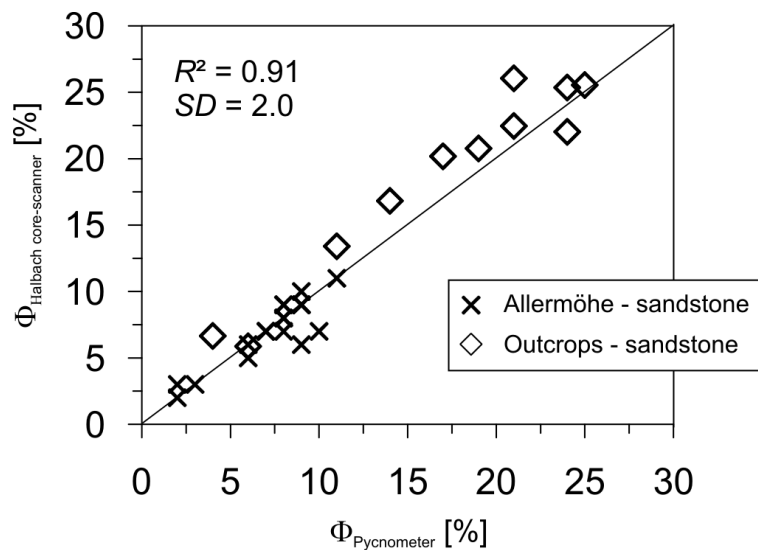


Figure 19: Correlation of porosities Φ determined on 30 sandstone core plugs with the modified version of the Halbach core-scanner ($\Phi_{\text{Halbach core-scanner}}$) and with a gas pycnometer ($\Phi_{\text{Pycnometer}}$). R^2 is the correlation coefficient and SD the standard deviation of the linear regression containing point (0, 0).

In the case of core samples recovered from the Allermöhe borehole, individual NMR core porosity values were additionally compared to the corresponding NMR logging data.

Both data sets are in good general agreement (Figure 20). The various sandstones of the Allermoehe aquifer were affected differently by mechanical compaction, cementation and dissolution of anhydrite during the history of diagenesis (Pape et al., 2005a). Based on the interpretation of downhole data which integrates over a much larger volume than the core samples, depth intervals for core sampling were chosen where low anhydrite cementation was assumed. However, thin section images from the two core samples recovered at around 3250 m show anhydrite minerals within the pore space which reduce the porosity. This explains the discrepancy between core and logging data. In contrast, systematic higher porosity values measured on core plugs from deeper parts of the borehole (below 3242 m) result from the purity of the sandstone samples.

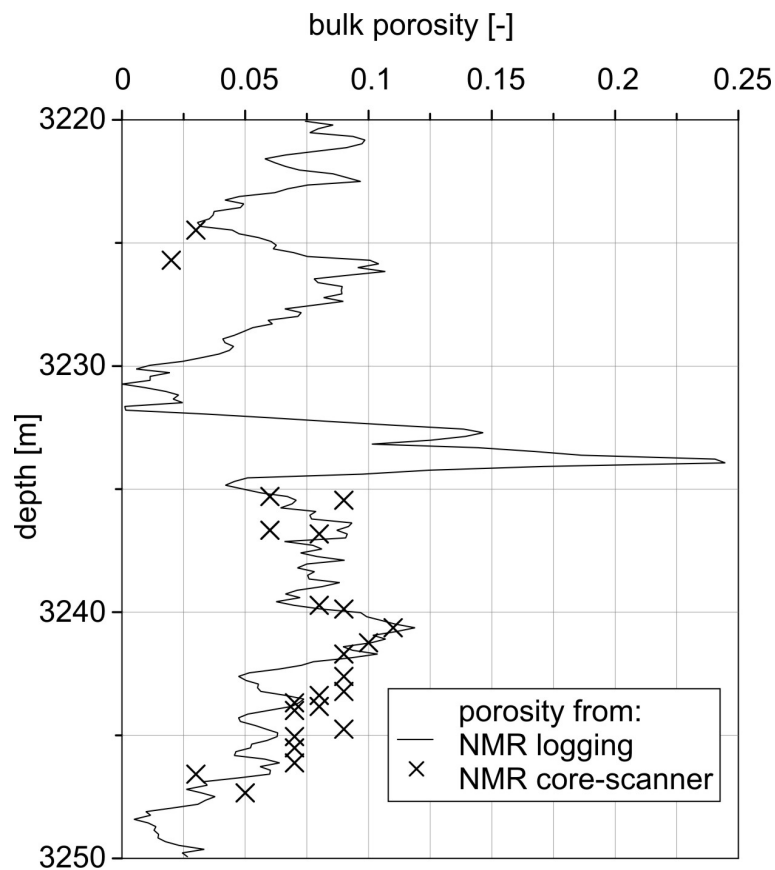


Figure 20: Comparison of NMR logging data recorded in the Allermoehe borehole and mobile NMR core-scanner results: the Schlumberger CMR porosity log correlates well with core plug porosities measured with the modified version of the Halbach core-scanner.

5.2 Appraisal of the results

In spite of the static magnetic field gradient, the NMR-MOUSE[®] can be used for porosity measurements of water-saturated drill cores. However, for samples with porosities

below 5 % the currently achievable signal-to-noise ratio of the NMR-MOUSE[®] is insufficient for a data processing based on an inverse Laplace transformation.

Because of the larger sensitive volume and the low static magnetic field gradient of the Halbach core-scanner associated with a higher signal-to-noise-ratio compared to the NMR-MOUSE[®] porosity can be determined with higher accuracy and to values as low as 2 %. Porosity determined from measurements with both the NMR-MOUSE[®] and the Halbach core-scanner correlate well with values determined independently on the same samples. For the Halbach core-scanner porosity measurements compare reasonably well with porosity from NMR logging data.

NMR measurements on samples with high magnetic susceptibility values are characterized by low signal-to-noise ratios. Cores with magnetic susceptibility values in excess of 30×10^{-3} SI are unsuitable for NMR analysis with the available mobile instrumentation.

NMR measurements on fresh drill cores directly at the drill platform yield porosity with the best accuracy because no drying and resaturation is required prior to measurements.

All porosity data, obtained by the different NMR core-scanners, are compiled in Tables A, B, and C in the Appendix with indication of the laboratory label and origin of the samples.

6 Estimation of pore size distributions and permeability

Low-field NMR can provide essential information on the size distribution of fluid-filled pore bodies in rock samples, because in the fast-diffusion limit the relaxation times are proportional to pore size (Kleinberg et al., 1994; Kenyon, 1997). Hence, NMR results can be used to predict permeability k . The permeability is the transport coefficient for flow through a porous medium in units of mD (1 mD = Millidarcy; darcy = 1 D = 9.87×10^{-13} m²). Compared to T_1 , T_2 measurements are preferred in NMR logging due to shorter measurement times and hence practical logging speed. However, measurements of T_2 are potentially affected not only by the properties of interest such as the pore size but also by the inhomogeneity of the static magnetic field and the internal magnetic field gradients (Kenyon, 1992) causing further reduction in relaxation times. Internal magnetic field gradients arise from magnetic susceptibility contrasts between rock mineral surfaces and the pore fluid (Godefroy et al., 1999 and Lonnes et al., 2003). The magnetic susceptibility value of water is negative (-9.26×10^{-6} SI at 20 °C) like for diamagnetic minerals such as rock salt, calcite, gypsum, quartz and graphite. In contrast, most minerals and rocks have positive values (Kleinberg and Horsfield, 1990). Compared to high-field NMR, measurements in low magnetic fields are favored for rock studies, because the internal field gradient is proportional to the applied magnetic field strength (Kleinberg et al., 1994). However, estimating permeability only from NMR T_2 relaxation time measured in a low and homogeneous static magnetic field is difficult, due to the unknown nature of each sample's surface relaxivity and its internal magnetic field gradients. Hence NMR data should be calibrated using additional information from core analysis.

1D transverse relaxation measurements on limestone cores recovered during ODP Leg 166, on sandstone core plugs from the Allermoehe borehole, and from different German outcrops were used to estimate permeability by a standard method common in the oil industry.

Transport properties of the Allermoehe sandstone formation were studied separately (Pape et al, manuscript in preparation). Aside from 1D T_2 relaxation measurements, additional 2D T_1 - T_2 correlation experiments were performed on corresponding core plugs for more accurate permeability estimation. Moreover, further structural parameters were determined such as porosity, formation factor, specific inner surface area, pore radius distributions from

mercury injection, and permeability from gas flow measurements. Using a new model, based on the dependence between the surface relaxivity ρ_2 and the pore radius, permeabilities of the Allermoehe samples can be determined accurately. In contrast, the standard calculation scheme from the oil industry fails due to the increasing influence of internal magnetic field gradients on the T_2 distributions with decreasing pore radii.

6.1 Influence of external magnetic field gradients

Transverse relaxation time (T_2) distributions of a water-saturated limestone sample (ODP Leg 166, 21R, 2W, 128-149 cm) with low magnetic susceptibility (Table 1) measured with both the first version of the Halbach core-scanner and the NMR-MOUSE[®] at the same echo time of 0.1 ms show the effect of the external field gradients on transverse relaxation (Figure 21). Compared to the measurement with the NMR-MOUSE[®], the relaxation time distribution determined with the Halbach core-scanner is broader with slower T_2 times. Due to the diffusive attenuation of the signal measured in the presence of the external field gradient of the NMR-MOUSE[®], CPMG decays are truncated for long echo times, and all distributions of $T_{2,\text{eff}}$ are compressed towards shorter relaxation times.

To study the influence of diffusion due to the low external gradient of the B_0 field of the first version of the Halbach core-scanner, transverse relaxation time distributions were measured with different echo times of 0.08 ms, 0.1 ms and 0.15 ms on a further limestone core (ODP Leg 166, 1005C, 19R, 1W, 55-64 cm) (Table 1) yielding low magnetic susceptibility values. CPMG echo envelopes corresponding to different echo times are overlapping. None is shortened by diffusive attenuation (Figure 22).

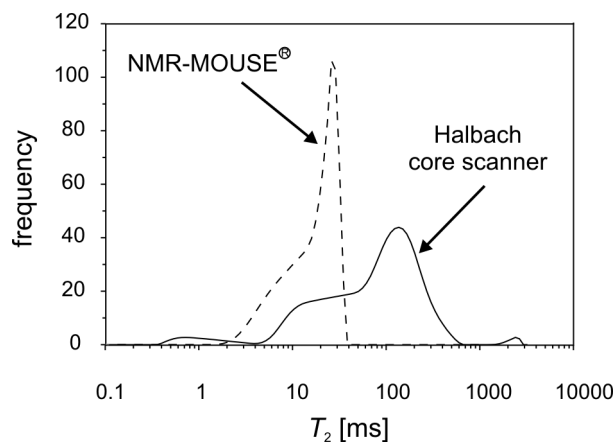


Figure 21: The relaxation time distribution obtained by inverse Laplace transformation for the limestone sample (ODP Leg 166, Hole 1005C, 21 R, 2W, 128 cm - 149 cm) is wider for large T_2 values when measured with the Halbach core-scanner than when measured with the NMR-MOUSE[®].

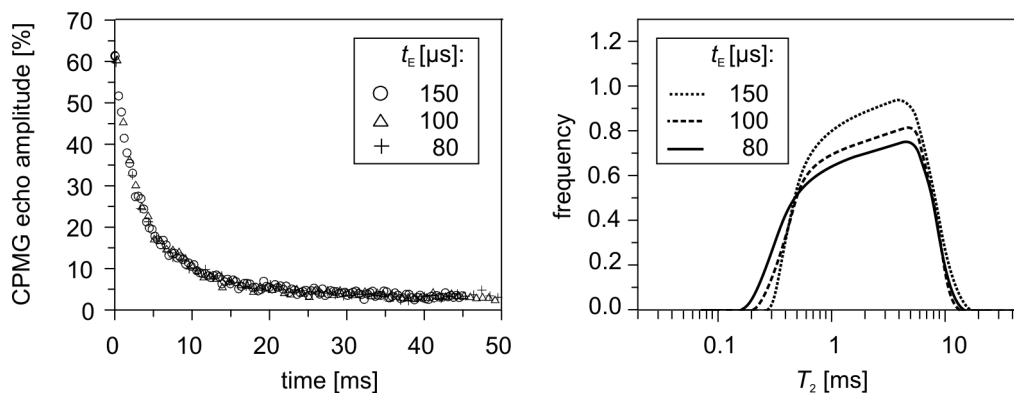


Figure 22: CPMG echo envelopes of a water-saturated limestone (ODP Leg 166, 1005C, 19R, 1W, 55 cm - 64 cm) measured at different echo times t_E with the Halbach core-scanner (left); T_2 distributions of the limestone sample (right).

Recording NMR signals from samples that contain clay-bound water is difficult because the very fast decays associated with small pores vanish during the echo spacing. Further reduction in relaxation times occurs due to the fact that internal field gradients increase with decreasing pore radii (cf. chapter 6.6). The shortest echo spacing is limited by transient processes in the transmitter-receiver system, and the pulse length.

Clay-rich samples recovered from Meteor Leg 58/27 were studied with the NMR-MOUSE[®] using the shortest possible echo time of 0.1 ms. The sediments had been preserved and could be measured in their original wet state. Due to the higher static magnetic field and its stronger gradient compared to that of the Halbach core-scanner all decays measured with the NMR-MOUSE[®] are shortened by diffusion. Hence, the clay-bound water that corresponds to the smallest pore sizes could not be resolved as the decays occurred too early for detection. Besides, due to the small sensitive volume of the NMR-MOUSE[®] only a small portion of the clay-bound water could be integrated by the measurement. Hence, the signal intensity was very low. The detected signals from the clay-rich sediment samples could not be separated from signals which were detected due to background signals from the printed circuit board and transient oscillations (Figure 23a).

In contrast, T_2 distribution curves recorded by the Halbach core-scanner are less influenced by diffusion processes due to the lower static magnetic field of the sensor and its gradient. The Halbach core-scanner was used to measure T_2 distributions on clay-rich sediment cores recovered during ODP Leg 204, where NMR logging was performed for the first time in ODP. Average T_2 -values recorded by Schlumberger's *ProVision* Logging-While-Drilling (LWD) tool range between 3 ms and 3 s (Shipboard Scientific Party, 2003).

T_2 distribution curves were recorded by the Halbach core-scanner on cores acquired from adjacent holes during ODP Leg 204. Due to the large sensitive volume of the Halbach core-scanner the signal intensity was high and because of the lower influence of diffusion and the short echo time of 0.06 ms, T_2 values could be detected down to 0.1 ms (Figure 23b).

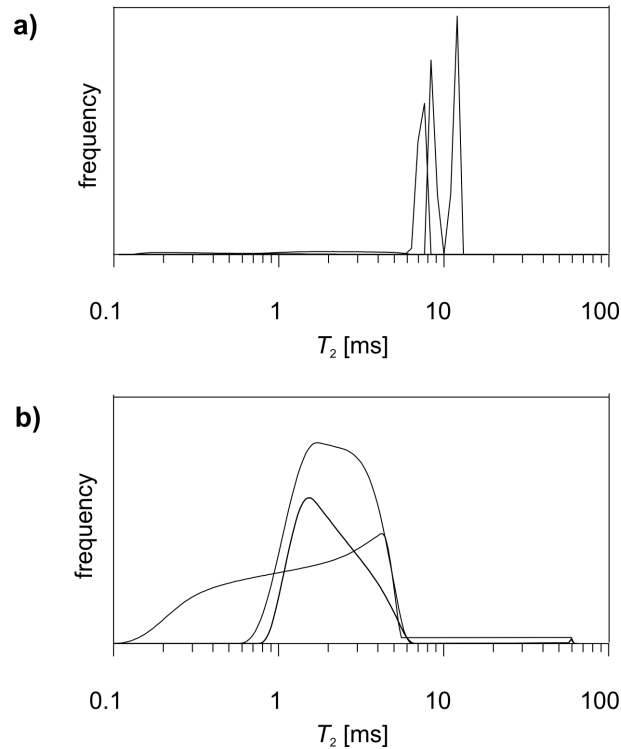


Figure 23: T_2 distribution measurements on clay-rich sediment cores: (a) cores recovered during Meteor Leg 58/27 GeoB 8627-2 measured with the NMR-MOUSE[®]. Short decays are lost because of the high magnetic field gradient of the instrument; (b) cores recovered during ODP Leg 204 in Hole 1245C measured with the Halbach core-scanner; the T_2 values range from 0.1 ms - 7 ms.

6.2 Limits due to magnetic susceptibility

For high magnetic susceptibility rocks of more than 5×10^{-3} SI, such as basalt and peridotite, cores recovered during ODP Legs 152, 163, 209, and 210 (Table 1), a direct estimate of the pore-size distribution from relaxation measurements is not possible. This is due to the strong influence of diffusion caused by the large internal magnetic field gradients within the porous medium. CPMG measurements by the Halbach core-scanner show very pronounced diffusion effects and distribution curves are compressed to shorter T_2 values or even cannot be detected at all. An example for measurements on two peridotite cores recovered during ODP Legs 209 and 210 is shown in Figure 24.

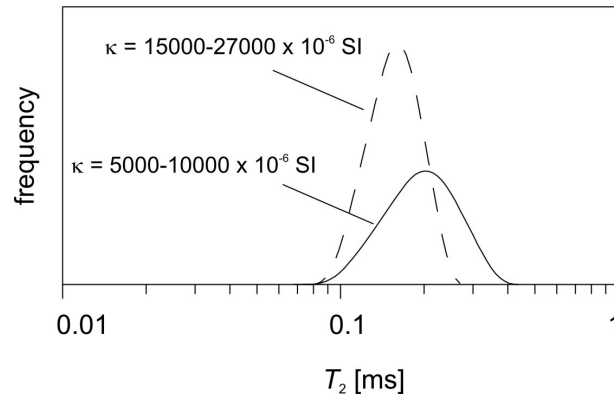


Figure 24: T_2 distributions measured with the first version of the Halbach core-scanner on two peridotite cores (full line: ODP Leg 209, 1274A, 6R, 2W, 0 cm -30 cm (dashed line: ODP Leg 210, 1277A, 9R, 115 cm - 145 cm) with high magnetic susceptibility values. The T_2 distribution curves are compressed to short T_2 values.

6.3 Standard NMR models for permeability prediction

The two widely applied permeability transforms, based on NMR measurements, are the Timur-Coates equation (23) based on the work of Timur (1969) and the $T_{2,LM}$ equation (24) developed by Kenyon et al. (1988):

$$k_{TIM} = \left[\left(\frac{\Phi}{10} \right)^2 \left(\frac{FFV}{BFV} \right) \right]^2. \quad (23)$$

$$k_{T_{2,LM}} = a T_{2,LM}^2 \Phi^4, \quad (24)$$

In these equations, k is permeability in mD, FFV and BFV are the NMR-derived fractional volumes of free and bound fluid, $T_{2,LM}$ is the logarithmic mean T_2 value in ms, whereas a is an empirically determined constant which depends on the surface relaxivity. Usually, for sandstones $a = 4 \text{ mD}/(\text{ms})^2$ (Morris et al., 1994), whereas in carbonates, smaller factors have been used, for example $a = 0.1$ (Kenyon and Kolleeny, 1995). Both equations are empirical, and permeability prediction by NMR always requires a local calibration to core data in each formation. The Timur-Coates equation can be customized for oil reservoirs where it is widely used for interpretation of NMR logging data. In contrast, the $T_{2,LM}$ equation fails for hydrocarbon-bearing formations but works well in zones containing only water (Coates et al., 1999). The rationalization for such correlation comes from the following: The Kozeny-Carman relationship (Kozeny, 1927 and Carman, 1956) (compare chapter 6.4) proposes that

the permeability is inversely proportional to the square of the surface to volume ratio S/V of the pore space. This suggests that permeability is proportional to the square of a representative NMR relaxation time ($T_{2,LM}$) through equation (8) (compare chapter 2.3). The logarithmic mean $T_{2,LM}$ of the relaxation time is defined as:

$$T_{2,LM} = 10^{\left[\frac{\sum_{i=1}^N V_i \log\left(\frac{T_{2i}}{1\text{ms}}\right)}{\sum_{i=1}^N V_i} \right]}, \quad (25)$$

where V_i is the volume fraction of a pore i decaying with the relaxation time T_2 . Usually, N is ~ 100 . The volumes of capillary and bound water in equation (23) are obtained by centrifuging in the laboratory (Kenyon, 1997). Threshold values for T_1 and T_2 of 46 ms and 33 ms have been established as reasonable for sandstones (Straley et al., 1997). Longer times varying between 90 ms to 150 ms have been found for carbonates (Dunn et al., 2002; Chang et al., 1994; Kenyon and Kolleeny, 1995). Nevertheless, both models are not universal for realistic structure variations, textures and mineral composition (Mirotnik et al., 2004). The cutoff method is also subject to the same concerns about changes in surface relaxivity and in pore throat/pore-body ratio as is permeability estimation from $T_{2,LM}$ (Kenyon, 1997). Both permeability models generate an appreciable amount of data scatter relative to the independently determined permeabilities.

In the present study, the $T_{2,LM}$ equation (24) was used for NMR measurements on different rock types with variable porosity and permeability, such as limestone cores recovered during ODP Leg 166, sandstone cores recovered from the Allermoehe borehole, and samples from different German outcrops. T_2 distributions were measured with the first version of the Halbach core-scanner at ten different positions along three limestone cores from different depth intervals of ODP Hole 1005C (ODP Leg 166) characterized by low magnetic susceptibility (Table 1). Porosity of the limestone sections vary from 20 % to 32 %. Permeability values from gas flow measurements fall in a narrow range between 0.6 mD and 3.9 mD. The $T_{2,LM}$ equation was used to calculate permeability (k_{NMR}). For the calibration of a , gas permeability (k_{gas}) was measured on ten corresponding core plugs. A good match between k_{NMR} and k_{gas} was found when $a = 0.2$ (Table 4).

Additionally eight sandstone core plugs sampled at different outcrops in Germany were studied with the modified Halbach core-scanner. Porosities range from 17 % to 26 %

and permeabilities from gas flow measurements vary between less than 0.049 mD up to 2205 mD. The $T_{2,LM}$ equation was applied using the factor $a = 4$ common for sandstone formations to predict permeability. The results agree well with those from gas flow measurements ($R^2 = 0.81$ and $SD = 0.6$) (Figure 25).

Table 4: Permeability determined with different methods at various positions along three limestone cores (ODP Leg 166, Hole 1005C: 21R, 1W, 128 cm – 149 cm; 34 R, 1W, 48 cm- 80 cm; 34 R, 2W, 108 cm - 141 cm): k_{gas} (gas permeability), k_{NMR} (equation (24) using a value for a of 0.2).

ODP sample identification	k_{gas} [mD]	k_{NMR} [mD]
166, 1005C, 21 R, 1W, 137 cm	2.3	3.7
166, 1005C, 21 R, 1W, 141 cm	1.8	2.5
166, 1005C, 34 R, 1W, 51 cm	3.9	2.3
166, 1005C, 34 R, 1W, 55 cm	1.6	1.1
166, 1005C, 34 R, 1W, 61 cm	1.9	1.6
166, 1005C, 34 R, 1W, 68 cm	2.0	1.1
166, 1005C, 34 R, 1W, 72 cm	1.9	1.5
166, 1005C, 34 R, 1W, 76 cm	2.2	1.6
166, 1005C, 34 R, 2W, 132 cm	0.6	0.1
166, 1005C, 34 R, 2W, 134 cm	0.8	0.1

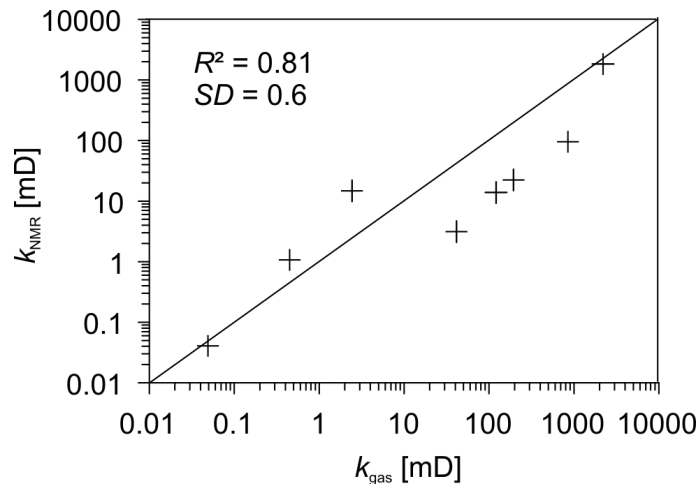


Figure 25: Correlation of permeabilities k determined on eight sandstone core plugs recovered from different outcrops in Germany. The values k_{NMR} were calculated according to equation (24) from T_2 distribution measurements performed with the modified version of the Halbach core-scanner using the factor of $a = 4$. The values k_{gas} result from gas flow measurements; R^2 is the correlation coefficient and SD the standard deviation.

Moreover, permeabilities from the Schlumberger CMR-log[®] recorded in the Allermoehe borehole were calculated according to Pape et al (1999) from the free water fraction Φ_{free} (T_2 cutoff = 33 ms) using the factor of $a = 4$ in equation (24). The permeability log is plotted in Figure 26.

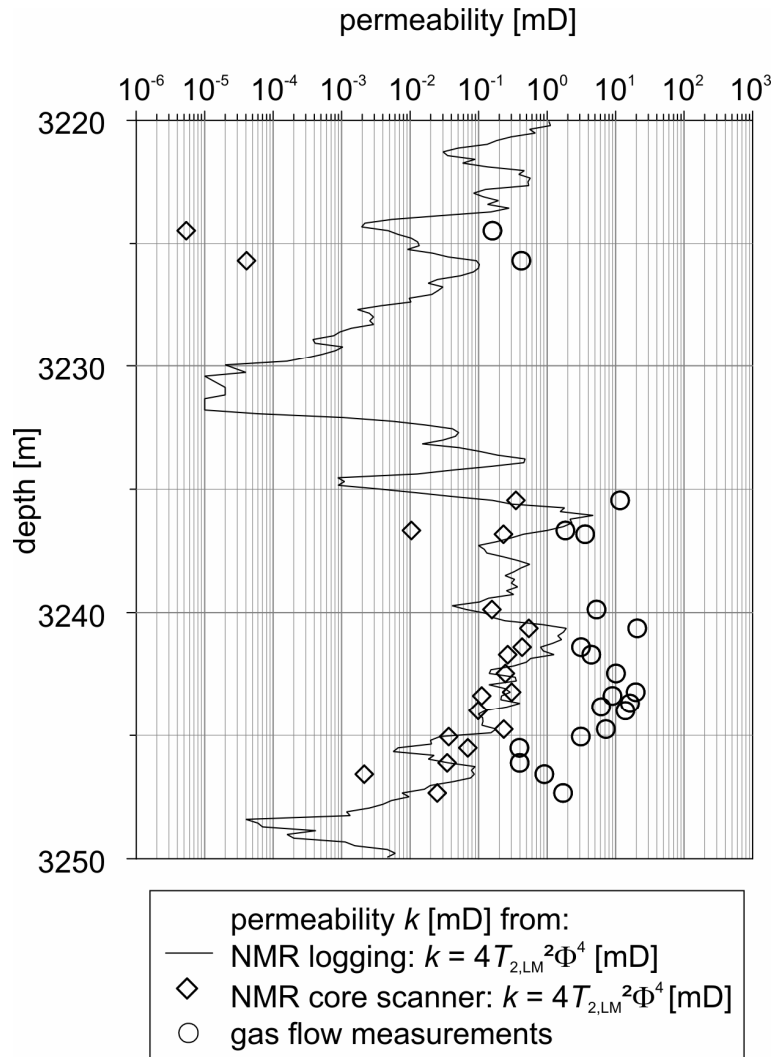


Figure 26: Comparison of NMR logging and mobile NMR core-scanner data: the CMR permeability is compared to NMR core permeability based on equation (24). Permeability values derived from gas flow measurements on core plugs are shown for comparison.

For comparison, the permeabilities calculated from equation (24) for laboratory 1D T_2 measurements and gas permeabilities are shown. Deviations between NMR and gas permeabilities are large. This can be explained by the low porosity values of the Allermoehe samples varying between 2 % and 11 %. Due to the high exponent of porosity equal to 4 in the $T_{2,LM}$ equation (24) which is suitable for formations with high porosity, permeability

calculated from Allermoehe logging and core data is underestimated. Therefore, in the following more detailed studies on the low porosity Allermoehe sandstone formation are shown to predict permeability more accurately. For an overview a set of petrophysical parameters measured on the Allermoehe core plugs is given in Table 5.

Table 5: Petrophysical parameters measured on the Allermoehe core plugs from various depths: pycnometer porosity Φ_{pyc} , formation factor F , specific inner surface area $S_{\text{por,BET}}$ measured with the BET method, gas permeability k_{gas} , logarithmic mean values from 1D T_2 distributions $T_{2,\text{LM}_1\text{D}}$ and from 2D T_1 and T_2 distributions $T_{1,2\text{LM}}$.

Sample	Depth [m]	Φ_{pyc} [%]	F	$S_{\text{por,BET}}$ [μm^{-1}]	k_{gas} [mD]	$T_{2,\text{LM}_1\text{D}}$ [ms]	$T_{1,\text{LM}_2\text{D}}$ [ms]	$T_{2,\text{LM}_2\text{D}}$ [ms]
AC1	3224.45	2	53	40.42	0.16	2.95	-	-
AC3	3225.64	2	54	39.79	0.42	7.95	-	-
AC4	3235.34	9	56	2.38	11.6	82.17	510	81.84
AC6	3236.67	6	72	10.59	1.85	14.23	250	30.11
AC7	3236.79	8	67	9.40	3.59	32.93	220	29.07
AC9	3239.88	8	70	8.45	5.26	24.37	300	37.04
AC10	3240.69	11	38	5.24	20.7	30.37	330	41.34
AC12	3241.44	9	68	10.89	3.13	32.78	330	28.17
AC13	3241.75	9	58	9.21	4.42	31.79	190	24.34
AC14	3242.56	9	44	5.63	10.1	30.60	320	35.76
AC15	3243.16	9	50	4.34	19.6	34.02	440	35.03
AC16	3243.42	8	55	6.60	8.99	26.01	330	33.29
AC18	3243.78	8	56	10.89	6.16	21.95	320	33.73
AC19	3243.92	10	47	6.50	13.9	32.01	370	39.90
AC20	3244.79	8	60	5.17	7.2	29.77	320	35.35
AC21	3245.10	7	79	6.71	3.1	19.49	-	-
AC22	3245.54	7	89	9.34	0.39	17.47	150	7.68
AC23	3246.15	8	92	8.37	0.4	18.88	130	7.47
AC24	3246.65	3	65	38.67	0.91	25.65	-	-
AC25	3247.31	6	66	12.52	1.71	21.57	240	23.89

6.4 General permeability relationships

According to the Kozeny-Carman equation (Kozeny, 1927; Carman, 1956), permeability is related to porosity Φ , tortuosity T and the effective hydraulic pore radius r_{eff} :

$$k = \left(\frac{1}{8}\right) \left(\frac{\Phi}{T}\right) r_{\text{eff}}^2 \quad (k \text{ in } \mu\text{m}^2; r_{\text{eff}} \text{ in } \mu\text{m}). \quad (26)$$

The term (Φ/T) can be replaced by the inverse formation factor F^{-1} , and by Φ^m/A , according to the first Archie equation (Archie, 1942) with the cementation or tortuosity factor m , which varies between 1 and 3 and the coefficient A , which ranges from 0.6 to 2 according to the rock texture. The effective pore radius can be substituted by S_{por} , the specific surface normalized by the pore volume. For cylindrical hydraulically connected pores r_{eff} is related to S_{por} by:

$$r_{\text{eff}} = \frac{2}{S_{\text{por,hydr}}}. \quad (27)$$

In equation (27), the effective pore radius is calculated as twice the ratio of the model capillary's volume and its surface. This equation assumes that the pores are bundles of smooth, cylindrical but tortuous capillaries of radius r_{eff} (Figure 27) (Pape et al., 2000).

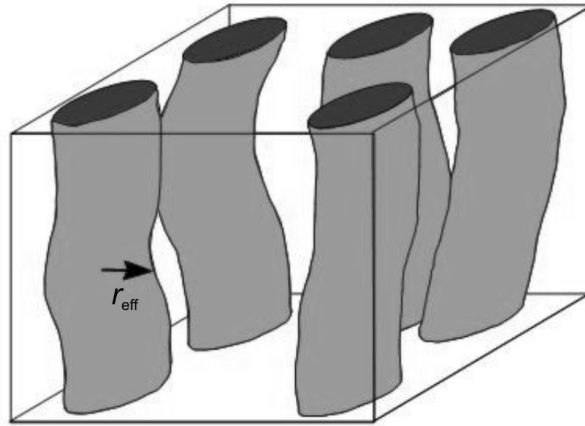


Figure 27: Simple model for porous media with smooth capillaries of radius r_{eff} .

In contrast, the most simple model for NMR relaxation which relates relaxation times T_1 and T_2 to S_{por} , was developed for isolated spherical pores (Kleinberg et al., 1994) yielding:

$$\frac{1}{T_{1,2}} = \rho_{1,2} S_{\text{por,NMR}}, \quad (28)$$

where $\rho_{1,2}$ is the surface relaxivity given in $\mu\text{m/s}$ and

$$r_{\text{eff}} = \frac{3}{S_{\text{por,NMR}}} . \quad (29)$$

Similar to equation (27), equation (29) follows for a model porous medium made up of smooth spherical pores (Figure 28).

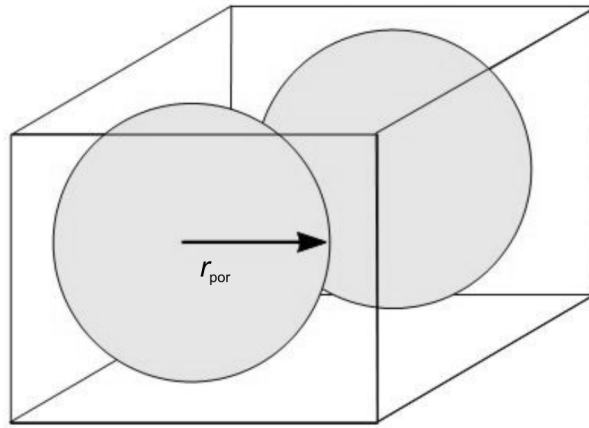


Figure 28: Simple model for porous media with smooth spheres of radius r_{por} .

Based on a fractal model for porous rocks (Figure 29), several geometrical relations were established (Pape et al. 1999; Pape et al., 2000) in which specific surface, pore radius, tortuosity, and porosity are connected through the fractal dimension D . This is the fundamental geometric parameter for the description of the pore-space structure. A standard value for sandstones is $D = 2.36$ (Pape et al., 1987). The principal idea of the fractal concept is the dependence of the measure of geometrical parameters such as the area of a rough surface on the power of resolution of the measuring method. As a result, $S_{\text{por,BET}}$ measured by nitrogen adsorption is larger than $S_{\text{por,hydr}}$ because the size of nitrogen atoms is smaller than the size of water molecules. According to Pape et al. (1987), this is described by

$$S_{\text{por,hydr}} = 0.1410 S_{\text{por,BET}} r_{\text{eff}}^{-0.36} . \quad (30)$$

Then equations (27) and (30) yield:

$$r_{\text{eff}} = \left(\frac{2}{0.141 S_{\text{por,BET}}} \right)^{\frac{1}{0.64}}. \quad (31)$$

From equations (31) and (26) follows:

$$k_{S_{\text{por,BET}}} = 497 \left(\frac{\Phi}{T} \right) S_{\text{por,BET}}^{-3.125}$$

$$\left(k_{S_{\text{por,BET}}} \text{ in } \mu\text{m}^2, S_{\text{por,BET}} \text{ in } \mu\text{m}^{-1} \right). \quad (32)$$

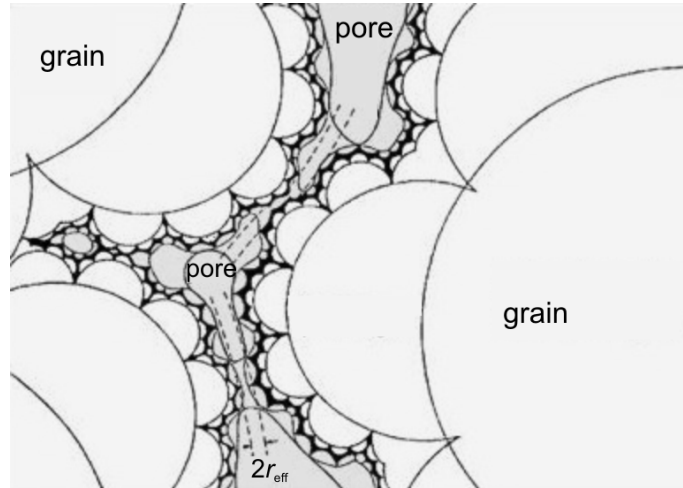


Figure 29: Cartoon showing a rock according to the fractal pore space model (Pape et al., 1987) composed of geometrical pores and hydraulic capillaries with effective radius r_{eff} .

Permeabilities of the Allermoehe core plugs were calculated with equation (32) using measured values of F and $S_{\text{por,BET}}$ and electrical tortuosities calculated from the measured values of F (Table 6). Except for one outlier they agree within one order of magnitude with the measured gas permeabilities (Figure 30).

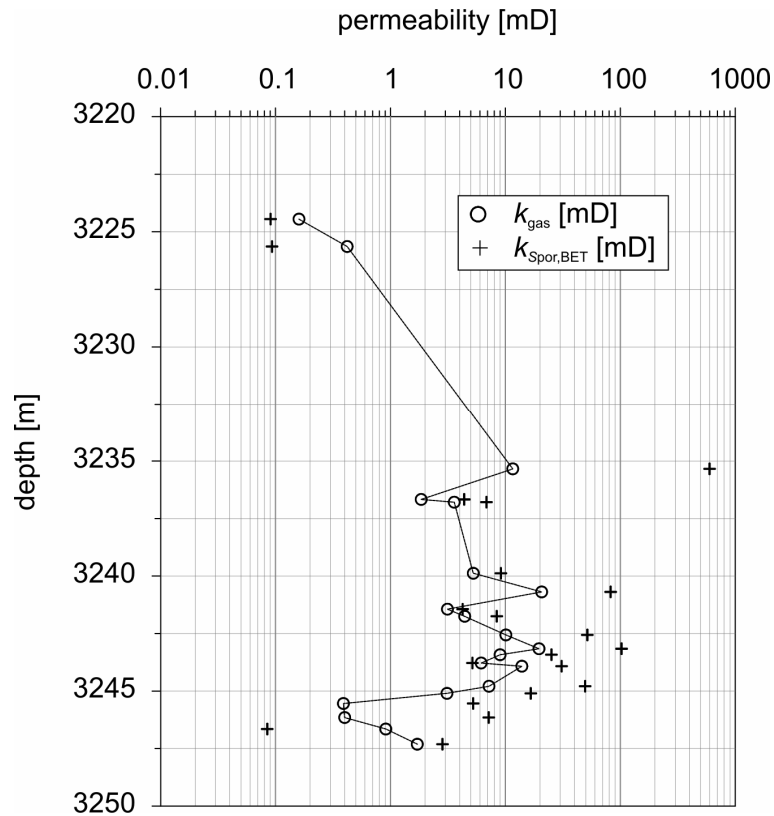


Figure 30: Calculated and measured permeabilities ($k_{\text{Spor,BET}}$ and k_{gas}) versus depth of the borehole Allermoeh.

From the calculated and the measured permeabilities effective hydraulic pore radii were derived with equation (26). By comparison with the logarithmic mean values of the radius distributions from mercury intrusion, $r_{\text{eff,LM}}$, the r_{eff} values calculated from F and k_{gas} or $k_{\text{Spor,BET}}$ are too low (Table 6). This may be due to the fact, that the influence of the clay fraction which can be obtained from mercury injection curves measured on the Allermoeh samples (cf. chapter 6.5) was neglected. Besides the electric tortuosity T_{el} was used instead of the hydraulic tortuosity T_{hydr} which may be considerably larger (Pape et al., 2005a). Numerical simulations on two-dimensional networks by David (1993) showed that the so-called ‘network tortuosity’ for hydraulic flow was 1.5 times larger than the ‘network tortuosity’ for electrical current. Interpretation of PFG-NMR measurements on Allermoeh sandstone (Pape et al., 2005b) revealed that the radius of pore bodies of about 12 μm exceeds that the radius of pore throats measures of about 2 μm . Tortuosity values for self-diffusion of water reached values ranging from 5 to 20.

Table 6: Petrophysical parameters of Allermoehe samples: Tortuosity from electrical measurements (T_{el}) and calculated according to Archie's equation (T_{hydr}); permeability from gas flow measurements (k_{gas}) and derived from T_{el} and $S_{por,BET}$ (k_{Spor}); effective pore radii: r_{eff} calculated from k_{gas} and k_{Spor} and $r_{eff,LM}$ from mercury injection curves.

Sample	T_{el}	T_{hydr} $= 0.6\Phi^{1.2}$	k_{gas} [mD]	$k_{Spor,BET}$ [mD] eq. (32)	r_{eff} [μm] from k_{gas} eq. (26)	r_{eff} [μm] from $k_{Spor,BET}$ eq. (26)	$r_{eff,LM}$ [μm] from mercury intrusion
AC1	1.06	65.60	0.16	0.09	0.26	0.19	-
AC3	1.08	65.60	0.42	0.09	0.42	0.20	-
AC4	5.04	10.79	11.6	598.38	2.26	16.27	-
AC6	4.32	17.55	1.85	4.38	1.02	1.58	-
AC7	5.36	12.43	3.59	6.84	1.37	1.90	3.14
AC9	5.6	12.43	5.26	9.13	1.70	2.25	3.78
AC10	3.8	8.48	20.7	82.35	2.37	4.74	5.27
AC12	6.12	10.79	3.13	4.25	1.29	1.51	2.76
AC13	5.22	10.79	4.42	8.42	1.42	1.96	2.82
AC14	3.96	10.79	10.1	51.66	1.87	4.24	4.90
AC15	4.5	10.79	19.6	102.53	2.77	6.36	9.23
AC16	4.4	12.43	8.99	25.15	1.97	3.31	4.45
AC18	4.48	12.43	6.16	5.16	1.64	1.51	4.63
AC19	4.7	9.51	13.9	30.87	2.26	3.38	-
AC20	4.8	12.43	7.2	49.45	1.84	4.84	4.87
AC21	5.53	14.59	3.1	16.63	1.39	3.22	-
AC22	6.23	14.59	0.39	5.25	0.52	1.92	-
AC23	7.36	12.43	0.4	7.16	0.54	2.28	0.29
AC24	1.95	40.33	0.91	0.08	0.68	0.21	-
AC25	3.96	17.55	1.71	2.83	0.94	1.22	-

Based on fractal theory (Pape et al., 1999) a power-law relationship can be established between permeability and porosity. A fit to average sandstones yields:

$$k_{\phi} = 31\Phi + 7463\Phi^2 + 191(10\Phi)^{10} \quad (k \text{ in } \text{nm}^2). \quad (33)$$

From data of Allermoehe sandstone Pape et al. (1999) derived the relationship:

$$k_{\phi} = 0.309(100\Phi)^{4.85} \quad (k \text{ in } \text{nm}^2) \quad (34)$$

which was used to obtain permeability from NMR logging and NMR core-scanner data. The permeability values from NMR data according to equation (34) and from gas flow measurements agree well with the exception of a few outliers (Figure 31).

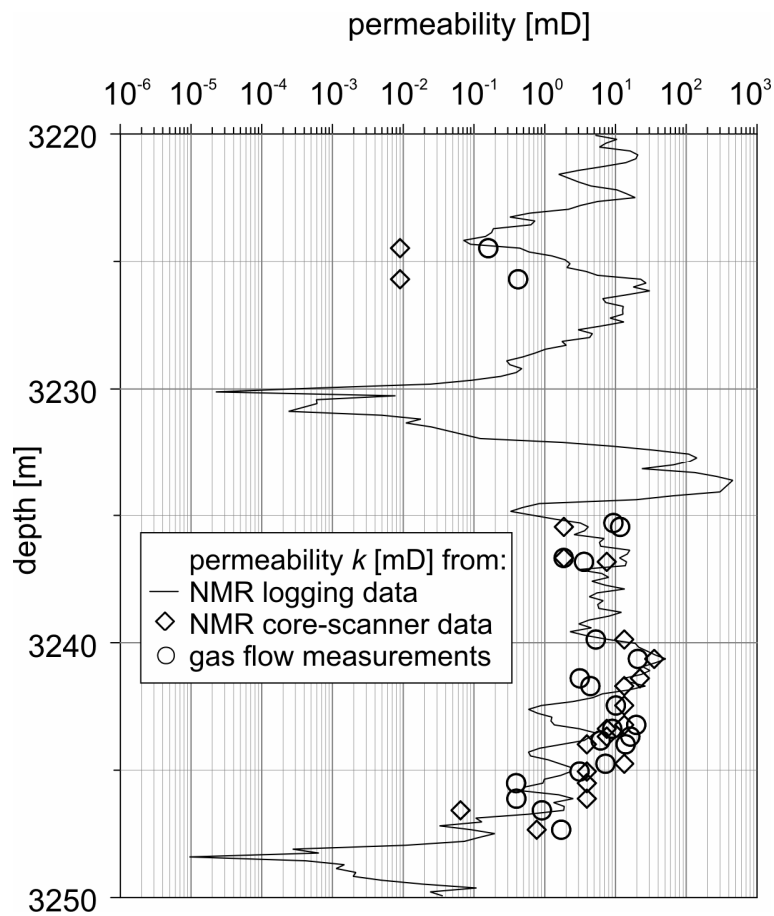


Figure 31: Correlation of core plug permeabilities: results from gas flow measurements are compared to calculated permeabilities from a power-law relationship between permeability and porosity according to equation (36). Porosity data from NMR logging and NMR core-scanner measurements were used.

However, to develop a method for permeability prediction which is suitable for different formations, information on effective pore radius derived i.e. from mercury porosimetry should be used.

6.5 Mercury injection curves

The curves of mercury injection porosimetry were used firstly to obtain an estimate of the effective hydraulic pore radius and secondly to determine the factor $3\rho_{1,2}$ which relates pore radius r to $T_{1,2}$ of the NMR relaxation curves according to equations (28) and (29):

$$T_{1,2} = \frac{1}{3\rho_{1,2}} \underbrace{\left(\frac{3}{S_{\text{por,NMR}}} \right)}_{r_{\text{eff, cf. eq. (29)}}} = c_{r,T_{1,2}} r, \quad (35)$$

where $c_{r,T_{1,2}}$ is the conversion factor in $\text{ms } \mu\text{m}^{-1}$.

The logarithmic mean value of the pore radius distribution is given by $r_{\text{eff,LM}}$:

$$r_{\text{eff,LM}} = 10 \left[\frac{\sum_{i=1}^{N=154} \Delta V_i \log\left(\frac{r_i}{1\mu\text{m}}\right)}{V_{\text{rel}}} \right], \quad (36)$$

where ΔV_i are the differential volumes of the pore radius distribution curve and V_{rel} is the integral volume equal to one.

For clay bearing rocks containing small pores which contribute not to the hydraulic conductivity equation (26) has to be modified to:

$$k = \left(\frac{1}{8} \right) \left(\frac{\Phi - \Phi_{\text{clay}}}{T_{\text{hydr}}} \right) r_{\text{eff,LM}}^2$$

$$(k \text{ in } \mu\text{m}^2; r_{\text{eff,LM}} \text{ in } \mu\text{m}), \quad (37)$$

where $T_{\text{hydr}} = 0.6\Phi^{-1.2}$ (David, 1993, cf. Table 6). Figure 32 shows the mercury injection curves recorded on core plugs AC9 and AC23. The differential volumes ΔV_i of the distribution curves are plotted as relative volumes, with the integral volume V_{rel} equal to one. The limits r_{border} between the clay volume portion and the hydraulically relevant volume portion are set where the steeper slope of the distribution curve characteristic for small radii changes into a shallower one. For sample AC23 with a considerable high clay content, the effective pore radius is calculated by truncating the clay portion at $r_{\text{border}} = 0.05 \mu\text{m}$ and stopping the summation in equation (36) at that point. In this case, the term $r_{\text{eff,LM}}$ in equation (37) is substituted by $r_{\text{eff,free,LM}}$. To calculate permeability of several Allermoehe samples from the effective pore radii, good results were obtained by using $(\Phi - \Phi_{\text{clay}}) = 0.7 \Phi$ in the

corresponding permeability equation (37). The results are presented in Table 7. Figure 33 shows calculated and measured permeabilities plotted versus depth.

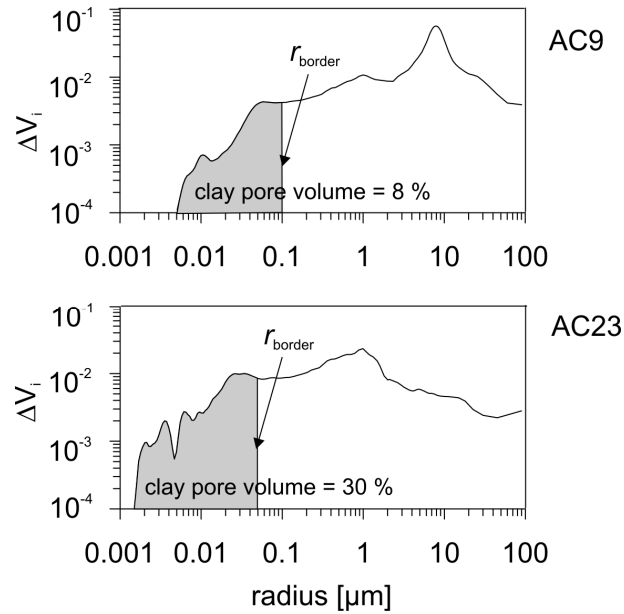


Figure 32: Pore radius distribution curves of core plugs AC9 and AC23. The differential volumes ΔV_i of the distributions curves are plotted as relative volumes, with the integral volume V_{rel} equal to one. The limits of the clay region r_{border} are set where the steeper slope of the distribution curve characteristic for small radii changes into a shallower one.

Table 7: Pore radii $r_{eff,LM}$ and $r_{eff,LM,free}$ resulting from mercury injection curves and corresponding permeability values calculated according to equation (37). For comparison gas permeabilities (k_{gas}) are added.

Sample	$r_{eff,LM}$ [μm]	$r_{eff,LM,free}$ [μm]	k [mD] from $r_{eff,LM}$ [μm] eq. (37)	k [mD] from $r_{eff,LM,free}$ [μm] eq. (37)	k_{gas} [mD]
AC7	3.14	-	5.6	-	3.6
AC9	3.78	-	8.2	-	5.3
AC10	5.27	-	32	-	20.7
AC12	2.76	-	5.7	-	3.1
AC13	2.82	-	5.9	-	4.4
AC14	4.90	-	17.7	-	10.1
AC15	9.23	-	63	-	19.6
AC16	4.45	-	11.3	-	9
AC18	4.63	-	12.2	-	6.2
AC20	4.87	-	13.5	-	7.2
AC23	0.29	0.9	-	0.46	0.4

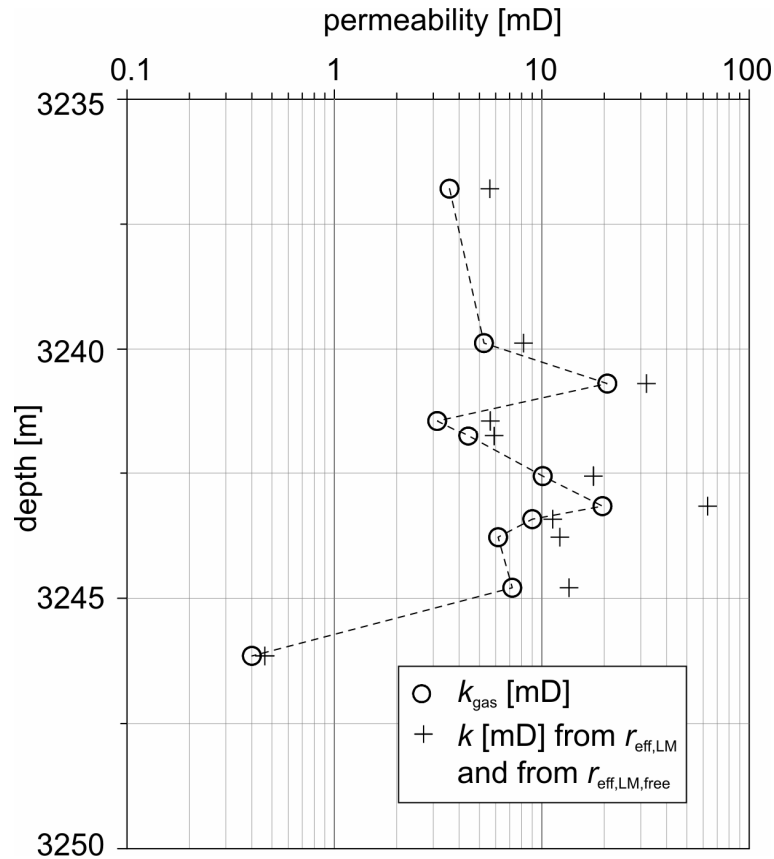


Figure 33: Permeabilities of Allermoehe sandstone samples calculated from pore radius distributions according to equation (37) and plotted versus depth and compared to gas permeabilities.

6.6 Surface relaxation and ‘internal field gradient relaxation’

Among experimental methods, such as gas BET and mercury intrusion, NMR has been used successfully to measure the S/V ratio via spin relaxation (Kenyon, 1992) and to study pore structure of sedimentary rocks using pulsed field gradient (PFG) techniques (Timur, 1969; Hürlimann et al., 1994). A further concept without applying field gradients was demonstrated by Song (2000), Kenyon et al. (2002) and Song (2003) to measure the pore size length scale using internal magnetic field gradients. The nuclear spin magnetization decay due to diffusion in the internal field (DDif) is measured and thus the pore length scale can be deduced.

In this study pore radii are determined from T_2 distributions measured in a nearly homogeneous static magnetic field. Therefore an individual ρ_2 is related to each T_2 value of the T_2 distribution curve. As equation (35) indicates a linear relationship between NMR-relaxation times and pore radii, the $T_{1,2}$ distribution curves can be processed in a similar way as the mercury injection curves by calculating the logarithmic mean values $T_{1,2,LM}$. In the case

of longitudinal relaxation, the linearity is really sufficiently fulfilled. This means that the relaxivity ρ_1 is constant with respect to pore radius although ρ_1 may vary for different samples. The physical process related to ρ_1 is called surface relaxation. It acts directly at the mineral surface of the pore walls where the magnetization of the hydrogen atoms is lost. For the same sample, the T_2 distribution curves are shifted to smaller values. This indicates that a second relaxation process is active, which is explained by dephasing of the transverse magnetization vectors caused by diffusion of water molecules within an internal, inhomogeneous magnetic field. These strong field gradients are caused by paramagnetic centers at the pore walls and are effective within a certain distance from the paramagnetic minerals. For simplification this will be represented by a thickness d of this field gradient interlayer (Figure 34).

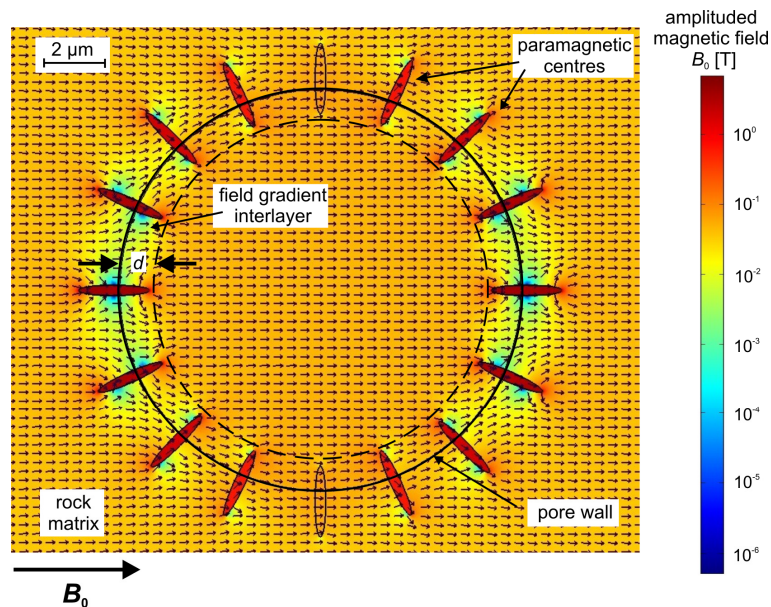


Figure 34: Schematic model of a pore, which is posed to a constant, homogeneous static magnetic field of amplitude $B_0 = 0.2$ T. Strong local magnetic field gradients caused by paramagnetic centers at the pore wall affect a layer of thickness d .

In this situation transverse relaxation can be described by (Pape et al., manuscript in preparation):

$$\frac{1}{T_2} = \frac{1}{T_1} + \frac{1}{T_{2,ifg}}, \quad (38)$$

where surface relaxation due to interaction of proton spins with the pore wall lattice is assumed to be the same for T_1 and T_2 . $T_{2,\text{ifg}}$ is the internal field gradient relaxation time with corresponding ‘internal field gradient relaxation’ $\rho_{2,\text{ifg}}$:

$$T_{2,\text{ifg}} = \frac{1}{\rho_{2,\text{ifg}}} \left(\frac{r-d}{3} \right). \quad (39)$$

Combining equations (35) and (39) we obtain:

$$\rho_2 = \rho_1 + \frac{\rho_{2,\text{ifg}}}{\left(1 - \frac{d}{r}\right)}; \quad (40)$$

$$\frac{T_1}{T_2} = 1 + \frac{\rho_{2,\text{ifg}}}{\rho_1 \left(1 - \frac{d}{r}\right)}. \quad (41)$$

Equations (40) and (41) show that ρ_2 and T_1/T_2 decrease with pore radius r . As the external field in the improved Halbach core-scanner used for NMR relaxation measurements is very homogeneous, this instrument provides favorable conditions for separating surface relaxivity and field gradient relaxivity based on data from the two-dimensional (2D) T_1 - T_2 correlation experiment.

6.7 2D T_1 - T_2 correlation experiments

To study the influence of diffusion on the shape of the T_2 distribution function for low porosity rocks, such as those from the Rhaetian sandstone at Allermoeche, 2D T_1 - T_2 relaxation correlation experiments were performed with the improved Halbach core-scanner. Previous results are published in Anferova et al. (in press). The T_1/T_2 ratio, determined from 2D T_1 - T_2 correlation experiments performed on the Allermoeche samples is not constant even at short echo spacing. It decreases with pore size from values of 10 to 4. Figure 35 shows the 2D T_1 - T_2 map measured on the Allermoeche core plug AC15.

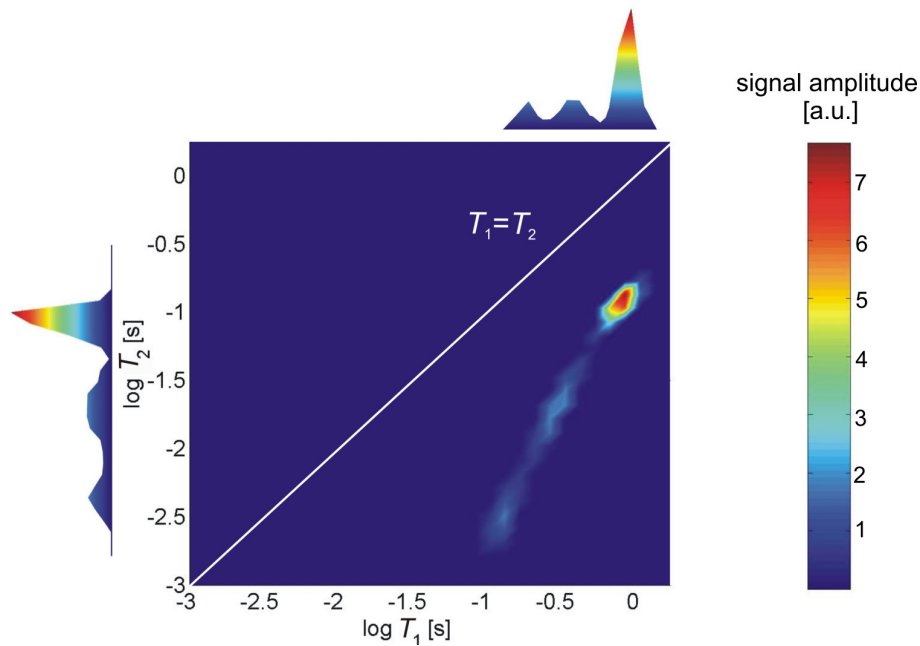


Figure 35: Two dimensional T_1 - T_2 map recorded on Allermoehe core plug AC15. Due to high internal gradients, the T_1/T_2 ratio is not constant.

The T_1 - T_2 correlation experiments were used to determine the relationship between ρ_1 and ρ_2 . In analogy to the mercury injection curves, the differential magnetizations Δm of each $T_{1,2}$ fraction of the distribution curves are plotted as relative volumes, with the integral volume m_{rel} equal to one. First, all relaxation curves with related mercury injection curves were correlated to the radius distribution curves by shifting the relative volume distribution relative to the pore size distribution until the maxima of both curves for large radii and large $T_{1,2}$ values coincide. Then ρ_1 and $\rho_{2,\text{eff}}$ are determined from equation (35) for each sample (Table 8). As an example, Figure 36 shows the comparison of T_1 and T_2 distributions with the pore radius distribution measured by mercury intrusion on sample AC9.

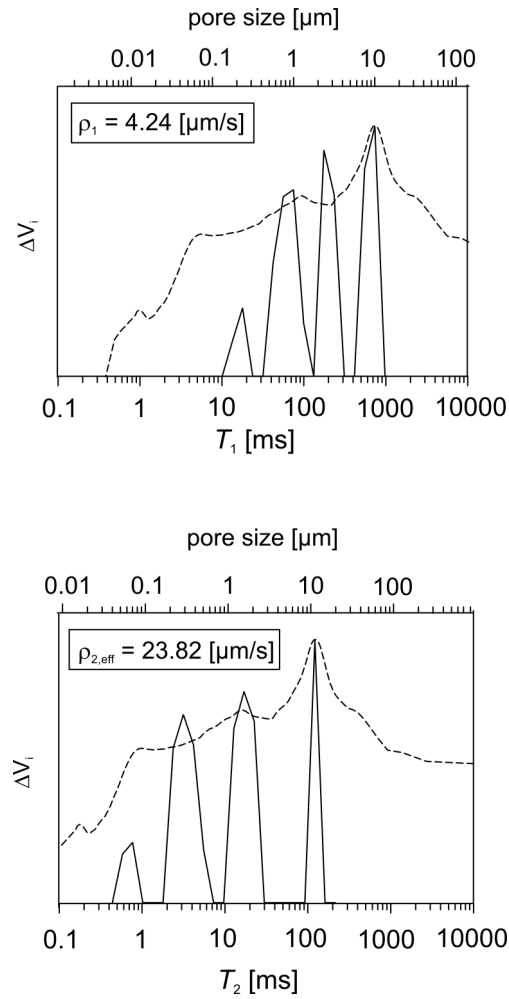


Figure 36: Distributions of pore radius (dashed lines) and $T_{1,2}$ (full lines) measured on Allermoehe sample AC9. Surface relaxivities ρ_1 and $\rho_{2,\text{eff}}$ were varied until the first maxima for large $T_{1,2}$ values match the maximum of the pore radius distribution obtained from mercury injection.

Table 8: Values of surface relaxivities ρ_1 and $\rho_{2,\text{eff}}$ found by the comparison of mercury injection and 2D $T_{1,2}$ distribution curves according to equation (35).

sample	ρ_1 [$\mu\text{m/s}$]	$\rho_{2,\text{eff}}$ [$\mu\text{m/s}$]
AC7	4.83	21.89
AC9	4.24	23.82
AC10	4.24	23.82
AC12	2.37	17.76
AC13	4.21	13.30
AC14	5.31	37.20
AC15	4.28	35.10
AC16	5.77	33.62
AC18	5.09	29.68
AC23	2.22	12.96
mean value	4.256	24.915

As core plug AC9 is representative for all Allermoehe samples studied in this work due to its petrophysical properties (porosity, range of pore sizes, and permeability) it will also be used to demonstrate the pore radius dependence of ρ_2 and to calculate the thickness of the interlayer d :

For large $T_{1,2}$ values, the first maxima of the relative volume distribution occur at $T_1 = 749.9$ ms and $T_2 = 133.4$ ms. The second maxima for the next largest $T_{1,2}$ values occur at $T_1 = 177.8$ ms and $T_2 = 17.78$ ms (Figure 36). Correlating the T_1 curve with the radius distribution curve at the first maximum yields a conversion factor of $c_{r,T1} = 78.64$ ms μm^{-1} (cf. equation (35)). Consequently, the first maximum corresponds to $r_1 = 9.53$ μm and the second maximum corresponds to $r_2 = 2.26$ μm . Inserting the appropriate T_1 and T_2 values corresponding to both maxima in equation (41) and dividing the two equations yields:

$$\frac{\left(\frac{T_1(r_1)}{T_2(r_1)} - 1\right)}{\left(\frac{T_1(r_2)}{T_2(r_2)} - 1\right)} = h = \frac{\left(1 - \frac{d}{r_2}\right)}{\left(1 - \frac{d}{r_1}\right)}. \quad (42)$$

From this one obtains: $h(1 - d/r_1) = (1 - d/r_2)$ or $h(r_2/r_1)(r_1 - d) = (r_2 - d)$, yielding the thickness of the interlayer:

$$d = r_2 \frac{(1-h)}{1-h\left(\frac{r_2}{r_1}\right)}. \quad (43)$$

Inserting the values of the parameters on the right-hand side of equation (43) yields $d = 1.25$ μm . The surface relaxivities of AC9 obtained from the comparison of the $T_{1,2}$ distribution curves with the mercury injection curve are $\rho_1 = 4.24$ $\mu\text{m/s}$ and $\rho_{2,\text{eff}}(r_1) = 23.82$ $\mu\text{m/s}$. This yields the ‘field gradient interlayer relaxivity’ $\rho_{2,\text{ifg}} = (\rho_{2,\text{eff}}(r_1) - \rho_1)(1 - d/r_1) = 17.01$ $\mu\text{m/s}$.

In order to study the relationship between the pore radius r , surface relaxivity ρ_2 , and transverse relaxation time T_2 , equations (40) and (35) were used to calculate ρ_2 and T_2 in a table of values. From this table and equation (40) one sees that ρ_2 as a function of T_2 has a pole at $r = d$. The ρ_2 values calculated with equation (40) are valid as long as the pore radius

r is about three times larger than d which corresponds to $T_2 = 40$ ms. To calculate correct ρ_2 values for T_2 times shorter than 40 ms, the ρ_2 curve which has been calculated for large pore radii can be extrapolated by a straight line in the plot of $\log \rho_2$ versus $\log T_2$ with the slope at $r = (3 d)$. From data measured on Allermoehe sample AC9, the slope of -0.3 was obtained which gives:

$$\rho_2(r_i) = \rho_2(r_j) \left(\frac{T_2(r_i)}{T_2(r_j)} \right)^{-0.3}, \quad (44)$$

where i and j are adjacent pore radii.

In a more simple fashion, a correction is determined empirically. From the first distribution maxima for large values of T_2 and the pore radius, $\rho_{2,\text{eff}}$ is determined from equation (35). At this point, $\rho_{2,\text{eff}}$ is equal to ρ_2 . For shorter T_2 times, ρ_2 values become larger than $\rho_{2,\text{eff}}$ and consequently calculated pore radii $r_{\rho_{2,\text{eff}}}$ are too small. Hence, they have to be multiplied by a correction term which was calibrated for the sample AC9. The correction term found as $(9.53 \mu\text{m} / r_{\rho_{2,\text{eff}}})^{0.3}$ yields one for $r = 9.53 \mu\text{m}$ corresponding to the first maximum for large T_2 values. Then the corrected pore radius $r_{\text{corr}}(T_{2,\text{LM}})$ related to $T_{2,\text{LM}}$ is determined with the following equation:

$$r_{\text{corr}}(T_{2,\text{LM}}) = r_{\rho_{2,\text{eff}}}(T_{2,\text{LM}}) \left(\frac{9.53 \mu\text{m}}{r_{\rho_{2,\text{eff}}}(T_{2,\text{LM}})} \right)^{0.3}, \quad (45)$$

where $r_{\rho_{2,\text{eff}}}(T_{2,\text{LM}})$ is determined with equation (35) from $T_{2,\text{LM}}$ and $\rho_{2,\text{eff}}$. Using the exponent of 0.3 yields a corrected pore radius $r_{\text{corr}}(T_{2,\text{LM}})$ which is similar to the pore radius $r_{\rho_1}(T_{1,\text{LM}})$. The pore radius $r_{\rho_1}(T_{1,\text{LM}})$ is obtained with equation (35) and ρ_1 from the T_1 distribution curve which is measured simultaneously on sample AC9.

In Figure 37a, the shape of the T_1 and T_2 distribution curves of sample AC9 are compared. The relaxation curves are correlated by shifting the relative volume distributions until the maxima of both curves for large $T_{1,2}$ values coincide. This is achieved by multiplying the T_2 values by the term $(\rho_{2,\text{eff}} / \rho_1)$. In a next step the T_2 distribution curve is renormalized in two ways. Firstly it is corrected with the approach based on the thickness of the field gradient interlayer. Therefore each measured T_2 value of the T_2 distribution curve is

multiplied with the term (ρ_2 / ρ_1) . The individual ρ_2 values are determined with equations (40) and (44). Secondly, the T_2 distribution curve was renormalized empirically. Therefore, T_2 values were multiplied with the correction term $(9.53 \mu\text{m} / r_{\rho_2,\text{eff}})^{0.3}$ and with the term $(\rho_{2,\text{eff}} / \rho_1)$. In both cases a nearly perfect match with the T_1 curve has been achieved (Figure 37b).

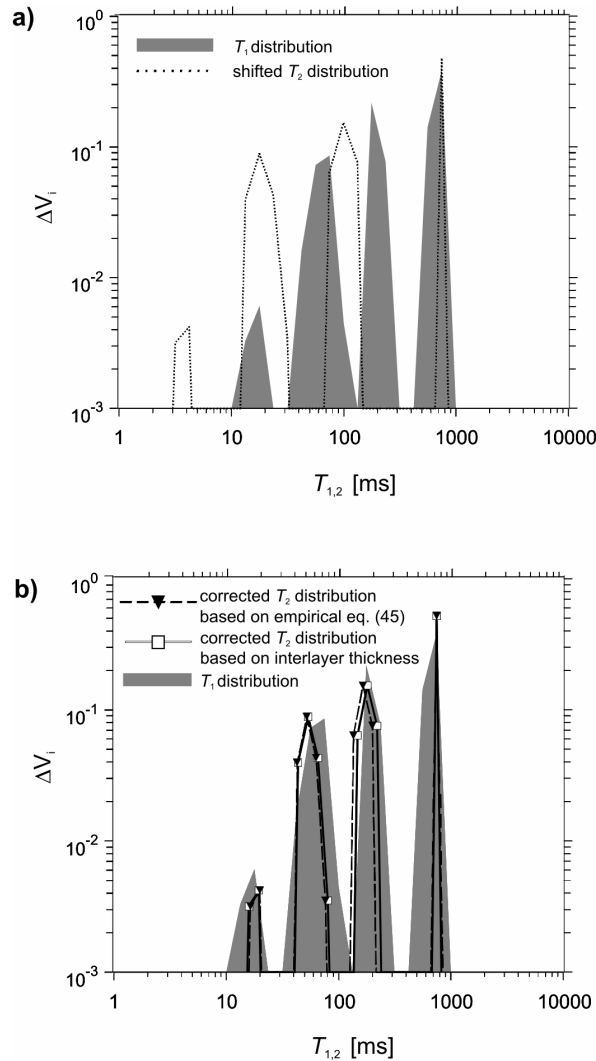


Figure 37: Relationships between T_1 and T_2 distribution curves of the T_1 - T_2 correlation experiment, explained for sample AC9; (a) the T_2 distribution curve is shifted so that the first maxima for large $T_{1,2}$ values of both distribution curves coincide; (b) Two correction procedures applied for the T_2 distribution curve are demonstrated which compensate the effect of enhanced relaxation due to magnetic field gradients in the layer next to pore walls.

For all samples for which a pore radius distribution curve was available, values of $r_{\rho_1}(T_{1,\text{LM}})$ and $r_{\rho_2,\text{eff}}(T_{2,\text{LM}})$ were calculated from the T_1 and T_2 distribution curves. Mean values of ρ_1 and $\rho_{2,\text{eff}}$ (Table 8) of these samples were used to determine values of $r_{\rho_1}(T_{1,\text{LM}})$

and $r_{\rho 2, \text{eff}}(T_{2, \text{LM}})$ for the rest of samples. From the $r_{\rho 2, \text{eff}}(T_{2, \text{LM}})$ values also $r_{\text{corr}}(T_{2, \text{LM}})$ values were calculated according to equation (45). Permeability was then predicted with the following equations:

$$k = \left(\frac{1}{8} \right) \frac{c \Phi}{T_{\text{hydr}}} r_{\rho_1}^2(T_{1, \text{LM}}) \quad (46)$$

and

$$k = \left(\frac{1}{8} \right) \frac{c \Phi}{T_{\text{hydr}}} r_{\text{corr}}^2(T_{2, \text{LM}}) \quad (47)$$

$(k \text{ in } \mu\text{m}^2; r_{\rho_1}(T_{1, \text{LM}}) \text{ and } r_{\text{corr}}(T_{2, \text{LM}}) \text{ in } \mu\text{m}),$

with tortuosity $T_{\text{hydr}} = 0.6 \Phi^{-1.2}$ (David, 1993, cf. Table 6). The factor $c = 0.7$ was chosen due to the considerably high clay-content of the Allermoeche samples resulting in a value of $\Phi - \Phi_{\text{clay}} = 0.7$ in eq. (37) (cf. chapter 6.5). Table 9 shows the resulting pore radii and permeabilities.

Table 9: Results based on mercury injection curves and 2D T_1 - T_2 correlation experiments performed on the Allermoeche samples: pore radii $r_{\rho_1}(T_{1, \text{LM}})$ and $r_{\rho 2, \text{eff}}(T_{2, \text{LM}})$ are calculated according to equation (35) using surface relaxivities ρ_1 and $\rho_{2, \text{eff}}$ shown in Table 8; the $r_{\text{corr}}(T_{2, \text{LM}})$ values are calculated according to the empirical equation (45). Permeabilities k follow from equations (46) and (47). For comparison gas permeabilities (k_{gas}) are added.

sample	$r_{\rho_1}(T_{1, \text{LM}})$ [μm] eq. (35)	$r_{\rho 2, \text{eff}}(T_{2, \text{LM}})$ [μm] eq. (35)	$r_{\text{corr}}(T_{2, \text{LM}})$ [μm] eq. (45)	k [mD] from $r_{\rho_1}(T_{1, \text{LM}})$ eq. (46)	k [mD] from $r_{\text{corr}}(T_{2, \text{LM}})$ eq. (47)	k_{gas} [mD]
AC4	6.51	6.12	6.97	35.96	27.67	11.6
AC6	3.19	2.25	3.45	3.60	1.53	1.85
AC7	3.19	1.91	3.07	5.38	2.08	3.59
AC9	3.82	2.65	3.87	8.53	4.00	5.26
AC10	4.20	2.95	4.18	20.06	10.03	20.7
AC12	2.35	1.50	2.59	4.97	1.67	3.13
AC13	2.40	0.97	1.91	2.69	0.70	4.42
AC14	5.10	3.99	5.16	19.71	11.78	10.1
AC15	5.65	3.69	4.88	17.64	10.06	19.6
AC16	5.71	3.36	4.57	11.92	6.43	8.99
AC18	4.89	3.00	4.23	10.19	5.15	6.16
AC19	4.72	2.98	4.21	16.48	8.29	13.9
AC22	1.92	0.57	1.32	0.74	0.14	0.39
AC23	0.87	0.29	0.82	0.38	0.05	0.4
AC25	3.06	1.79	2.93	2.60	0.97	1.71

In Figure 38, the permeabilities calculated from 2D T_1 and T_2 distributions according to equations (46) and (47), are plotted versus depth and compared to gas permeabilities. Additionally, Figure 39 compares calculated permeability according to the standard method in oil industry (equation (24)) from 2D T_2 distributions using a factor of $a = 4$ which is generally accepted for sandstones. Whereas permeabilities derived from equation (47) agree well with gas flow measurements, results from the standard method used in oil industry based on equation (24) seem to underestimate permeability systematically for the low porosity Rhaetian sandstones from Allermoehe.

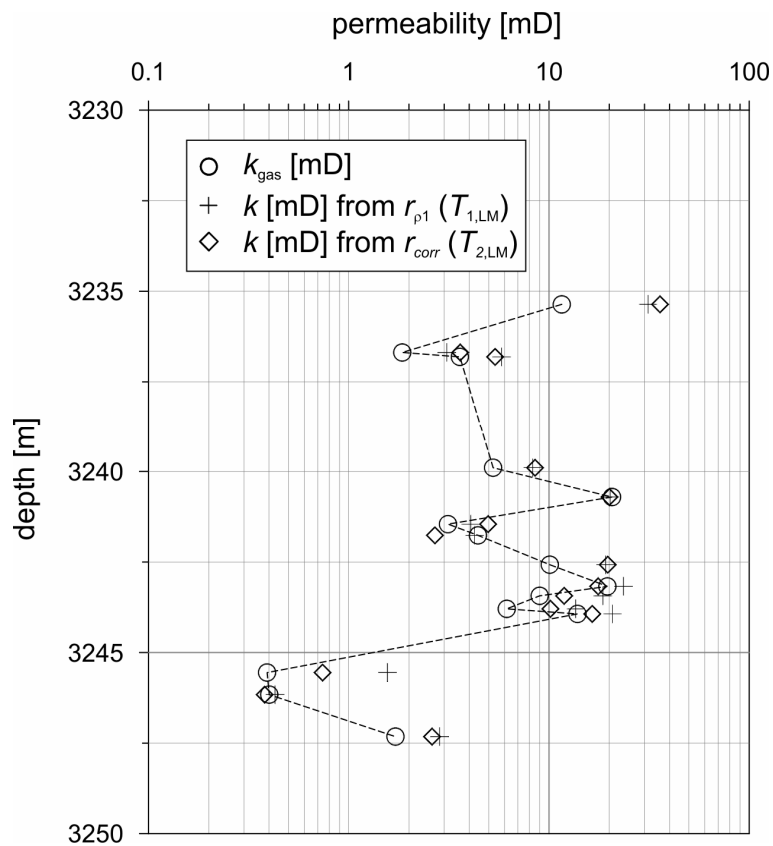


Figure 38: Permeabilities calculated from 2D T_1 and T_2 distributions according to equations (46) and (47) (Table 9) plotted versus depth and compared to gas permeabilities for Allermoehe samples.

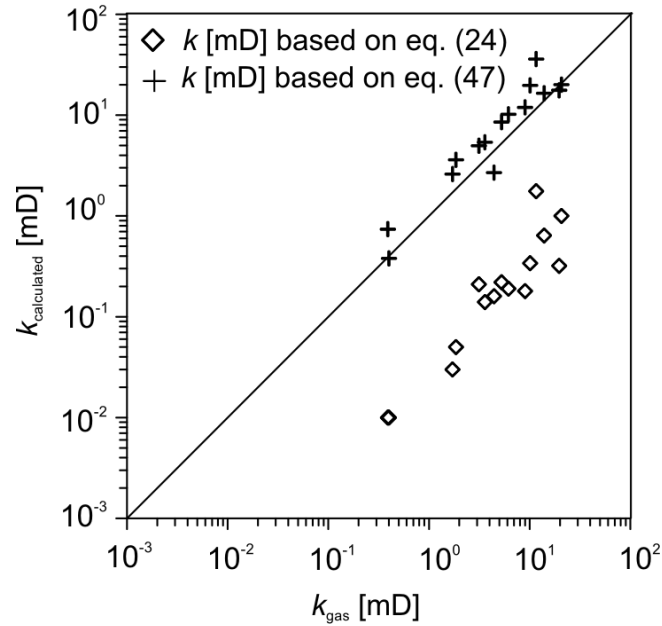


Figure 39: Correlations of Allermoehe core plug permeabilities: results from gas flow measurements are compared to (1) calculated permeabilities according to the standard method in oil industry ($T_{2,LM}$ equation (24) using a factor of $a = 4$) and (2) calculated permeabilities from r_{corr} ($T_{2,LM}$) according to equation (47); all calculated permeability values are based on 2D T_2 measurements.

6.8 Permeability from 1D T_2 relaxation

Permeabilities of the Allermoehe core plugs were also derived from 1D transverse relaxation measurements performed with the improved Halbach core-scanner.

For the samples with available pore size distribution, individual relaxivities $\rho_{2,eff}$ were determined by coinciding the maxima of both frequency distributions. A mean value of $\rho_{2,eff}$ was calculated and used for the other samples. As an example, Figure 40 shows the distribution curves of T_2 values and pore radii measured on Allermoehe sample AC9 and the resulting surface relaxivity $\rho_{2,eff}$.

Pore radii $r_{\rho_{2,eff}}(T_{2,LM})$ were calculated from logarithmic mean relaxation times $T_{2,LM}$ according to equation (35). In the case of samples AC1 and AC3 with very small pore radii, $T_{2,LM}$ values were calculated by using a lower T_2 cutoff of $T_2 = 0.9$ ms corresponding to the clay region. The pore radii were corrected according to equation (45) by multiplication with the term $(9.53/r_{\rho_{2,eff}})^{0.3}$ yielding $r_{corr}(T_{2,LM})$.

Permeability was calculated from equation (47) with $c = 0.7$ (cf. chapter 6.5) and tortuosity $T_{\text{hydr}} = 0.6 \Phi^{-1.2}$ for $\Phi \geq 0.05$ (David, 1993; cf. Table 6), and $T_{\text{hydr}} = 20$ for $\Phi < 0.05$ (Pape et al., 2005b).

Equation (47) is consistent with:

$$k = \left(\frac{1}{8}\right) \left(\frac{c \Phi}{T_{\text{hydr}}}\right) \underbrace{\left(3 \rho_{1,2,\text{eff}} T_{2,\text{LM,corr}}\right)}_{r_{\text{eff}}, \text{ cf. eqs. (28) and (29)}}^2$$

$$\left(k \text{ in } \mu\text{m}^2; \rho_{1,2,\text{eff}} \text{ in } \mu\text{m/s}\right), \quad (48)$$

where $T_{2,\text{LM,corr}}$ is the corrected logarithmic mean

$$T_{2,\text{LM,corr}} = T_{2,\text{LM}} \left(\frac{9.53 \mu\text{m}}{3 \rho_{2,\text{eff}} T_{2,\text{LM}}}\right)^{0.3}. \quad (49)$$

The effective surface relaxivity $\rho_{2,\text{eff}}$, corrected pore radii $r_{\text{corr}}(T_{2,\text{LM}})$, and permeability are presented in Table 10. To obtain permeability values according to equation (49) the mean value of $\rho_{2,\text{eff}}$ was used. In Figure 41, the permeabilities calculated from 1D T_2 distributions according to equation (47) are plotted versus depth and compared to gas permeabilities. Additionally, Figure 42 shows the comparison to permeability values calculated by the standard method in oil industry from 1D T_2 distributions according to the $T_{2,\text{LM}}$ equation (24) using a factor of $a = 4$ which is generally accepted for sandstones. Whereas permeabilities derived from equations (47) and (48) agree well with gas flow measurements, results from the standard method used in oil industry based on equation (24) underestimate permeability systematically. Particularly for the samples AC1 and AC3 which contain a considerable amount of clay, permeabilities are underestimated by four orders of magnitude.

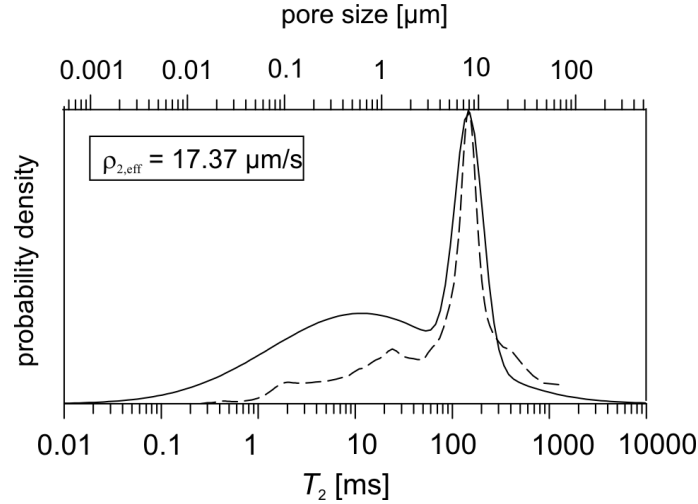


Figure 40: Distributions of pore radii (dashed line) and 1D NMR relaxation time T_2 (full line) measured with the improved Halbach core-scanner on Allermoehe sample AC9. For the given surface relaxivity $\rho_{2,\text{eff}}$, both distribution maxima coincide.

Table 10: Results based on 1D T_2 relaxation measurements with the improved Halbach core-scanner: $\rho_{2,\text{eff}}$ values follow from equation (37); $r_{\text{corr}}(T_{2,\text{LM}})$ values result from equation (45) and permeabilities k from $r_{\text{corr}}(T_{2,\text{LM}})$ according to equation (47) and from $T_{2,\text{LM,corr}}$ according to equations (48) and (49).

sample	$\rho_{2,\text{eff}} [\mu\text{m/s}]$	$r_{\text{corr}}(T_{2,\text{LM}})$	k [mD]	k [mD]	k_{gas}
	eq. (35)	[μm] eq. (45)	from $r_{\text{corr}}(T_{2,\text{LM}})$ eq. (47)	from $T_{2,\text{LM,corr}}$ eqs. (48) and (49)	[mD]
AC1	-	1.53	0.21	0.21	0.16
AC3	-	2.49	0.55	0.55	0.42
AC4	-	6.14	27.90	27.91	11.6
AC6	-	1.79	0.97	0.97	1.85
AC7	21.60	3.32	6.30	6.46	3.59
AC9	17.37	2.31	3.03	2.73	5.26
AC10	23.46	3.33	12.72	13.70	20.7
AC12	13.10	2.33	4.01	3.06	3.13
AC13	22.05	3.29	7.99	8.30	4.42
AC14	13.10	2.22	3.64	2.78	10.1
AC15	27.85	4.07	12.22	14.56	19.6
AC16	29.68	3.52	7.07	8.74	8.99
AC18	26.29	2.87	4.69	5.40	6.16
AC19	-	3.16	4.43	4.44	13.9
AC20	23.07	3.24	5.99	6.39	7.2
AC21	-	2.23	2.11	2.12	3.1
AC22	-	2.06	1.81	1.81	0.39
AC23	10.38	1.34	1.02	0.68	0.4
AC25	-	2.71	0.48	0.48	1.71
mean value	20.72				

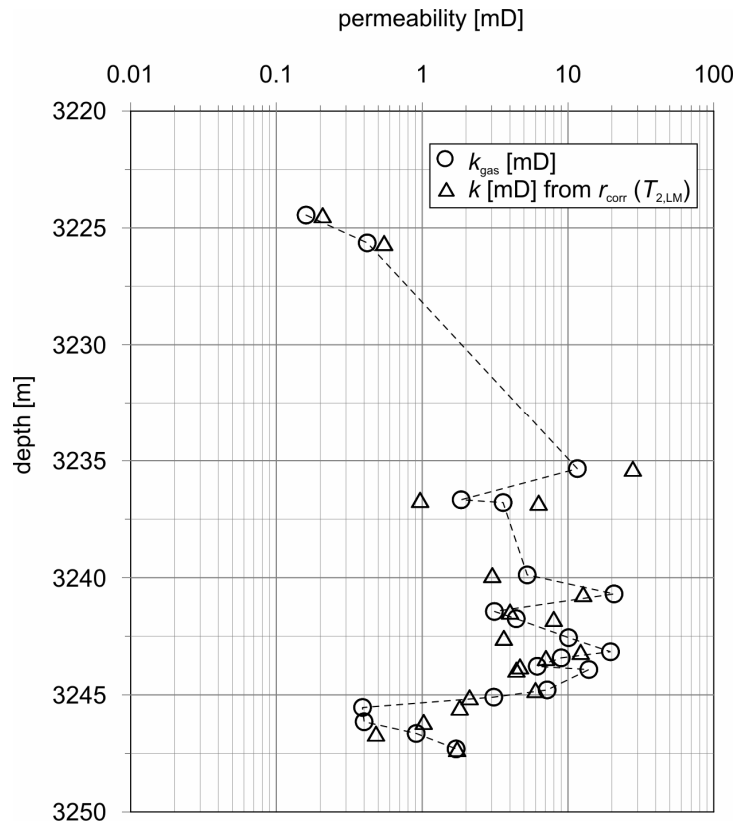


Figure 41: Permeabilities calculated from 1D T_2 distributions according to equation (47) plotted versus depth and compared to gas permeabilities.

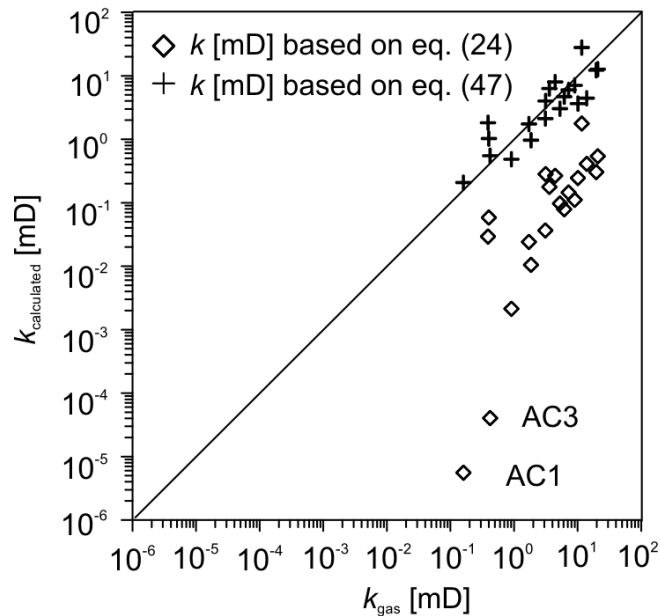


Figure 42: Correlations of Allermoehe core plug permeabilities: results from gas flow measurements are compared to (1) calculated permeabilities according to the standard method in oil industry ($T_{2,\text{LM}}$ equation (24) using a factor of $a = 4$) and (2) permeabilities according to equation (47). All calculated permeability values are based on 1D T_2 distributions measured with the improved Halbach core-scanner.

6.9 Appraisal of the results

T_1 and T_2 distribution measurements were performed with different mobile NMR core-scanners. According to the particular characteristics of each sensor, different petrophysical parameters could be determined from 1D T_2 - and 2D T_1 - T_2 correlation-measurements.

For the NMR-MOUSE[®] which has a magnetic field gradient of 12 T/m the influence of diffusion in the external gradient cannot be neglected, even if the relaxation measurements are performed on samples with low magnetic susceptibility values and with a short echo time. If the static magnetic field is inhomogeneous and varies with position in the same sample, different protons precess with different frequencies. Their precessions are quickly out of phase with each other, so that the transverse magnetization decays rapidly. Hence, distributions of $T_{2,\text{eff}}$ obtained with the NMR-MOUSE[®] cannot be related directly to pore size distribution.

Compared to studies with the NMR-MOUSE[®], measurements with both Halbach core-scanners are less influenced by diffusion and have better time resolution such that faster relaxation components can be recorded. For this reason, the Halbach core-scanners are better suited to study clay-rich samples. High magnetic susceptibility values of the cores, however, limit the straightforward determination of the pore size distribution from relaxation data. But the Halbach core-scanners can be used as a fast and non-destructive instrument to estimate the pore size distribution of drill cores with low magnetic susceptibility values.

The common empirical $T_{2,\text{LM}}$ equation used in the oil industry for estimating permeability from NMR logging data, is acceptable for typical reservoir rocks with high porosity and permeability. Here, the influence of diffusion due to internal magnetic field gradients caused by paramagnetic centers at the pore walls can be neglected in large-radius pores. In the case of the Rhaetian sandstone formation at Allermoehe with low porosity and permeability, this calculation scheme yields large errors. These are caused by diffusion in the internal magnetic field gradients which are associated with small pore radii of the rocks. However, accurate permeability prediction from transverse relaxation measurements is possible: From T_1 - T_2 correlation experiments, the relationship between the surface relaxivities ρ_1 and ρ_2 can be determined. Based on a model, where a field gradient interlayer envelopes the inner side of the pore walls, the thickness of this interlayer and the corresponding field gradient interlayer relaxation $\rho_{2,\text{ifg}}$ can be calculated. Therefore, a constant value for ρ_1 can be obtained from the comparison of T_1 distributions with mercury injection curves. Based on this analysis, it is possible to calculate an individual surface relaxivity ρ_2 for each T_2 value.

Finally, a hydraulic effective pore radius can be calculated for each sample from the logarithmic mean value of the T_2 distribution curves. Moreover, an empirical equation which is calibrated for T_2 distributions measured on the Allermoehe samples can be used to calculate effective pore radii. Consequently, permeability can be predicted accurately from the effective pore radii with the physically based Kozeny-Carman equation (Kozeny, 1927; Carman, 1937).

7 Conclusion & Outlook

Newly developed mobile NMR core-scanning devices using weak magnetic fields can be applied to measure NMR decay curves on drill cores in order to determine porosity and estimate pore-size distributions and permeability on drill cores. The unilateral NMR-MOUSE[®] and both Halbach core-scanners differ in magnetic field strength, operating frequencies, field homogeneity and sensitive volume. The main advantages of the NMR instruments discussed in this study are their small size, low weight, and mobility. This permits analysis on water-saturated full cores either in the laboratory or at the drilling-platform. Cores can be measured in their original water-saturated state directly after recovery without prior preparation. This allows a more accurate porosity determination compared to measurements on drill cores which are resaturated in the laboratory after drying during storage.

The unilateral NMR-MOUSE[®] is the smallest and handiest device. Measurements require no particular sample geometry, except for a flat surface. Thus, the device is suitable for measuring semi-cylindrical cores (ODP/IODP standard). NMR experiments with the NMR-MOUSE[®] yield accurate porosity values on water-saturated drill cores. A volume calibration of the samples is not required as the sensitive volume of the NMR-MOUSE[®] is well defined at a fixed frequency. Because of its small sensitive region, the NMR-MOUSE[®] is used to determine local heterogeneities in the samples. Due to the highly inhomogeneous magnetic field of the NMR-MOUSE[®], the decay of the echo envelope is strongly affected by diffusion. Hence, distributions of transverse relaxation obtained with the NMR-MOUSE[®] cannot be related to pore-size distributions.

Both Halbach core-scanners are slightly bigger and heavier than the NMR-MOUSE[®]. However, they are still versatile and mobile. With the Halbach core-scanners, the transverse relaxation measurement times are reduced from one half hour to a few seconds. Measurements on full cores with both Halbach core-scanners have the advantage of integrating a considerably larger volume compared to the NMR-MOUSE[®] and to commercial devices which are convenient only for drill cuttings and core plugs. Because of the lower field gradient and the larger sensitive volume, both Halbach core-scanners record a stronger signal with a correspondingly better signal-to-noise ratio than that of the NMR-MOUSE[®]. Hence, porosity measurements with the Halbach core-scanners are more accurate: Even low porosities in the range of 2 % - 5 % can be detected which cannot be measured by the NMR-MOUSE[®]. The low and homogeneous measuring fields of the Halbach core-scanners provide

an additional advantage because measurements are less influenced by diffusion and for this reason, faster relaxation components can be recorded and even clay-rich samples can be studied.

If the studied samples have high magnetic susceptibilities this results in a low signal-to-noise ratio. For drill cores with magnetic susceptibility values larger than 30×10^{-3} SI, no signals can be detected. T_2 distributions recorded on mafic rocks, such as basalt, gabbro and peridotite recovered within ODP/IODP, are strongly distorted due to local internal field gradients, even when measured in a homogeneous static magnetic field. Hence, they cannot be related to pore size distributions and permeability cannot be predicted.

In contrast, NMR results obtained within the homogeneous static magnetic field of the Halbach core-scanners on samples with low magnetic susceptibility values have sufficiently high quality to estimate permeability. The commonly used oil-field standard equation to estimate permeability from NMR results is useful in case of formations with high porosity and permeability. For rocks with low porosity and small pore radii, this calculation scheme contains large errors due to the strong influence of internal magnetic field gradients. Hence, in the latter case T_1 measurements which are not affected by any diffusion should be preferably used to predict permeability from NMR logging data. However, if T_2 was measured in the laboratory within a homogeneous external magnet field these values are as useful for permeability prediction as T_1 measurements. To calculate permeability from T_2 distributions, the increasing influence of the surface relaxivity ρ_2 with decreasing pore radius has to be accounted for. For this reason the logarithmic mean value $T_{2,LM}$ has to be multiplied with the term $(3.18 / (\rho_{2,eff} T_{2,LM}))^{0.3}$ which was calibrated for Allermoehe sandstones. However, for each formation T_2 measurements have to be calibrated by independent permeability measurements on core plugs. However, permeability is not only a function of the pore radius, which is proportional to T_1 or T_2 , but depends also on several structural parameters. To extend the interpretation with respect to permeability, additional studies of transport properties besides independent pore-size measurements are helpful including the formation factor and the specific inner surface area. In the future, it could be studied if the calibration term for $T_{2,LM}$ values which was developed for the Rhaetian sandstones at Allermoehe can be applied also to other sandstone or even limestone formations.

Recent efforts aim for adapting NMR methods also to ODP and the upcoming IODP program. Mobile NMR instruments tested and calibrated in the present study show a great potential for the application on board of research vessels. The possibility to measure fresh cores right after drilling in their original wet state provides excellent conditions for accurate

porosity determination. This could be done, for example, with the NMR-MOUSE[®]. The use of Halbach core-scanners with a homogeneous static magnetic field is of particular interest as they permit to estimate permeability. As yet, this property is not measured on board of the drill ship. For the measurements, limestones commonly recovered within ODP/IODP are mainly suitable as they are low in magnetic susceptibility. If the cores are fresh so that no additional saturation is necessary, even less consolidated sediments as sand, silt, and mud could be studied. Hence, the application of mobile NMR instruments on board of the drill ship could provide a significant contribution to the scientific topics and operational conditions of the ODP/IODP.

References

Abragam, A., 1961. The Principles of Nuclear Magnetism, pp. 82-83, Clarendon Press, Oxford.

Allen, D.F., Flaum, C., Ramakrishnan, T.S., Bedford, J., Castelijns, K., Fairhurst, D., Gubelin, G., Heaton, N., Minh, C.C., Norville, M.A., Seim, M.R., Pritchard, T. and Ramamoorthy, R., 2000. Trends in NMR Logging, *Oilfield Review*, 12 (3): 2-19.

Anferova, S., Anferov, V., Arnold, J., Talnishnikh, E., Voda, M., Kupferschläger, K., Blümmler, P., Clauser, C. and Blümich, B., 2007. Improved Halbach Sensor for NMR Scanning of Drill Cores, *Magnetic Resonance Imaging*, 25 (4): 474-480.

Anferova, S., Anferov, V., Rata, D.G., Blümich, B., Arnold, J., Clauser, C., Blümmler, P. and Raich H., 2004. A Mobile NMR Device for Measurements of Porosity and Pore Size Distributions of Drilled Core Samples, *Concepts in Magnetic Resonance Part B (Magnetic Resonance Engineering)*, 23B (1): 26-32.

Anferova, S., Anferov, V., Adams, M., Blümmler, P., Routley, N., Hailu, K., Kupferschläger, K., Mallet, M., Schroeder, G., Sharma, S. and Blümich, B., 2002. Construction of the NMR-MOUSE[®] with short dead time, *Concepts in Magnetic Resonance Part B (Magnetic Resonance Engineering)*, 15B (1): 15-25.

Archie, G.E., 1942. The electrical resistivity logs as an aid in determining some reservoir characteristics, *Transactions of the American Institute of Mining and Engineering*, 146: 54-62.

Arnold, J., Bartetzko, A., Iturrino, G. and Paulick, H., submitted. Facies reconstruction from Resistivity-at-the-Bit images recorded in a submarine felsic volcanic succession, submitted to *Marine Geophysical Researches*.

Arnold, J., Clauser, C., Pechinig, R., Anferova, S., Anferov, V. and Blümich, B., 2006. Porosity and Permeability from Mobile NMR Core-Scanning, *Petrophysics*, 47 (4): 306-314.

Bartetzko, A., Klitzsch, N., Iturrino, G., Kaufhold, S. and Arnold, J., 2005. Electrical properties of hydrothermally altered dacite from the PACMANUS hydrothermal field (ODP Leg 193), *Journal of Volcanology and Geothermal Research*, 152: 109-120.

Bartetzko, A., Paulick, H., Iturrino, G. and Arnold, J., 2003. Facies reconstruction of a hydrothermally altered dacite extrusive sequence: Evidence from geophysical downhole logging data (ODP Leg 193), *Geochemistry Geophysics Geosystems* G³, 4 (10): 24p.

Blümich, B., Casanova, F., Buda, A., Kremer, K. and Wegener, T., 2005. Mobile NMR for analysis of polyethylene pipes, *Acta Physica Polonica A*, 108: 13-23.

- Blümich, B., Anferova, S., Casanova, F., Kremer, K., Perlo, J. and Sharma, S., 2004a. Unilateral NMR: Principles and Applications to Quality Control of Elastomer Products, *KGK Kautschuk, Gummi, Kunststoffe*, 57: 346-349.
- Blümich, B., Anferova, S., Pechinig, R., Pape, H., Arnold, J. and Clauser, C., 2004b. Mobile NMR for porosity analysis of drill core sections, *Journal of Geophysics and Engineering*, 1: 177-180.
- Blümich, B., 2000. *NMR Imaging of Materials*, Clarendon Press, Oxford.
- Blümich, B., Blümli, P., Eidmann, G., Gutshausen, A., Haken, R., Schmitz, U., Saito, K. and Zimmer, G., 1998. The NMR-MOUSE[®]: construction, excitation, and applications, *Magnetic Resonance Imaging*, 16: 479-484.
- Borgia, G.C.; Brown, R.J.S. and Fantazzini, P., 1998. Uniform-penalty inversion of multiexponential decay data, *Journal of Magnetic Resonance*, 132: 65-77.
- Brownstein, K.R. and Tarr, C.E., 1977. Importance of classical diffusion in NMR studies of water in biological cells, *Physical Review A*, 19: 2446-2453.
- Brunauer, S., Emmet, H. and Teller, E., 1938. Adsorption of Gases in Multimolecular Layers, *Journal of the American Chemistry Society*, 60 (2): 309–319.
- Carman, P.C., 1956. *Flow of gases through porous media*, Butterworth Scientific Publications, London.
- Carr, H.Y. and Purcell, E.M., 1954. Effects of Diffusion on Free Precession in Nuclear Magnetic Resonance Experiments, *Physical Review*, 94 (3): 630–638.
- Changh, D., Vinegar, H.J., Morris, C.E. and Straley, C., 1994. Effective porosity, producible fluid and permeability in carbonates from NMR logging, paper A, in 35th annual logging symposium transactions: Society of Professional Well Log Analysts SPWLA, 21 p.
- Chen, Q., Kinzelbach, W., Ye, C. and Yue, Y., 2002. Variations of Permeability and Pore Size Distribution of Porous Media with Pressure, *Journal of Environmental Quality*, 31: 500-505.
- Coates, G.R., Xiao, L. and Prammer, M.G., 1999. *NMR Logging – Principles and Applications*, Halliburton Energy Services, Houston.
- Cohen, M.H. and Mendelson, K.S., 1982. Nuclear magnetic relaxation and the internal geometry of sedimentary rocks, *Journal of Applied Physics*, 53 (2): 1127-1135.
- Darling, R., 2005. *Well Logging and Formation Evaluation*, Elsevier, Amsterdam.
- David, C., 1993. Geometry of Flow Path for Fluid Transport in Rocks, *Journal of Geophysical Research*, 98 (B7), 12: 267-278.
- Dullien, F.A.L., 1979. *Porous media: fluid transport and pore structure*, Academic Press, New York.

References

- Dunn, K.J., Bergman, D.J. and Latorraca, G.A., 2002. Handbook of geophysical exploration. Seismic exploration, Elsevier Pergamon, Oxford.
- Eidmann, G., Savelberg, R., Blümler, P. and Blümich, B., 1996. The NMR-MOUSE[®], a mobile universal surface explorer, *Journal of Magnetic Resonance A*, 122: 104-109.
- Flikweert, A.J., 2003. Investigating Rubber Samples with the NMR-MOUSE[®] and Bruker Spectrometers, Doctoral Dissertation, TU Eindhoven, Eindhoven.
- Geotek, 2000. Multi-Sensor Core Logger Manual: Geotek, Nene House Drayton Fields, Daventry Northants NN11 5EA, United Kingdom.
- Godefroy, S. and Callaghan, P.T., 2003. Two dimensional relaxation/diffusion correlation in porous media, *Magnetic Resonance Imaging*, 21: 381-383.
- Hahn, E.L., 1950. Spin echoes, *Physical Review*, 80 (4): 580-594.
- Halbach, K., 1980. Design of permanent multipole magnets with oriented rare earth cobalt material, *Nuclear Instruments & Methods in Physics Research*, 169: 1-10.
- Hook, J.R., 2003. An Introduction to Porosity, *Petrophysics*, 44 (3): 205-212.
- Hoult, D.I. and Richards, R.E., 1976. The Signal-to-Noise Ratio of the Nuclear Magnetic Resonance Experiment, *Journal of Magnetic Resonance*, 24: 71-85.
- Hürlimann, M.D. and Venkataramanan, L., 2002. Quantitative Measurement of Two-Dimensional Distribution Functions of Diffusion and Relaxation in Grossly Inhomogeneous Fields, *Journal of Magnetic Resonance*, 157: 31-42.
- Hürlimann, M.D. and Griffin, D.D., 2000. Spin Dynamics of Carr-Purcell-Meiboom-Gill like Sequences in Grossly Inhomogeneous B_0 and B_1 Fields and Application to NMR Well Logging, *Journal of Magnetic Resonance*, 143 (1): 120-135.
- Hürlimann, M.D., Helmer, K.G., LaTour, L.L. and Sotak, C.H., 1994. Restricted Diffusion in Sedimentary Rocks. Determination of Surface-Area-to-Volume Ratio and Surface Relaxivity, *Journal of Magnetic Resonance, Series A*, 111: 169-178.
- Kenyon, W.E., Allen, D.F.; Lisitza, N.V. and Song, Y.Q., 2002. Better pore-size distributions from stimulated-echo NMR lab measurements using magnetic susceptibility contrast and small encoding angles, paper III, in 43th annual logging symposium transactions: Society of Professional Well Log Analysts, 14 p.
- Kenyon, W.E., 1997. Petrophysical Principles of Applications of NMR Logging, *The Log Analyst*, 38 (2): 21-43.
- Kenyon, W.E. and Kolleeny, J.A., 1995. NMR surface relaxivity of calcite with adsorped Mn^{2+} , *Journal of Colloid and Interface Science*, 170: 502-514.
- Kenyon, W.E., 1992. Nuclear magnetic resonance as a petrophysical measurement, *Nuclear Geophysics*, 6 (2): 153-171.

- Kenyon, W.E., Day, P.I., Straley, C. and Willemsen, J.F., 1988. A three-part study of NMR longitudinal relaxation properties of water-saturated sandstones. Society of Petroleum Engineers SPE Formation Evaluation, 3: 622-636.
- Kleinberg, R.L., Kenyon, W.E. and Mitra, P.P., 1994. Mechanism of NMR relaxation of fluids in rocks, Journal of Magnetic Resonance, Series A, 108: 206-214.
- Kleinberg, R.L. and Horsfield, M.A., 1990. Transverse Relaxation Process in Porous Sedimentary Rock, Journal of Magnetic Resonance, 88: 9-19.
- Kozeny, J., 1927. Über die kapillare Leitung des Wassers im Boden (Aufstieg, Versickerung und Anwendung auf die Bewässerung): Sitzungsberichte der Akademie der Wissenschaften in Wien, Mathematisch Naturwissenschaftliche Klasse (Abt. IIa), 136a: 271-306.
- Kukla, P. and Trautwein-Bruns, U., 2006. Ein tiefer Blick in die Aachener Unterwelt, Forschung – Das Magazin der Deutschen Forschungsgemeinschaft, 4: 22-25 (www.rwth-aachen.de/geow/Ww/rwth1geo/index.html).
- Lonnes, S., Guzman-Garcia, A. and Holland, R., 2003. NMR Petrophysical Predictions On Cores, paper DDD, in 44th annual logging symposium transactions: Society of Professional Well Log Analysts SPWLA, 13 p.
- Luthi, S.M., 2001. Geological Well Logs: Use in Reservoir Modeling, Springer, Berlin, Heidelberg.
- Matzkanin, G.A., 1989. A review of nondestructive characterization of composites using NMR, Springer, Berlin.
- Meiboom, S. and Gill, D., 1958. Modified spin-echo method for measuring nuclear relaxation times, Review of Scientific Instruments, 29: 668-691.
- Mirotchnik, K., Kryuchkov, S. and Strack, K., 2004. A Novel Method To Determine NMR Petrophysical Parameters From Drill Cuttings, paper MM, in 45th annual logging symposium transactions: Society of Professional Well Log Analysts SPWLA, 15 p.
- Morris, C.E., Freedman, R., Straley, C., Johnston, M., Vinegar, H.J. and Tutunjian, P.N., 1994. Hydrocarbon saturation and viscosity estimation from NMR logging in the Belridge diatomite, paper C, in 35th annual logging symposium transactions: Society of Professional Well Log Analysts, 24 p.
- Müller, M. and Yaramanci, U., 2005. Surface Nuclear Magnetic Resonance – Applications in hydrogeophysics and future developments, Magnetic Resonance Imaging, 23 (2), 417.
- N.N, 2005. Catalogue of Reference Procedures, Testing and Chemical Analysis, Bundesanstalt für Materialforschung und Prüfung, Berlin. (www.bam.de/en/kompetenzen/fachabteilungen/abteilung_1/fg13/index).
- N.N, 2003. Meteor Cruise No. 58, Leg 2, NW Africa, Research Centre of Ocean Margins, University of Bremen.

References

- Pape, H., Arnold, J., Pechnig, R., Clauser C., Talnishnikh, E., Anferova, S. and Blümich, B., manuscript in preparation. Permeability prediction for low porosity rocks by mobile NMR.
- Pape, H., Tillich, J.E. and Holz, M., 2005a. Pore geometry of sandstone derived from pulsed field gradient NMR, *Journal of Applied Geophysics*, 58 (3): 232-252.
- Pape, H., Clauser, C., Iffland, J., Krug, R. and Wagner, R., 2005b. Anhydrite cementation and compaction in geothermal reservoirs: Interactions of pore-space structure with flow, transport, P-T conditions, and chemical reactions, *International Journal of Rock Mechanics & Mining Sciences*, 42: 1056-1069.
- Pape, H., Clauser, C. and Iffland, J., 2000. Variation of permeability with porosity in sandstone diagenesis interpreted with a fractal pore space model. *Pure applied Geophysics*, 157: 603-619.
- Pape, H., Clauser, C. and Iffland, J., 1999. Permeability prediction based on fractal pore-space geometry, *Geophysics*, 64 (5): 1447-1460.
- Pape, H., Riepe, L. and Schopper, J.R., 1987. Theory of self-similar network structures in sedimentary and igneous rocks and their investigation with microscopical methods, *Journal of Microscopy*, 148: 121-147.
- Perlo, J., 2006. Single-Sided NMR Tomography, Doctoral Dissertation, Aachen University, Aachen.
- Raich, H. and Blümmler, P., 2004. Design and construction of a dipolar Halbach array with a homogeneous field from identical bar-magnets: NMR mandhalas. *Concepts in Magnetic Resonance Part B (Magnetic Resonance Engineering)*, 23B:16-25.
- Rieckmann, M., 1970. Untersuchung von Turbulenzerscheinungen beim Fließen von Gasen durch Speichergesteine unter Berücksichtigung der Gleitströme, *Erdöl-Erdgas-Zeitschrift*, 86: 36-51.
- Schön, J.H., 1996. Physical properties of rocks: Fundamentals and principles of petrophysics. *Handbook of Geophysical Exploration*, vol. 18, Pergamon Press, Oxford.
- Serra, O. and Serra, L., 2004. Well Logging – Data Acquisition and Applications, Serralog, Méry Corbon – France.
- Shipboard Scientific Party, 2004a. Proceedings of the Ocean Drilling Program, Initial Reports, 209, College Station, USA.
- Shipboard Scientific Party, 2004b. Proceedings of the Ocean Drilling Program, Initial Reports, 210, College Station, USA.
- Shipboard Scientific Party, 2003. Proceedings of the Ocean Drilling Program, Initial Reports, 204, College Station, USA.

- Shipboard Scientific Party, 1997a. Proceedings of the Ocean Drilling Program, Initial Reports, 165, College Station, USA.
- Shipboard Scientific Party, 1997b. Proceedings of the Ocean Drilling Program, Initial Reports, 166, College Station, USA.
- Shipboard Scientific Party, 1996. Proceedings of the Ocean Drilling Program, Initial Reports, 163, College Station, USA.
- Shipboard Scientific Party, 1994. Proceedings of the Ocean Drilling Program, Initial Reports, 152, College Station, USA.
- Song, Y.Q., 2003. Using Internal Magnetic Fields to Obtain Pore Size Distributions of Porous Media, Concepts in Magnetic Resonance Part A, 18A: 97-110.
- Song, Y.Q., Venkataramanan, L., Hürlimann, M.D., Flaum, M., Frulla, P. and Straley, C., 2002. T_1 - T_2 correlation spectra obtained using a fast two-dimensional Laplace inversion, Journal of Magnetic Resonance, 154: 261-268.
- Song, Y.Q., 2000. Determining Pore Sizes Using an Internal Magnetic Field, Journal of Magnetic Resonance, 143: 397-401.
- Straley, C., Rossini, D., Vinegar, H., Tutunjian, P. and Morriss C., 1997. Core analysis by low-field NMR, The Log Analyst, 38 (2): 84-93.
- Timur, A., 1969. Pulsed nuclear magnetic resonance studies of porosity, movable fluid permeability of sandstones, Journal of Petroleum Technology, 21: 775-786.
- Toumelin, E., Torres-Verdín, C., Chen, S. and Fischer, D.M., 2003. Reconciling NMR measurements and numerical simulations: assessment of temperature and diffusive coupling effects on two-phase carbonate samples, Petrophysics, 44 (2): 91-107.
- Webb, P.A., 2001. An introduction to the physical characterization of materials by mercury intrusion porosimetry with emphasis on reduction and presentation of experimental data, Micromeritics Instrument Corporation, Norcross, Georgia.
- Yaramanci, U., 2000. Surface Nuclear Magnetic Resonance (SNMR) – A new method for exploration of ground water and aquifer properties, Annals Of Geophysics, 43 (6): 1159-1175.

Appendix

Table A: Porosity data obtained by the NMR-MOUSE®.

Laboratory label	Borehole	NMR porosity [%]	Pycnometer porosity [%]
152,917A,63R,2W,1B	ODP Hole 917A	26	20
152,917A,80R,2W,2D	ODP Hole 917A	6	11
163,989B,6R,8W,64 cm	ODP Hole 989B	9	6
163,989B,6R,8W,60 cm	ODP Hole 989B	5	8
163,989B,1R,4.1	ODP Hole 989B	18	14
163,989B,3R,1.4C	ODP Hole 989B	14	13
163,989b,4R,1.3C	ODP Hole 989B	14	16
165,999B,40R,3W,30 cm	ODP Hole 999B	11	10
165,999B,41R,2W,40 cm	ODP Hole 999B	22	22
165,999B,41R,2W,129 cm	ODP Hole 999B	14	16
165,999B,41R,2W,121 cm	ODP Hole 999B	16	18
165,999B,41R,2W,137 cm	ODP Hole 999B	16	19
165,999B,46R,3W,135 cm	ODP Hole 999B	25	19
166,1005C,21R,2W,141 cm	ODP Hole 1005C	23	15
166,1005C,21R,2W,137 cm	ODP Hole 1005C	25	18
166,1005C,34R,2W,134 cm	ODP Hole 1005C	22	17
166,1005C,34R,2W,132 cm	ODP Hole 1005C	20	18
Allermöhe3	Borehole Allermöhe	8	10
Allermöhe4	Borehole Allermöhe	11	12
Allermöhe6	Borehole Allermöhe	9	12
Allermöhe12	Borehole Allermöhe	14	15
Allermöhe13	Borehole Allermöhe	17	16

Table B: Porosity data obtained by the first version of the Halbach core-scanner.

Laboratory label	Borehole	NMR porosity [%]	Pycnometer porosity [%]
152,917A,63R,2W,WB	ODP Hole 917A	19	19
152,917A,101R,4W,20 cm	ODP Hole 917A	9	9
152,917A,101R,4W,32 cm	ODP Hole 917A	9	11
163,989B,6R,8W,64 cm	ODP Hole 989B	9	9
163,989B,6R,8W,60 cm	ODP Hole 989B	5	9
166,1005C,19R,1W,55 cm	ODP Hole 1005C	23	21
166,1005C,21R,1W,141 cm	ODP Hole 1005C	23	22
166,1005C,21R,1W,137 cm	ODP Hole 1005C	25	22
166,1005C,21R,1W,144 cm	ODP Hole 1005C	23	22
166,1005C,34R,1W,72 cm	ODP Hole 1005C	28	33
166,1005C,34R,1W,68 cm	ODP Hole 1005C	28	32
166,1005C,34R,1W,76 cm	ODP Hole 1005C	28	29
166,1005C,34R,2W,134 cm	ODP Hole 1005C	22	21
166,1005C,34R,2W,132 cm	ODP Hole 1005C	20	21
166,1005C,34R,1W,55 cm	ODP Hole 1005C	26	25
166,1005C,34R,1W,61 cm	ODP Hole 1005C	30	26
166,1005C,34R,1W,51 cm	ODP Hole 1005C	32	31
166,1005C,34R,1W,129 cm	ODP Hole 1005C	23	22
166,1005C,82R,2W,25 cm	ODP Hole 1005C	22	20
Allermöhe14	Borehole Allermöhe	16	17
Allermöhe15	Borehole Allermöhe	15	14
Allermöhe16	Borehole Allermöhe	10	10
Allermöhe17	Borehole Allermöhe	10	14
Allermöhe18	Borehole Allermöhe	9	13
Allermöhe19	Borehole Allermöhe	8	12
Allermöhe20	Borehole Allermöhe	16	17
SuperC,27-2	Borehole RWTH-1	2	2
SuperC,28-3	Borehole RWTH-1	3	4
SuperC,26-1	Borehole RWTH-1	2	2

Table C: Porosity data obtained by the modified version of the Halbach core-scanner.

Laboratory label	Borehole/outcrop	NMR porosity [%]	Pycnometer porosity [%]
AC1	Borehole Allermöhe	3	2
AC3	Borehole Allermöhe	2	2
AC4	Borehole Allermöhe	6	9
AC6	Borehole Allermöhe	6	6
AC7	Borehole Allermöhe	8	8
AC9	Borehole Allermöhe	9	8
AC10	Borehole Allermöhe	11	11
AC12	Borehole Allermöhe	10	9
AC13	Borehole Allermöhe	9	9
AC14	Borehole Allermöhe	9	9
AC15	Borehole Allermöhe	9	9
AC16	Borehole Allermöhe	8	8
AC18	Borehole Allermöhe	8	8
AC19	Borehole Allermöhe	7	10
AC20	Borehole Allermöhe	9	8
AC21	Borehole Allermöhe	7	7
AC22	Borehole Allermöhe	7	7
AC23	Borehole Allermöhe	7	8
AC24	Borehole Allermöhe	3	3
AC25	Borehole Allermöhe	5	6
BBSF	Bad Bentheim, Germany 52°18'37 N, 7°15'02 E	22	24
BASF	Barkhausen, Germany 52°17'03 N, 8°24'36 E	26	21
COF	Cotta, Germany 50°56'55 N, 14°0'39 E	26	21
IBSF	Ibbenbüren, Germany 52°16'50 N, 7°43'59 E	13	13
ROWE	Obernkirchen, Germany 52°15'47 N, 9°12'31 E	6	6
OBKI	Bad Karshafen, Germany 51°39'06 N, 9°26'30 E	20	17
SASF	Sand, Germany 49°58'39 N, 10°35'25 E	22	21
SRSF	Schleerieth, Germany 50°01'12 N, 10°05'26 E	17	14
VESF	Velpe, Germany 52°25'10 N, 10°56'30 E	25	24
ZÜSF	Züschchen, Germany 51°10'47 N, 9°14'01 E	21	19

Acknowledgements

First of all, I want to thank Prof. Dr. C. Clauser for giving me the opportunity to perform this thesis in his group. He stayed interested in its progress all the time. I am very grateful for his helpful advice and valuable discussions. Besides to that he helped me a great deal to improve my scientific writing.

I also want to thank Prof. Dr. B. Blümich to be the second supervisor of my doctoral studies and for encouraging my experimental and theoretical studies.

I am very grateful to Dr. R. Pechnig who motivated me during the whole time of my dissertation. I always profited very much from her comprehensive knowledge and advice.

I thank Dr. H. Pape and Dr. N. Klitzsch for generously supporting the dissertation with their scientific expertise.

I am also grateful to the scientists of the mobile NMR group of the Institute of Macromolecular and Technical Chemistry at Aachen University for interdisciplinary cooperation, in particular to Dr. S. Anferova and Prof. Dr. V. Anferov who contributed to the success of the NMR experiments. Elena Talnishnikh supported the study with 2D relaxation time data. It was really enjoyable to work with all of you and to share our experiences on research and life.

I am also grateful to my colleagues for the pleasant atmosphere at work.

Finally, I would like to thank my friends and family and my boyfriend Gero for all support and constant encouragement during the time that I was engaged in this study. Special thanks go to Sven who provided me feedback particularly in the endphase of my dissertation.

The German Science Foundation kindly supported this study under grant number CL 121/16-1/2 to C. Clauser, B. Blümich and R. Pechnig.

Curriculum Vitae

	Persönliche Angaben
Name	Juliane Arnold
Geburtsdatum	02.06.1977
Geburtsort	Düsseldorf
	Studium und wissenschaftlicher Werdegang
seit 12/2002	Wissenschaftliche Angestellte am Lehr-und Forschungsgebiet für Angewandte Geophysik der RWTH Aachen
28.11.2002	Geologie-Diplom
04/2002 - 10/2002	Diplomarbeit am Lehr-und Forschungsgebiet für Angewandte Geophysik der RWTH Aachen Titel der Arbeit: Interpretation der Lithologie eines aktiven Hydrothermalsystems durch Auswertung geophysikalischer Bohrlochlogs sowie von RAB- und FMS-Bildern aus der ODP-Bohrung 1189
01/2000 - 11/2002	Studentische Hilfskraft am Lehr-und Forschungsgebiet für Angewandte Geophysik der RWTH Aachen
10/1996 - 11/2002	Geologie-Studium, RWTH Aachen
	Wesentliche Veröffentlichungen
1	Bartzko, A., Paulick, H., Iturrino, G. and Arnold, J., 2003. Facies reconstruction of a hydrothermally altered dacite extrusive sequence: Evidence from geophysical downhole logging data (ODP Leg 193), <i>Geochemistry Geophysics Geosystems</i> G ³ , 4 (10): 24p.
2	Anferova, S., Anferov, V., Rata, D.G., Blümich, B., Arnold, J., Clauser, C., Blümmler, P. and Raich H., 2004. A Mobile NMR Device for Measurements of Porosity and Pore Size Distributions of Drilled Core Samples, <i>Concepts in Magnetic Resonance Part B (Magnetic Resonance Engineering)</i> , 23B (1): 26-32.
3	Blümich, B., Anferova, S., Pechinig, R., Pape, H., Arnold, J. and Clauser, C., 2004. Mobile NMR for porosity analysis of drill core sections, <i>Journal of Geophysics and Engineering</i> , 1: 177-180.
4	Bartzko, A., Klitzsch, N., Iturrino, G., Kaufhold, S. and Arnold, J., 2005. Electrical properties of hydrothermally altered dacite from the PACMANUS hydrothermal field (ODP Leg 193), <i>Journal of Volcanology and Geothermal Research</i> , 152: 109-120.

- 5 Arnold, J., Clauser, C., Pechinig, R., Anferova, S., Anferov, V. and Blümich, B., 2006. Porosity and Permeability from Mobile NMR Core-Scanning, *Petrophysics*, 47 (4): 306-314.
- 6 Anferova, S., Anferov, V., Arnold, J., Talnishnikh, E., Voda, M., Kupferschläger, K., Blümmler, P., Clauser, C. and Blümich, B., 2007. Improved Halbach Sensor for NMR Scanning of Drill Cores, *Magnetic Resonance Imaging*, 25 (4): 474-480.
- 7 Arnold, J., Bartetzko, A., Paulick, H. and Iturrino, G., accepted. Facies reconstruction from resistivity-at-the-bit images recorded in a submarine volcanic succession, *Marine Geophysical Researches*.

Dezember 2008